MEDICAL IMAGE SEGMENTATION SYSTEM

FOR CEREBRAL ANEURYSMS

by

Yuka Sen

Dissertation submitted in fulfilment of the requirements

for the degree of

DOCTOR OF PHILOSOPHY

Department of The Australian School of Advanced Medicine
Faculty of Medicine and Health Sciences
Macquarie University
Sydney, Australia

February 2015

ABSTRACT

Background: Ruptured intracranial aneurysms is a much studied topic, with reports indicating the presence of unruptured intracranial aneurysms in approximately 5% of the adult population. Although the rupture rate of intracranial aneurysms is not high, it may lead to serious consequences including disability and mortality. Current treatments for intracranial aneurysms, however, also carry significant risks. To counter this, accurate assessment of the potential for intracranial aneurysm rupture is thereby essential in order for clinicians to balance the risk of surgery against the risk of the natural history.

In current medical practice, greater emphasis is placed upon medical imaging technologies, including CTA, MRA and DSA scan for diagnostic purposes. These are widely applied in neurovascular imaging as a non-invasive diagnostic tool for the detection and evaluation of intracranial aneurysms. This makes it possible to visualize three dimensional (3D) cerebral aneurysms, the results allowing us to be able to reconstruct patient-specific vessels and aneurysms. Currently, the 3D geometry blood vessel has been applied in the performance of haemodynamic simulations, with the results obtained subsequently applied as a tool for the diagnosis of aneurysm risk and in support of neurosurgeons for the treatment of aneurysms. Visualization and haemodynamic simulations are all based upon the results of medical image reconstruction - aimed at the extraction geometries of targeted intracranial aneurysms from three-dimensional (3D) medical images. Despite the many image segmentation methods available, with varying approaches

and algorithms, no dominant method yet exists, in terms of effectiveness, across the cerebral aneurysm. It has been indicated that it is necessary to develop a method in order to accurately segment the cerebrovascular aneurysm; thereby allowing us to measure aneurysm volume, size, and its 3D shape.

Methods: In this thesis, I proposed a new method of segmentation called the Threshold-based Level Set (TLS) method. This method was specifically designed for application in cerebrovascular and cerebral aneurysms, and was based upon the Geodesic Active Contours model and Chan-Vese model (CV), integrating both region and boundary information to segment cerebral aneurysms through the use of a global threshold and gradient magnitude to form the speed function. Validation tests have been carried out to ensure the quality of the proposed TLS method in both 3D CTA scan and 3D DSA scan images. Both in-vivo and in-vitro validation tests were performed. In the in-vivo experiment, forty five aneurysm patients, including vascular and cerebral aneurysm CTA imagery across three locations; the internal carotid artery (ICA), middle cerebral artery (MCA) and anterior communicating artery (AComA), were used for the validation of the TLS method via analysis of the forty five TLS segmented models in terms of geometric shape, volume, and haemodynamic results. In the in-vitro experiment, however, a series of CT scans of silicone aneurysm models were conducted in this study, with four different silicone models and four rates of contrast agent dilution used to generate various image data sets for validation of the TLS method.

Results: The proposed TLS method was found to be able to accurately segment intracranial aneurysms with blurred boundaries, complex cerebrovascular anatomical shapes and inhomogeneous images under automatic conditions. By comparison and contrast to other approaches, the TLS method revealed the highest volume overlap rate (JM), and lowest volume difference (VD), with its most

important advantage featuring its ability to identify the complex local geometry of intracranial aneurysms - extremely important information in clinical application. The results from in-vivo validation showed that the TLS method appears higher in terms of overlap ratio and smaller in terms of volume difference than the other methods for ICA, MCA, and AComA aneurysms. The study likewise indicated that the volume differences and the overlap ratio of TLS may be controlled at a maximum of under 9% and a minimum of over 92% for all aneurysm locations respectively. In-vitro validation results showed that the TLS method was able to achieve over 89% of the volume overlap rate and under 7% of the volume difference across all different degrees of silicone model shape complexities and contrast agent dilutions.

Conclusion: The TLS method is a technique with the ability to automatically segment intracranial aneurysms without the setting of a seed point or intensity threshold, and is likewise available for the segmentation of modifiable anatomical shapes, with blurred boundaries and inhomogeneous images. The TLS method may thus be a useful tool in the assistance of clinical diagnosis and surgical preparation, and play a vital part in the future of computational haemodynamics research.

STATEMENT OF CANDIDATE

I certify that the work in this thesis has not previously been submitted for a degree nor has it been submitted as part of the requirements for a degree to any other university or institution other than Macquarie University.

I also certify that the thesis is an original piece of research and it has been written by me.

In addition, I certify that all information sources and literature used are indicated in the thesis.

. . . . . .

Name Of Candidate

ACKNOWLEDGMENTS

As a mother of two, completing a PhD while juggling family and academic responsibilities have been quite an arduous task and would not have been accomplished without the invaluable support and supervision that my supervisors, colleagues and family afforded me. I am forever indebted to your contributions.

I firstly would like to thank Professor Michael Morgan, his tireless supervision and his expansive expertise and clinical knowledge a real asset to my work, and I wish him well for any of his future endeavours.

I am also extremely grateful for Professor Alberto Avolio, whose support and continuous interest in my project through the provision of my scholarship being of tremendous benefit to me.

Further, I extend my thanks to Professor John Magnussen, whose expertise in medical imaging and CT scanning as well as his input in my experiment assisting me greatly. I know he will be a tremendous asset in any field that he pursues and I wish him well for the future.

Also, a big thank you to Sylvia Priilaid who was also fundamental throughout this project and assisted me with all of my administration paperwork and other documentation for my study, while also being a wonderful friend to have a conversation with.

I also want to thank Dr Wei Sheng Zhang for his assistance in my CT scan, as well as Dr. David Verrelli for his contribution in that experiment, as well as teaching me much about statistical analysis.

Furthermore, I would like to thank both Dr. Jing Long Liu, who taught me how to work the CFD software fundamental to my work, and Dr. Chang-Joon Lee, who never falteringly answered my CFD questions.

I am also grateful to the entire team at Macquarie Medical Imaging (MMI) who have been a wonderful asset and have helped me procure much of the data necessary for my study.

This thanks is also extended IT group at Macquarie University, especially Hans Brabandt, IT support officer for ASAM, without their help in procuring a Matlab license, much of this study would have not been possible.

I also thank all the members both past and present of the Macquarie University CFD group for their support throughout this process.

Lastly, I extend my thanks to my family and friends, especially my husband, Itsu, and my children, Rida and Kenta, who continued their unwavering support and patience all throughout the process, even when I wasn′t in the best of moods. Thank you for putting up with me, and thank you for soldiering on with the housework and other menial chores when I wasn′t able to help.

List of Publications

- Y. Sen, Y. Qian, A. Avolio, and M. Morgan. *Image segmentation methods for intracranial aneurysm haemodynamic research.* Journal of biomechanics vol.47, pp. 1014-9 (2014)

- Y. Sen, Y. Zhang, Y. Qian, and M. Morgan. *Investigation of Image Segmentation Methods for Intracranial Aneurysm Haemodynamic Research.* Modelling in Medicine and Biology X , pp. 259-267, WIT Press (2013)

- Y. Sen, Y. Qian, A. Avolio, and M. Morgan. *Development of Image Segmentation Methods for Intracranial Aneurysms.* Computational and Mathematical Methods in Medicine vol.2013, 7 pages (2013)

- Y. Sen, Y. Qian, Y. Zhang and M. Morgan. *A Comparison of Medical Image Segmentation Methods for Cerebral Aneurysm Computational Hemodynamics.* In Biomedical Engineering and Informatics (BMEI), 2011 4th International Conference on vol.2, pp. 901-904 (2011)

- C J Lee, Y. Sen, H. Takao, Y. Murayama, and Y Qian. *The Effect of Non-Uniform Wall Thickness on Aneurysm Hemodynamic and Mechanical Behaviour: A Fluid-Structure Interaction Study.* Journal of biomechanics (under review, 2014)

- Y. Sen, Y. Qian, A. Avolio, and M. Morgan. *Validation of an Intracranial Aneurysm*

Image Segmentation Method via use of Silicone Models. Journal of biomechanics (under review, 2014)

Contents

List of Figures

List of Tables

Chapter 1

Introduction

1.1 Cerebrovascular Disease

As the centre of coordination for a range of functions, the human brain is supplied by a rich network of blood vessels. These vessels are responsible for the supply and delivery of oxygen and nutrients, as well as the elimination of toxic waste products. The Circle of Willis forms the major centre of this arterial system, branching from the anterior to the posterior regions of the brain vertebral-basilar system [1], as seen in Figure 1.1. Branching from the common carotid arteries, the left and right internal carotid arteries ICA form the structure that supply the majority of the forebrain. These eventually separate into corresponding left and right anterior cerebral arteries (ACAs) (connected by a smaller vessel called the anterior communicating artery (ACoA)) and the middle cerebral artery (MCA). Posterior communicating arteries (PCoA) interconnect the ICAs with their respective left and right posterior cerebral arteries (PCA), which comprise the posterior part of the Circle of Willis.

Cerebrovascular diseases is significant when there is interruption or impediment of cerebral blood flow. Several pathologies contribute to cerebrovascular disease, including

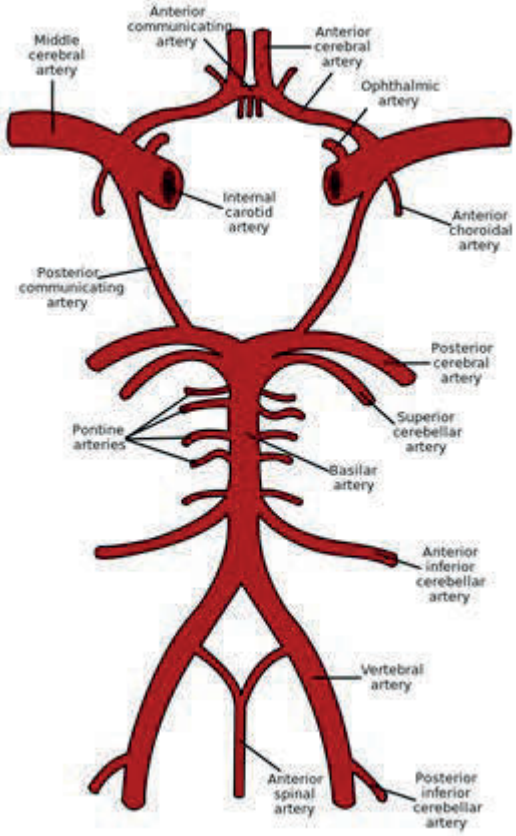

Figure 1.1: The Circle of Willis

the formation of intracranial aneurysms, arteriovenous malformations, or stenosis(e.g. atheromatous disease and dissection).

The focus of this study centres upon intracranial aneurysms. Though the exact mechanisms behind there development, growth and eventual rupture remain uncertain - the formation of aneurysms (i.e. pathological focal dilation of a cerebral artery) results from a weakened internal eleastic lamina of the arterial wall. This can result in the formation of a blister-like out-pouching which may rupture without warning and bleed into the adjacent subarachnoid space surrounding brain tissue (subarachnoid hemorrhage or SAH), or into the brain parenchyma (intracerebral haemorrhage or ICH). The consequences of such haemorrhage can be stroke, coma and potential death. Aneurysms may be typed accordingly to pathophysiological features, including a) saccular, b) fusiform and c) dissecting type aneurysms (Figure 1.2).

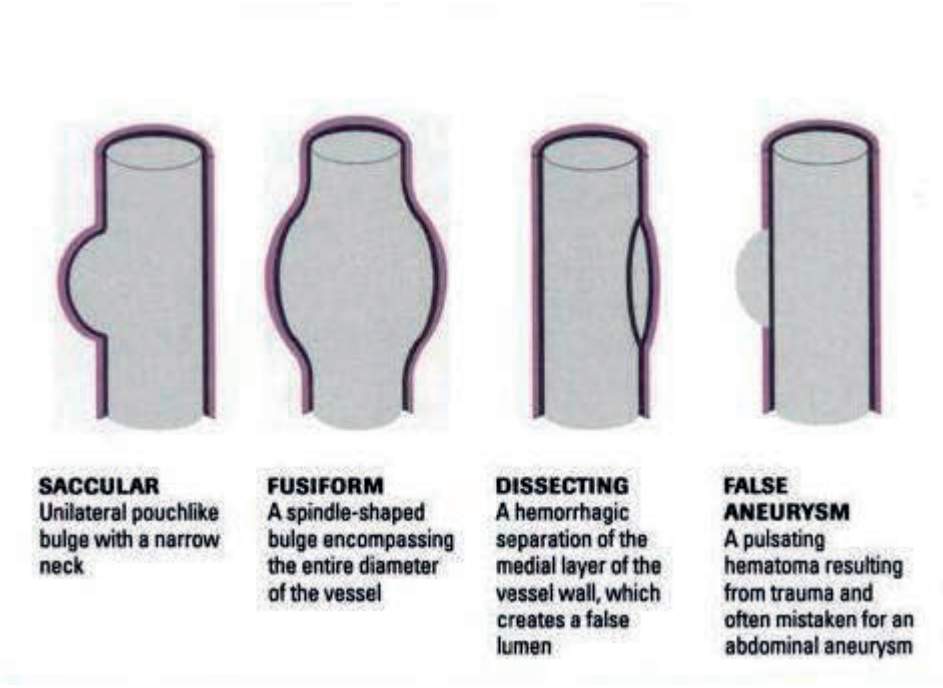

Figure 1.2: Types of aortic aneurysm.

Pseudoaneurysms or false aneurysms may also occur, which are essentially charac-

terized by collections of blood outside the arterial wall, with none of the arterial wall dilatation associated with that of true aneurysms.

Eighty five percent of all cerebrovascular aneurysms occur within the Circle of Willis. The most common sites for aneurysm location are: ACoA (35%); ICA (30%); and MCA (22%) [2]. Approximately 30% of patients with aneurysms will harbor multiple aneurysms [2]. Intracranial aneurysms represent a significant risk to health, with rupture and subsequent SAH linked to morality rates of up to 40% within the first week, and 50% by the first 6 months [2, 3].

The majority of aneurysms cause no symptoms or signs prior to rupture. The proportion of SAH that are caused by aneurysms that eventually rupture is approximately 85% [4].

Currently, two therapies are available to prevent potential rupture. These are, surgical clipping and endovascular coil insertion. The choice of which procedure is recommended is dependent upon aneurysm size and location, as well as external factors including availability of technologies, and physician technique [5].

The primary aim of both techniques is to physically separate the aneurysm sac from cerebral circulation, thereby obstructing blood supply into the aneurysm. During clipping, dissection of the aneurysm from surrounding brain tissue is performed via craniotomy, with clips of varying sizes and shapes in relation to aneurysm size applied to its neck or base. Endovascular techniques have varied over time, with the introduction of proximal balloon occlusion in the 1970s - to the development of the first Guglielmi detachable coil (GDC), approved of by the FDA in 1995 [6]. Success in preventing future rupture is determined by occlusion of the aneurysm sac remaining robust over time.

1.2 The role of medical image segmentation in Intracranial Aneurysms

1.2.1 3D Visualization

In current medicine, greater emphasis is placed upon medical imaging technologies, including CT (computerised tomographic scan), MRI (magnetic resonance imaging) and DSA (digital subtraction angiography) scanning for diagnostic purposes. These are able to visualize anatomical structures to very fine detail, allowing, in some instances, for the imaging of intracranial aneurysms at a sub-millimetre level. These imaging modalities may be combined to yield images to determine both the structural and functional relationships of organs.

Unlike the slice-by-slice method of analyzing traditional film-based or soft-copy "readings "of radiological imaging data, current technologies such as CT, MRI and DSA scanning utilise volume rendering [7–9], surface rendering [10–12] and maximum intensity projections (MIP) [13, 14] to formulate 3D visualisations. This facilitates a greater ability to accurately locate and pinpoint areas of concern in real-time, to better inform the formulation of treatment and management strategies.

Direct volume rendering requires every sample value to be mapped to opacity and colour. One such technique includes volume ray casting. This is effective for the evaluation of tissue structures, to reveal abnormalities in vascular distribution and abnormalities of anatomy - such as aneurysm formations. Its main advantage lies in the measurement of interior data, which allows for more information about spatial relationships between differing structures and organs. The downside, however, is that it is computationally intensive, and it may be difficult to interpret cloudy interiors, and the difficulty of analyzing heavy loads of high-resolution data. In surface rendering, the most common technique

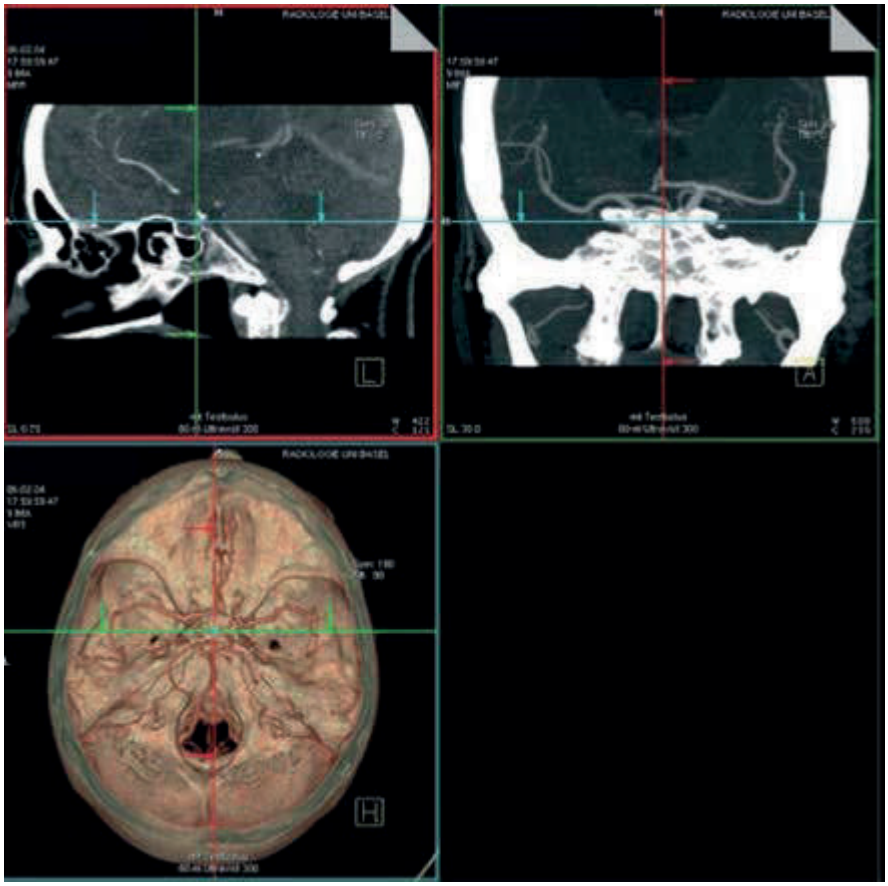

Figure 1.3: Three visualization techniques are displayed. Top left: Multiplanar reformations (MPR) image in sagittal plane. Top right: 30-mm Maximum intensity projection (MIP) slab in coronal plane, centered around the green line as displayed on the image top left (cross referencing). Bottom left: Volume rendering (VR) image

employed is polygon-based rendering, such as Marching Cubes [15, 16]. These generate polygons that are approximate isosurfaces from a volume, which are then rendered via a polygon rendering algorithm. Issues, however, inevitably arise with this method. Though generally faster than volumetric ray casting, a lot of time is required to alter the isosurface of interest, making the method difficult to implement in real time. Moreover, the generation of large amounts of polygons may be difficult to manage upon high-end graphics workstation, and problems may arise with the visualization of the interior of the volumes measured in polygon-based rendering.

Maximum intensity projection (MIP) - a visualization technique often used for blood vessel imaging - projects the highest intensity on each ray onto the corresponding pixel, with grey values calculated via data re-sampling at discrete k locations on rays. Oftentimes, the minimum intensity on a ray may be selected for the visualisation, depending on the dataset and the object to be visualized. One disadvantage however, is the impossibility of following a blood vessel in the foreground, when other structures in the background with higher intensity, cross this vessel.

Segmentation methods must thus be consistent and of sufficient accuracy, to enable to effective utilization of 3D imaging techniques. Despite this, however, no one method can guarantee accurate object definition under all circumstances.

1.2.2 Measurement

Multiple measurements must be made prior to the development of treatment plans for intracranial aneurysms. These include dome-to-neck ratios, the diameter of neck size, the location of the aneurysm, and its shape [17–19].

Obtainment of these parameters has been made easier through recent technological advances in imaging modalities - allowing for improvements in the ability to both describe and quantify more complex geometrical and morphological indices. Aside from volume and

area, other investigated factors include wall undulation, non-sphericity, conicity parameter and ellipticity indexes [20–22], as well as correlation between 2D and 3D features such as volume-to-ostium ratio [23,24] and the spatial relationship between the parent vasculature and the aneurysm itself.

Strong correlations have been found between size ratio index, obtained via extraction of maximal aneurysm height and parent vessel diameter, and rupture risk, with angles of inclination of the aneurysm sac and vessel in relation to the neck plane proposed as an additional morphological parameter - to varying degrees of success. Several semi-automatic computer-aided tools are available for quantitative evaluation of aneurysms [25–28].

1.2.3 Image-guided surgery

In order to prevent the flow of blood into the aneurysm, endovascular procedures can be guided by modern imaging devices [29, 30]. During the coiling procedure, a micro catheter is typically inserted into the arterial system and into the aneurysm itself, led by guide wires. After this, small helical-shaped coils are passed through the catheter and into the aneurysm, to fill and effectively seal it from subsequent blood flow, a procedure guided via X-ray imaging.

1.2.4 Surgical analysis

Cerebral aneurysms typically present in numerous shapes and sizes. Much like size, shape is vital in influencing rupture risk [31]. As such, advances in imaging modalities such as 3D rotational angiography (3D-RA), CT and MR, have made it possible to analyse the complexity of aneurysm shape in a 3D environment, prior to treatment, thereby improving the efficiency and effectiveness of surgical intervention.

1.2.5 Surgical simulation

Image-based neuronavigational systems are now commonly implemented to optimize the accuracy of neurosurgical procedures. These systems involve the use of a workstation and reference arrays or frames, which are connected to a clamp that serves to immobilize the head. These frames utilize passive markers which then reflect infrared flashes, which are subsequently detected via infrared camera systems. Prior to operation, a 3D reconstruction of the patients head is obtained via imaging data - loaded onto the workstation. This is followed by patient-to-image registration, with several fixed reference points on the scalp surface used to map the 3D image produced, to the surface of the patients head. Once this is established, the progress of the surgical approach may then be followed via the use of a probe to a region of interest in the operative field that will be displayed on the workstation screen [32].

Alongside vascular neuronavigation systems, simulation techniques have also been established to optimize the performance of aneurysm clipping procedures. The introduction of virtual 3D models has allowed for anticipation of aneurysm deformations during clip application, thereby influencing decisions surrounding the selection of clips size, number, shape and orientation. Moreover, specific cerebrovascular neuronavigation procedures have been developed with basis upon 3D-CTA or 3D-DSA in order to improve surgical guidance and promote the prediction of the location and orientation of aneurysms within both parenchymal and vascular environments [33].

As segmentation methods have an important role in surgical simulation, it must thus be consistent and of sufficient accuracy, to enable effective utilization in the assistance of surgical preparations for intracranial aneurysms.

1.3 Aims and Motivation

The aim of this thesis is to develop and validate segmentation methods for medical imaging applications. In particular, the main project involves the segmentation of cerebral aneurysms in the brain.

Aim 1: Propose an algorithm, the Threshold-based Level Set (TLS) for cerebrovascular image segmentation.

Aim 2: Develop an automatic robust TLS segmentation software based on the proposed TLS algorithm to improve problems existing in current segmentation technology.

Aim 3: Apply TLS software in the segmentation of intracranial aneurysms.

Aim 4: Validate TLS software using patient-specific aneurysm cases with different sizes and locations.

Aim 5: Investigate the influence of differing segmentation methods upon patient-specific analyses of cerebrovascular haemodynamics.

Aim 6: Validate TLS software using silicone aneurysm models.

The motivation for this work is to increase patient safety by providing better and more detailed information surrounding intracranial aneurysms, in order to optimise image interpretation and medical decision-making process. As knowledge of aneurysm size, location and morphology is essential in surgical intervention planning and performance, this work may assist medical practitioners in the segmentation and characterization of aneurysms, thereby improving both accuracy and reliability.

1.4 Thesis Outline

The thesis is organized into seven chapters. In Chapter 1 and Chapter 2, introduce some background information regarding medical and medical imaging. In Chapter 3, describes common methods and theories on medical image segmentation. In Chapter 4, the Threshold-based Level Set algorithm is proposed. Investigation of image segmentation methods, including TLS method of intracranial aneurysm haemodynamic research is given in Chapter 5. In Chapter 6, presents the validation of TLS method through the use of silicone models. Finally, conclusions of the thesis are discussed in Chapter 7.

Chapter 2

Medical Image Acquisition

There are three types of medical imaging technology commonly used for the diagnosis, evaluation of risks and treatment of intracranial aneurysms; Computed Tomography Angiography (Figure 2.1), Magnetic resonance and Digital subtraction angiography. In this chapter, we briefly introduce some basic concepts behind three medical imaging technologies, including the principles of scanning and imaging reconstruction, and the advantages and disadvantages that each have for the detection of intracranial aneurysms [34–37]. Both medical image data representation format and handling is explained in the last section of this chapter.

2.1 Computed Tomography Angiography

Computed tomographic angiography, or CTA, is one of the key technologies in the field of diagnostic radiology, alongside magnetic resonance angiography or MRA. These two techniques are commonly used in most vascular diagnostic procedures - most recently for the peripheral arteries and the circle of Willis, with the recent development of CTA for imaging of the coronary arteries. Developed in the early 1990s, CTA is a fast and robust technology, allowing for the obtainment of high spatial resolution 3-dimensional images

Figure 2.1: 3D CTA scanner (GE Healthcare, Discovery CT750.)

allowing for the evaluation of both the vascular lumen and the vessel wall surrounding structures. CTA is a minimally invasive medical test which uses a CT scanner to produce detailed images of both blood vessels and tissues. An iodine-rich contrast material is usually injected through a small catheter placed in the vein of the arm. A CT scan is then performed whilst contrast is passed through blood vessels to the various organs of the body.

2.1.1 Type of CT Scan

2.1.1.1 Spiral (Helical) CT

In contrast to conventional CT, the spiral CT does not require a section-by-section scan. Instead, the patient is translated through the scan plane at a uniform speed, during the data collection process (Figure 2.2), using a rotating x-ray tube. An image can be generated from each point along this scanned volume, with sectional images able to be constructed at arbitrary levels. Furthermore, additional images can be overlapped as needed, without the need for further scanning and hence increased exposure to radiation.

2.1.1.2 Multislice CT

Utilising third-generation technology and with the addition of two or more synchronously rotating detector arrays, alongside solid state detectors, the multislice CT is employed for the generation of multiple image slices in parallel. As many as 1000 detectors are positioned in the long dimension along the semicircular detector arch, with typically 16 or more located in the shorter dimension tangential to this arch. The number of detectors determines the number of image slices made producible by the multislice CT equipment - with 6, 8, 10, 16, 64, 128 and 320 detector array systems made available (Figure 2.3).

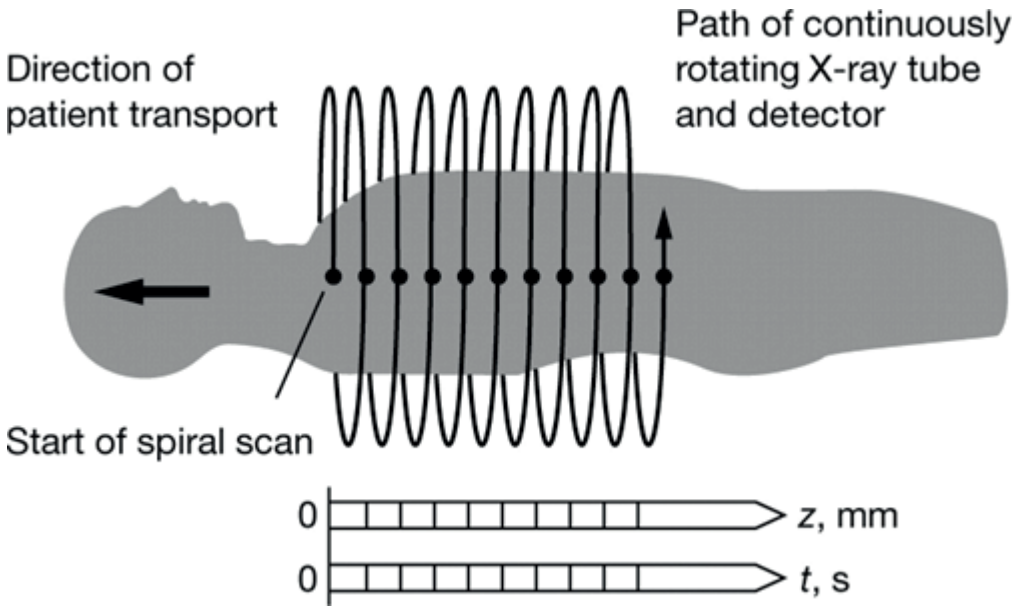

Figure 2.2: Principle of spiral CT scan.

2.1.2 Basic Concepts of Computed Tomography

2.1.2.1 Scanning Principle

The CT scan is a medical imaging procedure that utilizes x-ray and computer-generated technologies to produce two or three-dimensional images of the body. During the imaging process, the patient is typically placed between the x-ray source and detector. The intensity of attenuated radiation, or the degree of x-ray absorption by the body, is detected via the use of thin, semicircular digital detectors located within the scanner. Using mathematical image reconstruction (inverse Radon transformation), we are able to use this raw data - the degree of x-ray absorption found along each of the many paths through the body - to calculate local attenuation at each point within the acquisition volume. Local attenuation coefficients are normalized to produce CT numbers for every point of the image matrix. Measured in terms of the Hounsfield unit (HU), a CT number is assigned to each voxel, according to the degree of attenuation found in that particular voxel. The degree of x-ray absorption is proportional to the density of tissue, with higher densities

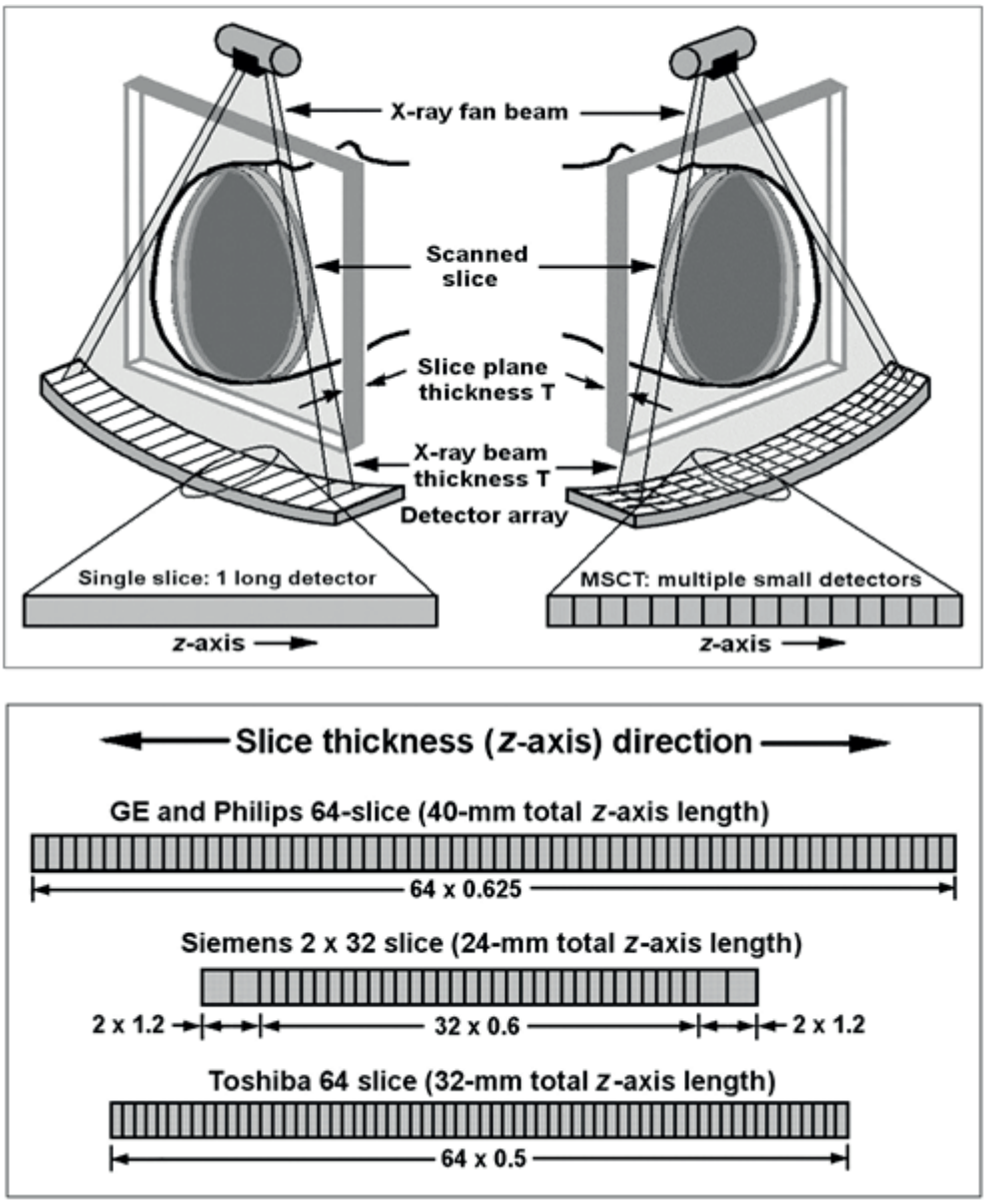

Figure 2.3: Principle of multislice CT scanners : A thin fan-shaped beam rotates around the body and is detected by more than two synchronously rotating detector array. Diagrams of various 64-slice detector designs (in z-direction). Most designs lengthen arrays and provide all submillimeter elements. Siemens scanner uses 32 elements and dynamic-focus x-ray tube to yield 2 measurements per detector.

associated with greater CT numbers. Water, the medium on which this scale is indexed, is always 0 HU, with bone found to be approximately 1000 HU. There is, however, no upper limit, with the available range of CT numbers varying accordingly with the scanners used and the number of bits available per pixel.

In order to obtain numerical values of convenient size, and to avoid dependence on the energy of the radiation, the CT number is defined mathematically as: CT number $= 1000 \times (\mu - \mu_{water}) / \mu_{water}$ Where μ is the linear attenuation coefficients of tissue and μ_{water} is the linear attenuation coefficients of water. Following the collection, this data is compiled to form x-ray projections of images of very thin, transverse slices of the body [38–41].

2.1.2.2 Image Reconstruction

The processes behind image reconstruction are illustrated in Figure 2.4. Detector signals registered during each scan are preprocessed to compensate for the heterogeneities present within the system. It is only after various correctional steps and transformation from signal intensities into x-ray attenuation values that this data is called the CT raw data - used to yield the image data set. Image reconstruction typically starts with selection of the desired field of view. Each ray passing through this field of view is used for reconstruction, with the attenuation value for each image point determined via use of the average of attenuation coefficients for all rays crossing this point - a process termed “back projection”. This type of projection however, produces non-sharp images with blurred edges, with resulting attenuation profiles subjected to an edge-enhancing mathematical filtering process called “convolution”. The type of filtering process used is determined by “convolution kernels”or reconstruction algorithms. These are used to alter the properties of reconstructed CT sections in terms of spatial resolution and image noise.

For third and fourth generation scanners, raw-data sets contain around 500 - 2300

projections for each 360^o rotation of the x-ray tube. In turn, each projection is comprised of approximately 500 - 900 single attenuation values, with image reconstructions from this raw data finally yielding the image data set.

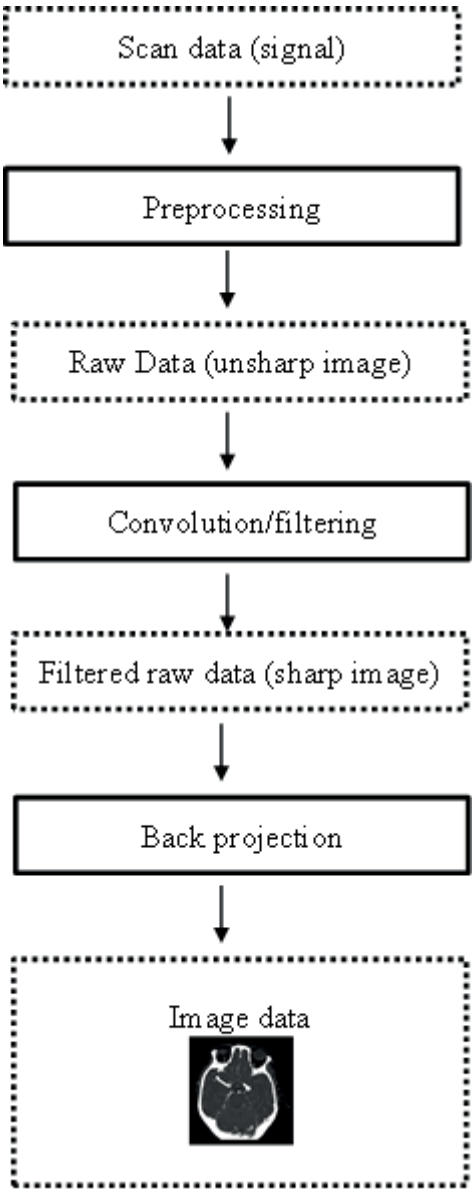

Figure 2.4: Processes involved in CT image.

2.1.2.3 Parameters

2.1.2.3.1 Window Settings Only a portion of the CT scale is displayed. This is due to 2 main reasons. The human eye is only able to distinguish between a limited range of colour shades. Thus, there is no need to assign the complete diagnostic range of CT numbers to the available range of grays, in distinguishing between differing structures. This window is defined by its width, which affects image contrast and level (center), which affects image brightness.

2.1.2.3.2 Artefacts in CT Scan Artefact is used to describe any discrepancy between the true attenuation values of the object and the CT numbers obtained from the reconstructed image. With images produced via CT more prone to artifact than those obtained via conventional radiography, due to reconstruction from a million separate detector measurements. Artefacts can be categorized into 4 groups: a) streaking, due to inconsistencies in a single measurement, b) shading, c) rings, d) distortion - due to helical reconstruction

Many things may cause the appearance of artefact. Physics-based artefacts arise due to physical processes involved in the data collection process whilst patient-based artefacts are caused by patient-dependent factors such as movement and the interference of metallic materials. Scanner-based artefacts arise due to imperfections in scanner function, whilst helical and multi-section artefacts are caused by errors in image reconstruction [42–44].

2.1.3 Computed Tomographic Angiography in Detection of Aneurysms

Computed tomographic angiography, or CTA (Figure 2.5), is a medical imaging technology used to visualize arterial and venous vessels throughout the body. One of its key advantages lies in its ability to visualize smaller vessels, including those of the Circle of Willis; the anterior choroidal and lenticulostriate, and the perforating arteries at the

ACoA and apex BA. Calcium deposits in the wall of aneurysms may also be detected via CTA, allowing for the visualization of thrombus formations in relation to vessel walls. This has important implications for treatment planning [45].

CTA, however, is unable to visualize collateral flow patterns, with the imaging of smaller vessels (<0.5 mm diameter) not recommended, should they influence therapeutic approach and design. CTA following conventional CT imaging is performed to optimize outcomes for cases involving potential aneurysmal SAH. However, for cases featuring hard to identify or unclear delineation of the aneurysmal growth, due to insufficient technical expertise - DSA may be employed until greater technical skill in CTA operation is gained. Most patients can be easily and comfortably treated without DSA [46].

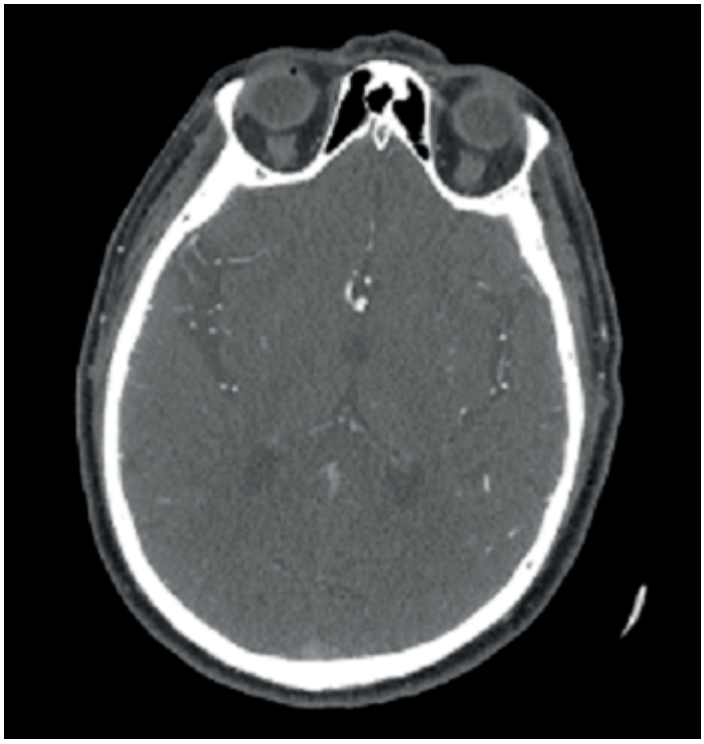

Figure 2.5: Computed tomographic angiography of the cerebral arteries.

2.2 Magnetic Resonance Angiography

Magnetic resonance angiography (MRA) involves the use of radiofrequency waves and magnetic field gradients in production of images. In response to the varying hydrogen densities and reaction to magnetic field gradients, a range of pulse sequences are administered upon tissues to either enhance or reduce these waves. These sequences include phase-contrast angiography (PC), time-of-flight angiography (TOF) and 3D contrast-enhanced MRA.

2.2.1 Type of MRA

2.2.1.1 Time of Flight and Phase contrast Magnetic Resonance Angiography

Tissues and structures within the slice of interest are saturated with repeated radio frequency pulse waves during time of flight magnetic resonance angiography (TOF-MRA) (Figure 2.6). In comparison to the stationary nature of tissue, blood flows are not subject to these radio frequencies. They thus maintain their signal intensity, and allow for the creation of a contrast between the dynamic nature of the inflowing fluid, and its static background. Limitations of this technique, however, include the impact of signal losses distal to stenosis due to turbulence, and the longer acquisition times involved.

2.2.1.2 Phase-contrast Magnetic Resonance Angiography

Utilising velocity-induced phase shifts which move protons via bipolar flow-encoding gradients, phase-contrast angiography (PC-MRA) is able to generate images of both static and non-static structures, with both two and three-dimensional techniques available (Figure 2.7). Though turbulent flow may continue to cause the occurrence of artefacts at the site of vessel stenosis, signal losses distal to this is minimized via the use of PC-MRA, when compared to TOF-MRA. Both TOF-MRA and PC-MRA are utilized in cases wherein pa-

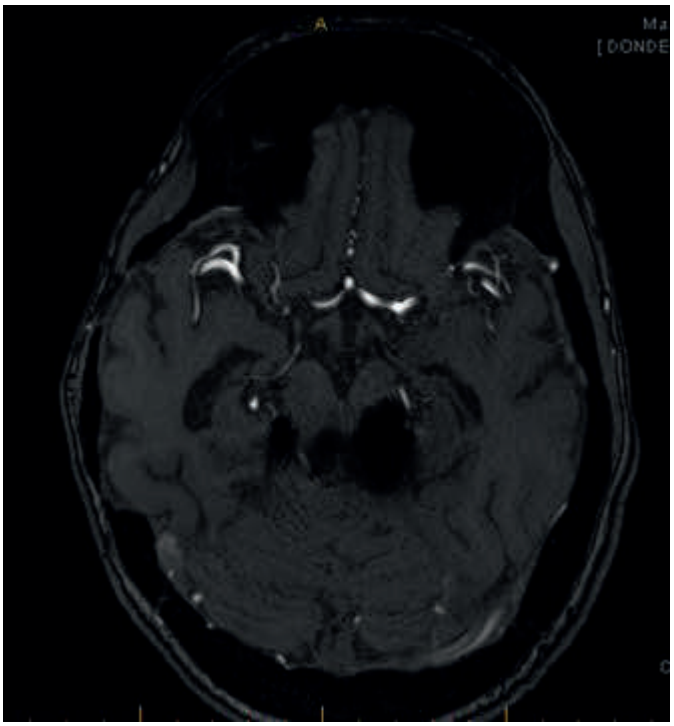

Figure 2.6: Time of flight magnetic resonance angiography of the cerebral arteries.

tients are found to have contraindications to gadolinium infusion - a contrast medium used in the conduction of MRA scans.

2.2.1.3 Contrast-enhanced Magnetic Resonance Angiography

3D contrast enhanced MRA (CE-MRA), has emerged as an accurate and efficient technique for the imaging of vascular structures without the limitation of previous techniques. Combining the enhanced tissue contrast obtained with conventional MRI techniques, CE-MRA is able to provide a 3-dimensional image that may be rotated 360 degrees for improved evaluation following post-processing. Gadolinium chelate, a paramagnetic contrast, is infused via intravascular injection to shorten the T1 relaxation time of blood, in comparison to surrounding tissue. This technique is less flow sensitive, as the signal of blood flow is often times based upon intrinsic T1 signals and less upon flow effects.

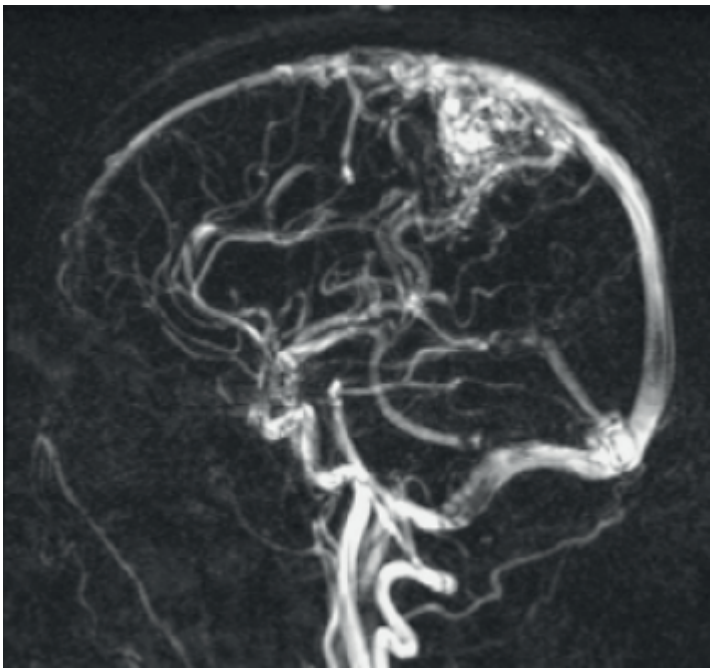

Figure 2.7: Phase-contrast magnetic resonance angiography of an arteriovenous malformation.

Increased spatial resolution can increase scanning times. The post-processing process can allow for the production of maximum intensity projection (MIP) images. Unlike TOF-MRA or PC-MRA, intravascular signals are dependent upon T1 relaxation and not inflow or phase-accumulation, resulting in the reduction of in-plane saturation and turbulence-induced signal loss. Careful timing of the contrast bolus is likewise necessary to ensure higher concentrations of gadolinium at the desired station, during the image acquisition process.

2.2.2 Basic Concepts of Magnetic Resonance Angiography

2.2.2.1 Scanning Principle

MRI scans may be used to produce images of the nuclei of atoms which contain an odd number of protons and/or neutrons. One nucleus which satisfies this criterion, is that of

the hydrogen atom - comprised of a single proton. With a magnetic dipole, the hydrogen nucleus is able to interact and align or antialign with the strong magnetic field generated via the MRI. Coupled with its abundance in the body, the net sum of the magnetic dipole moments from a group of these atoms will result in a bulk magnitisation that is aligned with the transverse or applied magnetic field (Figure 2.8).

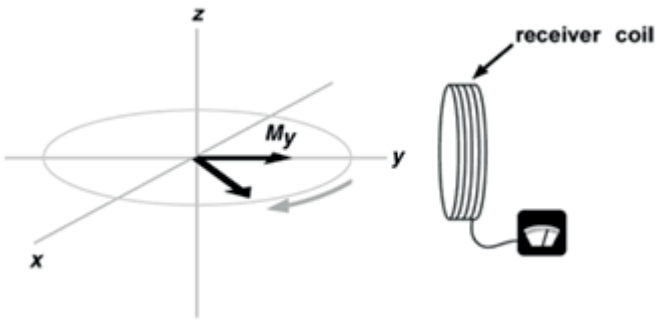

Figure 2.8: The bulk magnetization, M, rotates, or precesses, when it is transverse. The receiver coil detects an oscillating signal from the component of magnetization (My) that points toward it. The rate of precession and the frequency of the signal are proportional to the strength of the magnetic field. In this diagram, the magnetic field is aligned along the z-axis.

Maximum signals are generated when the longitudinal or aligned magnetization is slanted at 90 degrees, perpendicular to the direction of the applied magnetic field Magnetic field gradients that alter with position are superimposed upon the spatially uniform magnetic field upon imaging, with the resulting spatially varying fields produced causing the bulk magnetization at differing locations to process at varying speeds. Transverse magnetization at different locations will thus result in signals with varying frequencies. Based on these frequencies, magnetic field gradients are then mapped to their proper positions in all three dimensions, during the image reconstruction process. Signal intensities of magnetic resonance vary depending upon numerous factors, with a host of protocols that may be altered in order to accentuate or diminish the influence of these factors on

the produced image.

One factor that influences signal intensity is the amplitude of the transverse component of magnetization. Transverse magnetization will decay or diminish exponentially with time, with the rate of decay marked by the time constant, T2. This rate of decay is dependent upon the microstructure of tissues surrounding the magnetic dipole moments that make up the bulk magnetization. Differing tissues possess differing T2 decay times, with shorter times indicating a faster rate of transverse magnetization deterioration, and longer times indicative of a slower rate of decay. By allowing time to elapse between the transverse rotation of the magnetization, and its detection - signal differences from tissues with distinct T2 decay times are obtained. The time from this transverse tipping to signal detection is controlled by an imaging parameter called TE or echo time. As scans with longer echo times are able to accentuate signal differences due to variations in T2 decay times, these images are referred to collectively, as T2 weighted.

Other factors that affects signal intensity is the magnitude of longitudinal magnetization. Following transverse tipping, the longitudinal component of magnetization will undergo exponential regrowth. This rate of regrowth is marked by a time constant called T1. This regrowth rate depends upon the microstructure of the tissue surrounding the magnetic dipole moments. As differing tissues possess dissimilar microstructures, they possess differing T1 regrowth times. In MRI, the longitudinal magnetization can be tipped multiple times in order to encode enough information to map signals to the proper locations in the image.

If a short period of time elapses between the application of one tipping pulse and the next, the longitudinal magnetization does not fully regrow. Moreover, longitudinal magnetization from short T1 tissues regrows more than the longitudinal magnetization seen from tissues with longer T1. Thus, allowing only a short amount of time to elapse between tipping pulses ensures that differing amounts of magnetization are tipped transverse. This

results in generation of distinct signals from different tissues based on variations in T1 regrowth times. The time between tipping pulses is controlled by the parameter, TR or repetition time. Since scans with shorter repetition times exacerbate signal differences based upon variations in T1 regrowth times, these images will be referred to as T1 weighted. In order to minimize T2-weighting in these scans, the shortest possible echo time is used. In cases when a long TR and short TE are used, the signal no longer becomes dependent on T1 or T2 differences.

Alongside this, signal intensity is likewise influence by a multitude of factors like temperature, diffusion, the strength of magnetic field, motion, and the injection of a T1-shortening contrast material [47–50].

2.2.2.2 Limitation of Magnetic Resonance Angiography

Patient cooperation is of utmost importance for the obtainment of high-quality images, as patient-dependent artefacts may arise due to inadequate breath-holding or unplanned motion. At times, conscious sedation and/or general anesthesia may be necessary prior to scanning, to optimize image-quality for particular patients - ie: claustrophobic patients who may suffer symptoms of anxiety. Moreover, patient body size may limit the ability of participants to undergo MRA, due to size and weight limitations carried by most scanners.

MRA, in particular CE-MRA, is contraindicated in patients with a history of renal disease. The use of gadolinium-based contrast has been implicated in various nephrogenic conditions including nephrogenic systemic fibrosis - a systemic and fibrotic syndrome with potentially fatal consequences. Those afflicted typically present with progressive fibrosis and hyperpigmentation of the skin, with varying degrees of visceral. The risk of this is exacerbated amongst patients suffering from end-stage kidney disease.

Moreover, metallic implants such as stent devices may exhibit signal dropout following MRA scanning, due to magnetic susceptibility and radio frequency shielding. This may

potentially impact the accuracy of imaging for vessels with previously-implanted stent devices. MRA is likewise contraindicated for patients with magnetic, electrically conductive or RF-reactive implants, including pace-makers and defibrillators. Titanium implants, however, are generally considered safe.

2.2.3 Magnetic Resonance Angiography in Detection of Aneurysms

3D TOF-MRA has been found to be more effective than the 3D PC-MR technique in evaluation of aneurysms [51]. As with CTA, use of both two and three-dimensional imaging display modalities is recommended to optimize this process. Lower aneurysm detection rates are found for MRA, than compared to the DSA or CTA imaging techniques, particularly for smaller aneurysms (<3 mm).

Moreover, though less accurate quantification and lesion characterization are likewise found [52–54]. New strategies using CE-MRA have shown promising results.

This is due to several factors, including lower image resolution when compared to modern multi-slice CTA imaging, with the saturation of slow-flow and intravoxel phase dispersion in the presence of turbulent flow oftentimes leading to incomplete delineation on three-dimensional TOF-MRA imaging (Figure 2.9). Diagnostic difficulties might arise from a high signal artefact - such as the mimicking of flow signals by intraluminal thrombi or hematomas surrounding recently ruptured aneurysms [55, 56].

Applied as both a rapid first-pass technique and steady state technique, CE-MRA has been found useful in the delineation of thrombi from patient lumen in large aneurysm growths - though its reliability has been reduced for aneurysms of smaller size [57, 58]. Further improvements in aneurysm detection may be achieved via higher signal-to-noise and resolution. When used in combination with parallel imaging techniques such as sensitivity coding (SENSE), new synergies are now made possible [59].

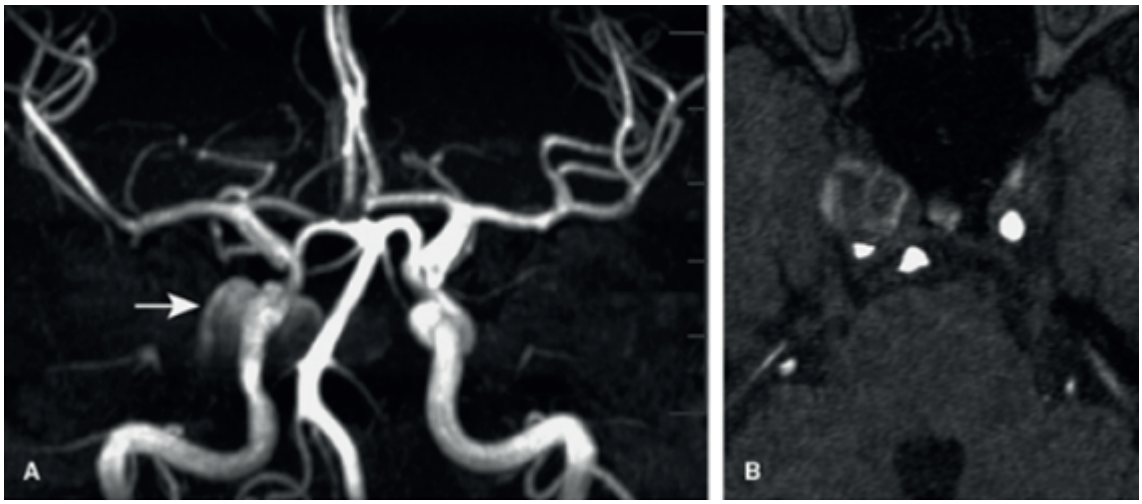

Figure 2.9: TOF-MRA of a giant intracranial aneurysm (A) 3D TOF MRA MIP image and (B) source image of the patient with a large aneurysm. The aneurysm can be detected (arrow), but is an incomplete delineation of the aneurysm.

2.3 Digital Subtraction Angiography

2.3.1 Basic Concepts of Digital Subtraction Angiography

DSA has long been considered the gold standard for the generation of high-resolution images of the vascular system (Figure 2.10). This involves the recording and processing of a fluoroscopic image in order to mask the radiodensities of vessel wall and surrounding tissues. Once this subtraction is performed, the image is made exclusively of the subsequent local injection of intraluminal contrast. Any movement after this initial subtraction image results in motion artefact and image deterioration, and a new mask image must be obtained prior to the injection of contrast. Although iodinated contrast materials are most common, alternative agents such as gadolinium or carbon dioxide, can also be utilized [60–62].

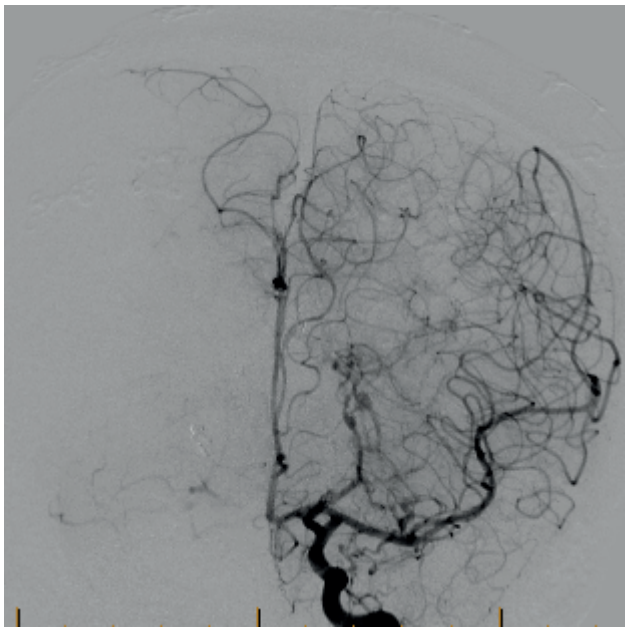

Figure 2.10: Digital subtraction angiography of the cerebral arteries. Several advantages exist for DSA over less invasive modalities such as CTA and MRA. Techniques including road mapping allow for a previously recorded image of a contrast-filled vessel to be viewed on a monitor, whilst angiographic wires and catheters are passed through this image in real time.

2.3.2 Limitations of Conventional Angiography

One of the main limitations is the invasive nature of conventional angiography, which requires percutaneous vessel cannulation, alongside use of intravascular wires, sheaths, catheters and other devices. Complications may also arise, including the rupture, dissection or thrombosis of vessels. Formation of pseudoaneurysms, and arteriovenous fistulae. The facilities and technical operating skills required for conventional angiography make this method the most expensive, over the other non-invasive techniques described. However, though most imaging modalities entail the use of contrast agents, which may be nephrotoxic and allergenic, a substantially lower amount is used when compared to techniques including CTA, where larger defined boluses are required for optimal vessel opacification.

2.4 Comparason of CTA and DSA in Detection of Aneurysms

Recent studies have supported the use of CTA as an effective initial imaging technique for the suspected detection of intracranial aneurysms. High sensitivity and specificity has been found for CTA (Sources), particularly amongst patients harbouring smaller-size aneurysms. The advantage of CTA over DSA in aneurysm detection lies in its ability to distinguish the presence of mural calcification and intracranial thrombi, as well as determine the relationship of the aneurysm to the adjacent bony structures, and its orientation in relation to intraparenchymal hemorrhage [63,64]. When aneurysms are concealed however, due to the presence of adjacent surgical clips or bony structures, the ability of CTA to distinguish smaller vessels diminishes [65].

2.5 Image Representation and Handling

Acquired 3D images, oftentimes in the form of multiple 2D image stacks, are stored on workstations linked to the scanners, which must be transferred to calculators for data processing. Presented by greater than 256 gray levels, 8-bit image formats, such as TIFF, must be handled by specialized image-editing software tailored to the representation of medical data. The need for a standard manner for the communication and translation of medical images is due to the vast array of patient and investigator variables that must be gathered in the acquisition process - including the time of acquisition, acquisition modality and scan parameters, and image number, position and resolution. This system, called Digital Communication in Medicine or DICOM, is the international standard for medical images and related information (ISO 12052) - defining the formats for images with the data and quality necessary for clinical use. Utilised in tens of thousands of imaging devices, including radiology, cardiology and radiotherapy devices including CT and MRI, DICOM has allowed for the replacement of conventional forms of imaging with a fully digitial workflow [66–68].

2.5.1 DICOM File Structure

DICOM file has two parts consisting of header and data set. The Figure 2.11 shows the basic file structure.

2.5.2 File Header

The header, which may or may not be included in the file, is comprised of a 128 byte File Preamble, followed by a 4 byte DICOM prefix. This standard does not require any structure for the fixed size preamble, and does not need to be structured as a DICOM data element with a tag and length. The intent of this file header is to facilitate access

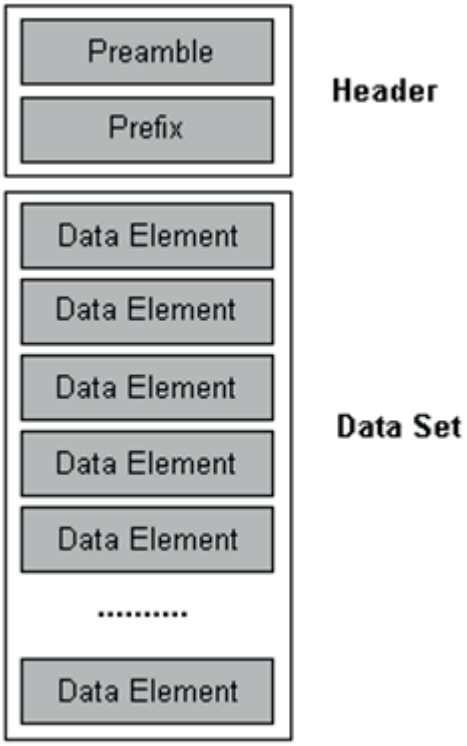

Figure 2.11: DICOM file structure.

to the data contained in the DICOM file by providing compatibility with a number of commonly used computer image file formats.

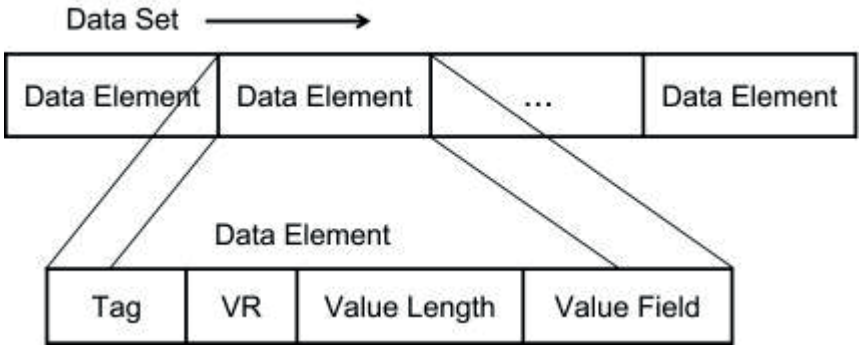

Figure 2.12: DICOM data set structure.

2.5.3 Data Set

The data set (Figure 2-11) represents a slice of the larger population, and is constructed of data elements, made up of 4 parts. These include the data element tag, value representation (VR), value length and value field.

Data Element Tag: an ordered pair of 16-bit unsigned integers representing the group number followed by the element number, like (XXXX,YYYY). It uniquely identifies the Data Element.

VR: A two-byte character string, which describes the data type and format in Value Field.

Value Length: a 16 or 32-bit unsigned integer, which shows the length of Value Field.

Value Field: the stored information DICOM data model is described by information object definition (IOD).

Though the Data Element Tag is often simple and conspicuous, its readability may be limited, with only standard Data Elements able to be understood with the assistance of a Data Dictionary.

Chapter 3

Medical Image Segmentation

Medical image segmentation is aimed at the extraction of targeted objects (organs, tissues) from images. This chapter will briefly present the most common categories of image segmentation methods used in the medical image segmentation process. We will introduce first the techniques of thresholding and region growing, before focusing upon more modern techniques prevalent throughout the field of medical imaging which a segmentation is found by means of optimizing an energy functional. In this context we talk about boundary based, region based and hybrid methods. The strengths and limitations of various image segmentation methods will also be explored.

3.1 Thresholding and Region Growing

As one of the fastest and most simple of region-based techniques, thresholding utilises a single threshold value to identify and produce images of objects. Values above and below this pixel are classified as object and background pixels respectively. Thresholding works well for high-contrast objects with a sharp edge, though the method often fails using smooth and non-homogenous images, influenced by background noise. Unfortunately, this is oftentimes the case for medical images, thereby limiting the utility of this research in

medical imaging.

A more sophisticated version of thresholding includes the use of region growing algorithms. This begins with use of a given seed point, known as an object pixel. The region surrounding the pixel is classified as background or object, depending upon a threshold value determined by reasonable criteria. This object is then segmented via filtering through the pixels which may be classified as "object". Issues however, surround this method, most notably the leakage of pixels, as it is difficult to establish a threshold value that can serve to confine an actual object.

3.2 Deformable Contour Methods

The underlying tenet of this method is the definition of an energy functional for the production of a continuous curve or surface, which includes both external energy from the image data, and internal energy from the curve or surface itself, as input. Following this, calculation of variations are made, and the energy functional minimized to produce the expected segmentation result.

3.2.1 Snakes

The Snake was introdused by Kass et al. [69], this technique involves the use of an explicit type of curve energy. In this, the curve deforms to minimize curve energy - including both external energy derived from the image, and internal energy derived from the curve itself, via use of a variational method. This energy is defined by:

$$E\left[C\left(s\right)\right] = -\int_0^1 \left|\nabla I\left(C\left(s\right)\right)\right|^2 ds + \alpha \int_0^1 \left|C'\left(s\right)\right|^2 ds + \beta \int_0^1 \left|C''\left(s\right)\right|^2 ds \qquad (3.1)$$

where $C(s)$ is a parametric curve with parameters, I is the image, and $C'$and $C''$are the first and second derivatives of C with respect to its parameters. The first term is referred

to as external energy, whilst the last two terms represent the internal energies of the snake. Whilst the external energy is used to drive the curve towards points with high-magnitude gradients (ie: images featuring strong edges), the first internal energy, weighted by $\alpha \geq 0$, forces the curve to become continuous and the second, weighted by $\beta \geq 0$ forces the curve to become smooth. The minimization of the first internal energy causes the curve to shrink, and the points along the curve to become equidistant with one another. Minimisation of the second energy reduces curvature difference, thereby smoothing out the curve. One of the most well-known numerical methods for energy minimization is the Euler-Lagrangiane equation, denoted by $\partial E/\partial C = 0$. Application of this equation results in a partial differential equation (PDE), which may be solved through use of a finite-difference or finite-element method. This is the basic principle behind the popular deformable curve methods used in image processing, though all solutions produced would be location-specific - with results strongly dependent upon use of a proper starting curve and proper initialization.

The Snakes algorithm was the first to utilize variational methods for image segmentation. However, the technique suffers from a number of drawbacks, most notably, the problem of explicit curve representation. Topological changes are not easily accommodated in this method, and complex re-parameterisation algorithms are often times necessary. Moreover, the nodes of the curve may be affected by local image features, including image noise, with solutions particularly sensitive to proper initialization. Difficulties may also arise in regards to specification of parameters used in the energy function.

3.2.2 Level Set Methods

In the face of difficulty of handling topological alterations, a non-parametric deformable contour method - or level-set method, was proposed by Caselles et al. [70] and Malladi et al. [71] in an effort to address this issue. This method originates from the the-

ory of propagating solid/liquid interface (front) with use of a curvature-dependent speed, as proposed by Osher and Sethian [72].

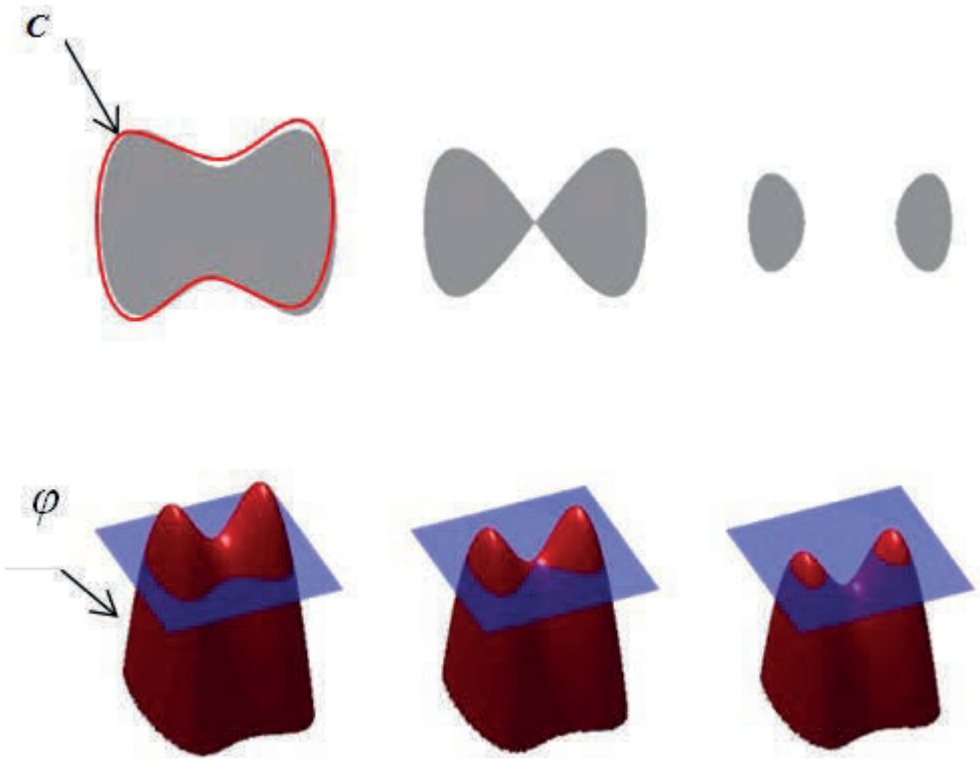

Figure 3.1: The red surface is the graph of a level set function $\varphi = 0$, and the flat blue region representing the x-y plane. The boundary of the shape is then the embedded curve C.

In the level set method, a curve or surface C(t) is implicitly represented as the zero level set of a time dependent function φ: $\Omega \to R$, by $C(t) = \{x, y \in R \mid \varphi(x, y, t) = 0\}$. This curve or surface is then deformed by the function:

$$\frac{\partial \varphi(t)}{\partial t} = -F\vec{n} \tag{3.2}$$

The Eq.3.2 is a partial differential equation,or a Hamilton-Jacobi equation in particular, this may be solved via use of finite differences on a Cartesian grid. The advantage of level set method lies in piece-wise continuity and the handling of topology through the implicit

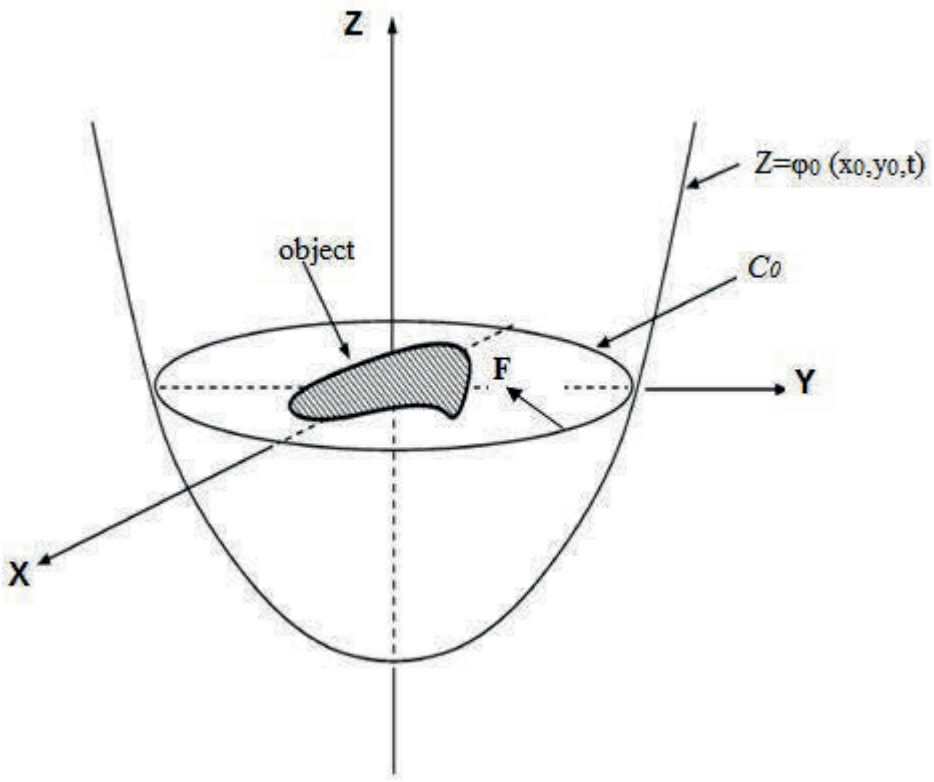

Figure 3.2: φ_0 presents an initial level set function φ, $C_0 = \varphi_0 = 0$ is the initial boundary of the embedded curve C, a speed F drives the curve C in the normal direction toward the object.

zero level set function. The major setbacks of level set methods, however, lie in their computationally expansive nature, due to the need for iterative optimization methods in the solution of complex PDE (partial differential equation).

3.2.3 Geodesic Active Contours

With basis upon the level set method, the geodesic active contour was simultaneously proposed by Caselles et al. [73] and Kichenassamy et al. [74]. The geodesic active contours unified the curve evolution approaches with the classical energy minimiazation methods (snakes). It was proven that the minimization of a simplified contour energy with no second order term in Eq.3.1 is equivalent to the minimization of the contour length weighted by an edge detection function in Riemannian space. The energy to be minimized is represented in the following form:

$$E_{GAC}\left[C\left(s\right)\right] = \int_0^{L(c)} g\left(\left|\nabla I\left(C\left(s\right)\right)\right|\right) ds \tag{3.3}$$

where $L(C)$ is the length of C, $g(\nabla I)$ is a strictly decreasing inverse edge indicator function, typically $g(|\nabla I|) = 1/(1+|\nabla I|^2)$. In order to minimize Eq.3.3, the curve evolution equation $\frac{\partial C(t)}{\partial t} = g(I)\kappa\vec{N} - (\nabla g \cdot \vec{N})\vec{N}$ should be applied, where κ is the Euclidean curvature and $\vec{N}$ represets the unit inward normal. If the planar curve C evolves according to $\frac{\partial C}{\partial t} = \beta\vec{N}$, for a given function β, then the embedding function φ should deform according to $\frac{\partial \varphi}{\partial t} = \beta|\nabla\varphi|$, where β is computed on the level set. By embedding the evolution of C in the φ, topological changes of $C(t)$ are handled automatically, thereby ensuring accuracy. Solving the geodesic problem is thus equivalent to finding the solution $\frac{\partial \varphi}{\partial t} = 0$ for the following evolution equation:

$$\frac{\partial \varphi}{\partial t} = |\nabla\varphi| div\left(g(I)\frac{\nabla\varphi}{|\nabla\varphi|}\right) \tag{3.4}$$

The geodesic active contour model provides a coupling between segmentation based on energy minimization and the level set framework. Whilst a rigorous mathematical

approach is necessary for its optimization, the curve representation is flexible and robust, allowing for both analysis and practical application.

3.2.4 Active Contours without Edges

With reliance of both classical approaches and active contour models upon the edge function in relation to the image gradient, these techniques are limited to detection of objects defined by its respective gradient. This is oftentimes problematic due to variations in edge contrast and noise. Models may fail when applied to objects with blurred or weakened edges, with the risk of leakage occurring if the edge is not well defined. Region-based active contour modelling was introduced by Chan & Vese [75], which allow for the detection of contours with and without gradient. A stopping term, as introduced in by the Mumford-Shah segmentation technique, is adopted in this model, with the entire curve evolution conducted under the level-set framework. Under the assumption that only two regions exist in which segments are constant piecewise, this model also operates for generalized input cases, where pixels conform to Gaussian distributions both within and outside of the desired segmentation. One of the advantages of the active contour model is its ability to segment blurred or discontinuous boundaries, and the ability for the initialization process to be initiated at any point within the image. Interior contours are moreover detected automatically. The active contours model is a special case of the Mumford-Shah functional for segmentation. Through this, the minimal partition problem may be addressed, which aims to find a partitioning of the image which best separates the interior of the curve from the exterior. This may be described as:

$$E_{CV}[C(s)] = \mu \int_0^{L(c)} ds + \iint_{\Omega_c} (I(x,y) - c_1)^2 dxdy + \iint_{\Omega \setminus \Omega_c} (I(x,y) - c_2)^2 dxdy \quad (3.5)$$

where Ω_c is the interior of the curve C, c_1 and c_2 are the average image intensities in the interior and exterior of C respectively and $\mu \geq 0$ is a weight parameter. The first term

is a regularization which serves to minimizes the length, whilst the second and last terms provide the balancing between the interior and exterior values. The image is separated into two regions or phases, approximated by constant values c_1 and c_2, and when $\mu = 0$ the first term disappears, and the Chan-Vese method becomes a simple thresholding method by the threshold $(c_1 + c_2)/2$ [76]. The main advantage of this model is the global dependence and the tendency to produce globally optimal solutions in practice. However, the influence of background intensity may cause difficulties in the utilization of active contours models for medical image segmentation.

3.3 Hybrid Methods

The segmentation methods identified in this chapter are classified into three broad groups according to the use of image features: region-based, boundary-based and hybrid. Of these methods, the thresholding, region-growing and Chan-Vese active contour models are region-based, the main disadvantage of these involving their inability to segment images that feature non-homogenous intensities. Boundary-based methods include the snake and geodesic active contour models. The disadvantage of these models is the data leakage that may occur in the case of blurred or very smooth boundaries.

Hybrid methods, on the other hand, are driven by both region and boundary-based information, and have to date achieved great success in the field of medical image segmentation. The main reason behind their success lies in the ability of these methods to simultaneously combine accurate and specific local information, with more robust, global information, to produce the final segmented image.

3.3.1 Robust Active Contour with Local Median

The Chan-Vese active contour model is based upon two assumptions that surround image pixel properties. First, it is assumed that intensity values conform to a Gaussian distribution within each region, and second, that the global mean or average intensity value vary across differing regions and hence may be utilised in discriminating between pixels. These two assumptions, however, are often times violated in reality, resulting in segmentation leakage or misclassification. A new method which employed local medians as opposed to a global mean, was thus proposed by Liu [77], represented as:

$$E[C(s)] = \mu \int_0^{L(c)} ds + \iint_{\Omega_c} (I(x,y) - f_1)^2 dxdy + \iint_{\Omega \setminus \Omega_c} (I(x,y) - f_2)^2 dxdy \qquad (3.6)$$

In Eq.3.6, local medians f_1 and f_2 replace global mean c_1 and c_2 in Eq.3.5 respectively. Where $f_1 = median(I * inside(C) * W)$, $f_2 = median(I * outside(C) * W)$, W is a rectangle window that is used to define neighbourhood pixels in an image. The robust active contour model using local information in an image instead of the global information improved the quality of the medical image segmentation.

3.3.2 Threshold-based Level Set

My PhD study introduces a new hybrid method called the threshold-based level set (TLS) [78]. This method was designed for the segmentation of intracranial aneurysms, with aim to optimize the accuracy of detecting aneurysm size and shape - whilst remaining automatic in its process. The TLS combines both geodesic active contour, which utilizes local boundary information and the Chan-Vese model, which uses region-specific global information, within the level-set framework to produce accurate segmentations of the morphology of intracranial aneurysms under varying clinical conditions. The associated evolution of PDE in the level-set framework is represented as follows:

$$\frac{\partial \varphi}{\partial t} = |\nabla \varphi| \left(\alpha \left(I - T \right) + \beta div \left(g \frac{\nabla \varphi}{|\nabla \varphi|} \right) \right) \qquad (3.7)$$

where I represents the image to be segmented, T the intensity threshold, g is the image gradient, $\kappa = div(\frac{\nabla\varphi}{|\nabla\varphi|})$ the curvature, α the image propagation constant and β represents the spatial modifier constant for the curvature κ. α and β serve to weight the relative influence of each of these terms on the movement of the surface contour. Details for the TLS method will be further described in Chapter 4.

Chapter 4

Threshold-based Level Set Segmentation Method

Level set methods are popular for solving many types of segmentation problems. The popularity of this is mainly due to the robust deformations and embedding in a well-studied mathematical framework. The previous chapter outlined the history of variational methods, which are mostly implemented using the level set representation. This chapter will continue by describing contributions in this thesis by applying a new level set method for intracranial aneurysm segmentation. Section 4.1 will start with a brief review of several approaches which are currently utilized in cerebrovascular segmentation. Sections 4.2 to Section 4.5 will explain in detail, the method of threshold-based level set segmentation, including the principle, formula, numerical scheme and the parameter setting of the boundary detector function. Section 4.6 will describe clinical studies in which we applied the proposed threshold-based level set method to eight patient-specific aneurysm cases, with comparison of results obtained alongside other segmentation approaches. These results will be a part of the in-vivo validation tests conducted.

4.1 Background

Specification of intracranial aneurysm morphology and hemodynamic analysis requires segmentation of vascular geometries from three-dimensional (3D) medical images, produced via CTA, MRA or DSA. Methods for such manipulations of medical images are directly linked to the accuracy of aneurysm model construction, particularly regarding the geometry of complex shapes and volumes. In most cases, this process involves extraction of the 2D image from CTA, MRA or DSA, followed by reconstruction of the 3D aneurysm surface model. As such, several approaches exist and are currently utilized in cerebrovascular segmentation. On one hand, the fuzzy-based approach has been adapted for the detection of malformed and small vessels in MRA images [79], whilst region growing approaches are popular in medical image segmentation due to their simplicity and computational efficiency [80]. Major problems, however, include leakage when the boundary is blurred, and sensitivity to seed position. Utilization of implicit active contour methods within the level-set framework seem to be widespread in medical image segmentation [81–83] as the method does not suffer from parameterization surface problems [84] and has the capability to handle complex geometries and topological changes [69, 72]. More recently, active contour methods have also appeared in the modeling of intracranial aneurysms and cerebrovascular segmentation [85, 86]. Law et al. proposed a method based upon multi-range filters and local variances to perform segmentation of intracranial aneurysms using Phase Contrast Magnetic Resonance Angiography data [87]. Hernandez and Frangi have developed a segmentation method for intracranial aneurysms based on Geometric Active Regions (GAR), using CTA and 3D Rotational Angiography data [88], whilst several Geodesic Active Contours (GAC) based methods have since been adapted for segmentation of brain aneurysms from CTA data [89,90]. These methods require either sufficient training sets or are reliant upon boundary information obtained from medical imaging. Furthermore, boundary-based active contour level set methods may easily leak

when the target boundary is not clearly defined. Though Firouzian et al. proposed a Geodesic Active Contours -based level set method which employs region information and intensity, a user-defined seed point is required in order to calculate intensity threshold [91].

Despite the many image segmentation methods available, with varying approaches and algorithms, there is no dominant method in terms of effectiveness, across all areas [92–94]. Our previous study indicated that the volume of the aneurysm models depend strongly on the differing segmentation methods. The segmentation method used, likewise influences the local geometric shapes of the aneurysms invovled [95]. Validation will thus become necessary, in order to compare segmentation methods and adjust the parameters of these segmentation techniques to assure the quality of patient-specific cerebral-vascular hemodynamic analysis. Although a number of commercial software packages for segmentation are currently available on the market, there is a conspicuous lack of discussion of methodology and information regarding validation processes.

In this thesis, We propose a new threshold-based level set method for cerebral aneurysms. This method is based on the Geodesic Active Contours model [73] and Chan-Vese model (CV) [75], integrating both region and boundary information to segment cerebral aneurysms through the use of a global threshold and gradient magnitude to form the speed function. The initial threshold is calculated from the Chan-Vese model and is then iteratively updated via the use of local image information to refine the details of edges throughout the process of segmentation. Upon reaching the aneurysm boundary, the change in the threshold value will decrease because of the contrast created between aneurysm and non-aneurysm intensities and the iteration will stop. The algorithm may then be implemented in an automatic or semi-automatic manner depending on the complexity of the aneurysm shape.

4.2 Threshold-Based Level Set (TLS)

The threshold-based level set combines both the geodesic active contour and the Chan-Vese model within the level set framework.

Under the level set scheme, this contour is seen to deform by the function; $\frac{\partial C(t))}{\partial t} = -F\left|\nabla\varphi\right|$, with an embedded surface $C(t)$ represented as the zero level set of φ by $C(t) = \{x, y \in R|\varphi(x, y, t) = 0\}$. F represents a function for speed, which drives the $C(t)$ surface evolution in the normal direction. It is clear that F exerts a direct impact upon the quality of medical image segmentation. The associated evolution of PDE in the level set framework is represented as follows:

$$\frac{\partial\varphi}{\partial t} = \left|\nabla\varphi\right|\left(\alpha\left(I - T\right) + \beta div\left(g\frac{\nabla\varphi}{\left|\nabla\varphi\right|}\right)\right) \tag{4.1}$$

where I represents the image to be segmented, T the intensity threshold, g is the boundary detector function (more details is discussed in section 4.5, $\kappa = div(\frac{\nabla\varphi}{|\nabla\varphi|})$ the curvature, α the image propagation constant and β represents the spatial modifier constant for the curvature κ. α and β serve to weight the relative influence of each of these terms on the movement of the surface contour.

The first term of the RHS of the formula, $\alpha(I - T)$, defines the region where T is an automatically defined parameter indicating the lower boundary of the intensity level for the target object. In this, the target aneurysm is always assumed to possess a relatively higher intensity level than its background. It can thus be seen that this first term forces the contours to enclose regions with intensity levels greater than T. When the contour lies within the aneurysm region, $(I - T) \geq 0$, it expands in the normal direction. When $(I-T) < 0$, the contour lies beyond the aneurysm region, and thus shrinks with a negative speed. This process stops when the contours converge to the aneurysm boundary; the image I reaching a threshold of T. If we isolate this first term on the RHS of the Eq. 4.1, it becomes the selection criteria for the lower threshold in the region growing threshold

method. The second term in the formula would likewise become the geodesic active contour term.

4.3 Numerical Scheme

If φ is a signed distance function (SDF), i.e. $|\nabla\varphi| = 1$, Eq.4.1 can be simplified to

$$\varphi_t = \alpha(I - T) + \beta div(g\nabla\varphi) \tag{4.2}$$

which suggests a stable iterative numerical scheme to approximate the PDE.

Let φ^k and φ^{k+1} denote the embedding function φ in the i^{th} and $(i+1)^{th}$ iterations respectively, the proposed numerical scheme to update from φ^k to φ^{k+1} consists of the following four steps:

- Re-initialise φ^k. Re-initialisation of an embedding function φ is the process to make $|\nabla\varphi| = 1$ while the embedded curve (the zero set) remains unchanged. One of the efficient methods for reinitialisation is the fast marching method [84].

- Update φ^k to obtain $\overline{\varphi^k}$ using $\overline{\varphi^k} = \varphi^k + \triangle_t\alpha(I - T)$ with the predefined time step $\triangle_t$.

- Re-initialise $\overline{\varphi^k}$.

- Update $\overline{\varphi^k}$ to obtain φ^{k+1} via solving the PDE $\varphi_t = \beta div\,(g\nabla\varphi)$ using the additive operator splitting (AOS) approach. AOS is an unconditionally stable finite difference method initially proposed in [96] for nonlinear diffusion filtering and then proposed in [97] for geodesic active contour problem.

4.4 Method for Automatic Threshold Selection

The threshold-based level set requires an appropriate estimate of the threshold value from proper segmentation of the aneurysm, obtained using Chan-Vese model and the statistical data, in particular, confidence interval (CI) and confidence level (CL).

4.4.1 Confidence Interval (CI) and Confidence Level (CL)

The confidence level CL represents how often the true percentage of a population lies within the confidence interval CI. Based on Chebyshevs inequality [98] a general relationship for symmetric distribution between CI and CL can be established. The inequality for symmetric distribution is given as:

$$P\left(|X-\mu| \geqslant k\sigma\right) \leq \frac{1}{k^2} \qquad k>0 \tag{4.3}$$

where X is the random variable population, μ is the population mean and confidence interval is represented by k times σ standard deviation. Eq.4.3 indicates that more than $\left(1-\frac{1}{k^2}\times 100\right)$ percent of the population lies between k standard deviations from the population mean.

For non-symmetric distribution, the one-tailed version of the inequality is used. This is given by:

$$P\left(X-\mu \geqslant k\sigma\right) \leq \frac{1}{1+k^2} \qquad k>0 \tag{4.4}$$

For this inequality, it follows that when $k=1$, more than 50% of the population is located one standard deviation away from the mean.

4.4.2 Initial Threshold Selection

According to the theory of confidence interval, the lower bound threshold of the aneurysm can be defined by:

$$T_i = \mu_a - k_i \sigma_a \qquad i \geq 0 \tag{4.5}$$

The threshold T represents the difference between the mean of the intensity of the aneurysm (μ_a) and k times its standard deviation (σ_a). The intensities of the aneurysm and its background regions are different, with the lowest intensity threshold of the aneurysm the same as the highest intensity threshold of the background. Thus, the relationship $\mu_b + k_b \sigma_b = \mu_a - k_a \sigma_a$ would apply. The confidence levels for both the aneurysm and its background are considered to be the same; $k_b = k_a = k$, thereby allowing k to be expressed as:

$$k = \frac{\mu_a - \mu_b}{\sigma_a + \sigma_b} \tag{4.6}$$

We have utilized the Chan-Vese model method to perform an initial segmentation. From the results obtained, the initial k_0 was seen to be calculated via Eq.4.6. The initial T_0 can likewise be found using Eq.4.5.

4.5 TLS Boundary Detector Function

The TLS method (Eq.4.1) utilizes a boundary detector function g, g can be definded as:

$$g\left(|\nabla I|\right) = \frac{1}{1 + c\left|\nabla I\right|^2} \tag{4.7}$$

where, g is for the detection of vascular boundaries, $|\nabla I|$ represents a gradient magnitude and c is a constant that controls the slope of the boundary detector function, $g\left(|\nabla I|\right)$. At the boundary of the aneurysm and background, the gradient $|\nabla I|$ is seen to increase significantly. At the inside of the aneurysm, the gradient $|\nabla I|$ is small and $g\left(|\nabla I|\right) = 1$.

However, at an ideal edge, $|\nabla I| \to \infty$ and $g(|\nabla I|) \to 0$. In other words, when $g(|\nabla I|) = 0$, this indicates a boundary. As mentioned in the chapter 2, different medical imaging modalities are able to generate different quality of medical imagery. The gradient $|\nabla I|$ of CTA image is relatively lower compared with the DSA image. Thus, a relatively c was needed for the adjustment of the decreasing speed of $g(|\nabla I|)$, in order to ensure that the search for the boundary was stopped at the aneurysm boundary.

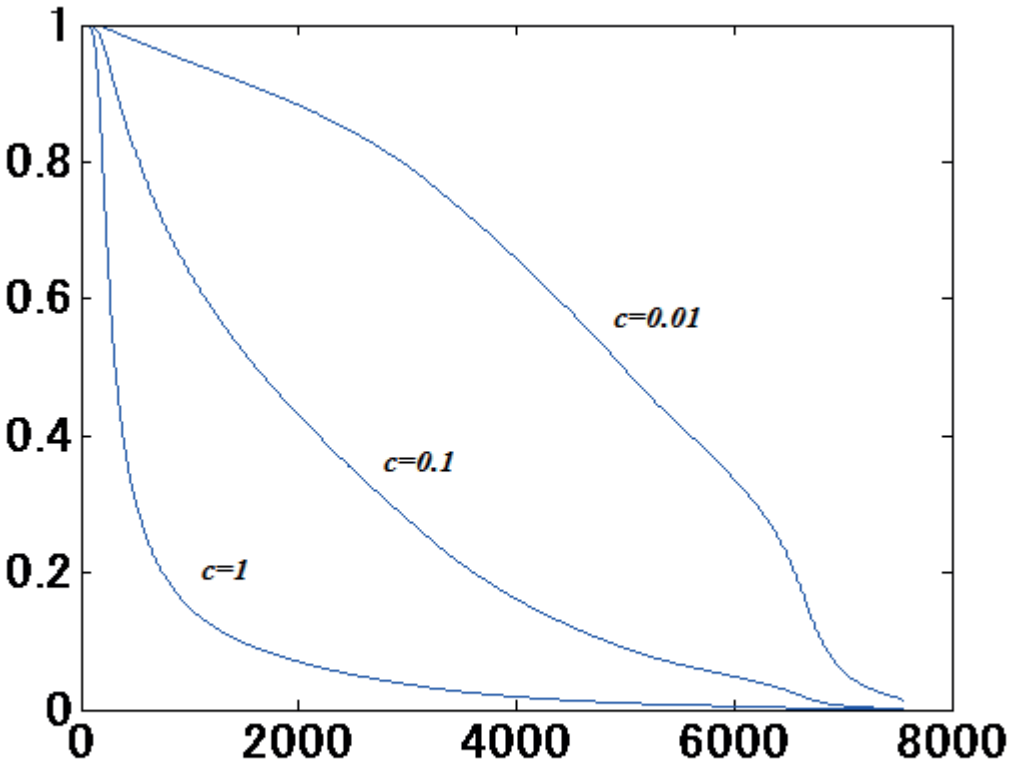

(a) Case 1

Figure 4.1 TLS Boundary detector function $g(|\nabla I|)$ is showed in three cases, g value is showed in the colomn and $|\nabla I|^2$ is listed in the row, (a) the Case 1 is a CTA image, the maximum of $|\nabla I|^2$ at the boundary is 8000. We can see when $c = 1$, even $|\nabla I|^2$ value is 2000 which is far from the boundary, g is already smaller than 0.1. However, if adjust c to 0.1, when $g = 0.1$, $|\nabla I|^2$ is around 5000. We noticed that when $c = 0.01$, g will

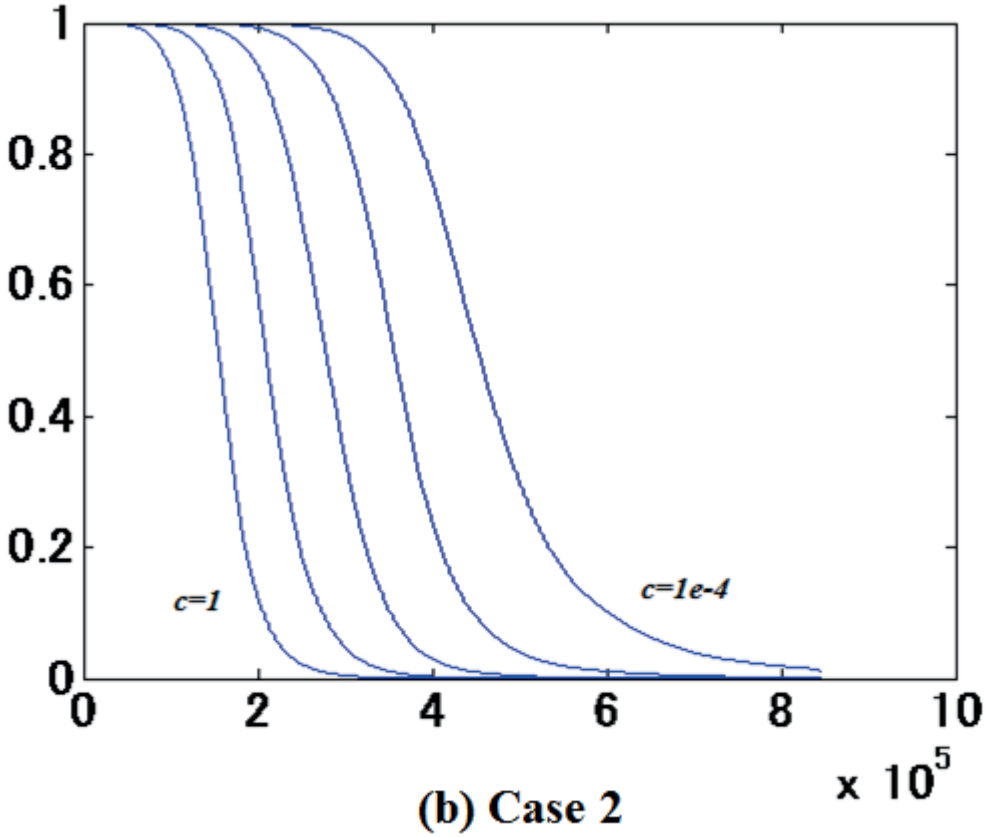

(b) Case 2

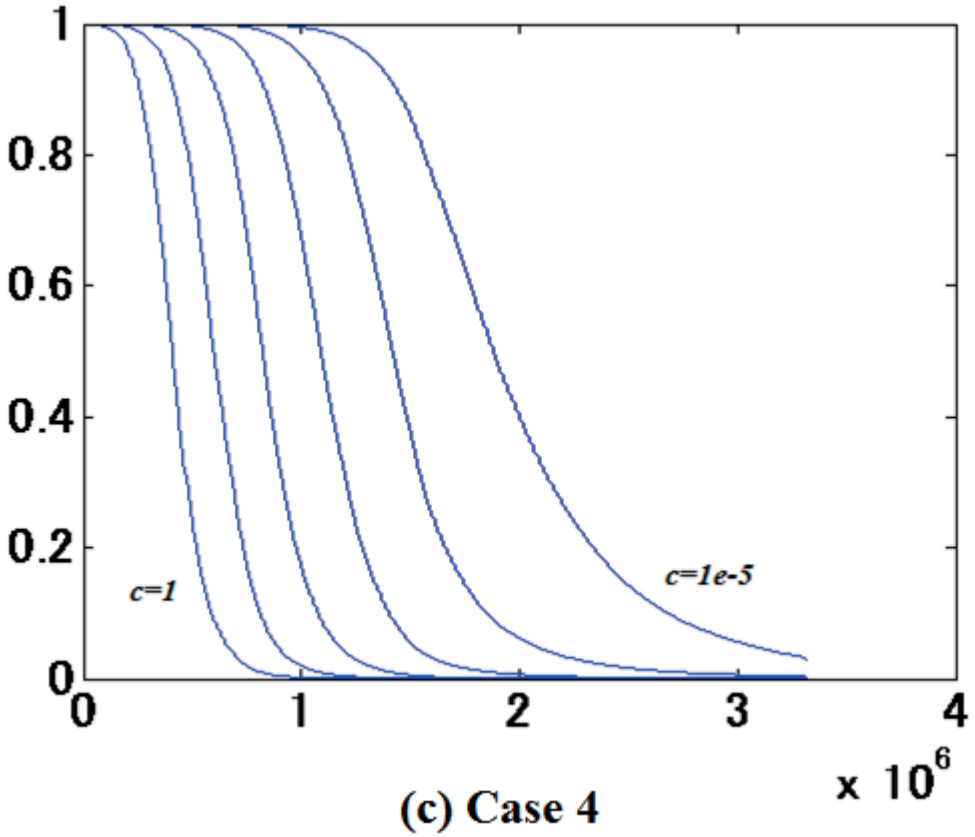

Figure 4.1: TLS Boundary detector function g in three cases with the different value of c. The left side g with $c = 1$, then g curve shifts to the right when $c \times 10^{-1}$.

stop at around 8000, and will cross some boundary, resulting in over segmentation. Thus, choosing $c = 0.1$ for Case 1 seems to be a suitable choice. (b) and (c) are a DSA image, in the Case 2 and Case 4 the maximum $|\nabla I|^2$ is around 8.3×10^5 and 3.3×10^6 respectively. $c = 10^{-3}$ and $c = 10^{-4}$ are more suited for each case respectively.

To overcome the problem, the TLS method uses a criteria to automatically select a suitable value for c for the TLS Boundary detector function $g(|\nabla I|)$. This criteria for value of c is found for which the g curve must meet two conditions: when $g(|\nabla I|) = 0.1$, $|\nabla I|^2 \geq max\left(|\nabla I|^2\right) \times 50\%$, and when $g(|\nabla I|) = 0.01$, $|\nabla I|^2 \leq max\left(|\nabla I|^2\right) \times 80\%$. For example, in Case 1, $max\left(|\nabla I|^2\right) \times 50\% = 4000$, $max\left(|\nabla I|^2\right) \times 80\% = 6400$, from Figure 4.1 (a), we can see that at $4000 \leq |\nabla I|^2 \leq 6400$, a g curve with $c = 0.1$ is able to meet the criteria.

4.6 Experiment

Clinical studies were performed with the consent of the patient in relation to the acquisition of aneurysm images. These images were collected retrospectively from a database. The protocols involved in data collection and analyses were approved of by the local institutional review board and the regional research ethics committee, with eight patient data sets harboring internal carotid artery aneurysms acquired by 3D CTA scans (GE Healthcare) or 3D DSA scans. Cases 1, 2, 6, 7 are CTA images, whilst another four are DSA images. Both 2D CTA and DSA images are depicted in Figure 4.2.

Cross-sectional images were acquired by CT angiography scanner with multidetector-row capability, with a table speed of 9 mm/s and zero-degree table (and gantry tilt). Scanning was initiated from the common carotid artery and continued parallel to the orbito-meatal line to the level of the Circle of Willis, during which intravenous injection of contrast material was administered at a rate of 3.5 mls/s. The aneurysm image was

512×512 pixel field, with slices of continuous thickness used to segment and reconstruct 3D vascular geometry. All pixels are expressed in Hounsfield Units (HU).

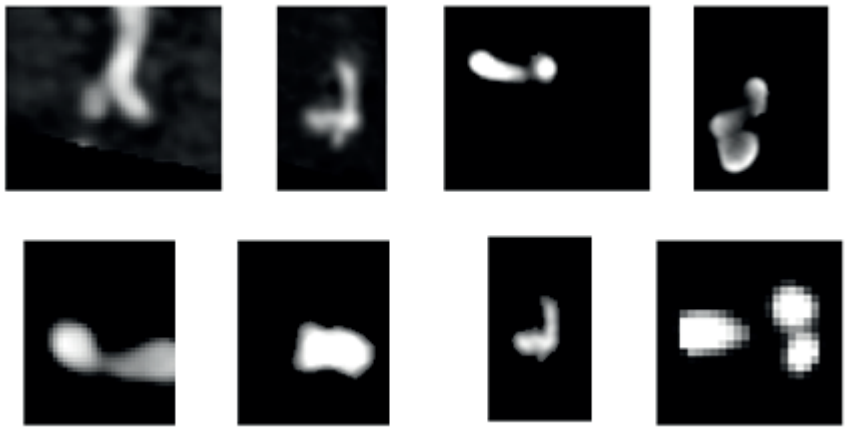

Figure 4.2: 2D CTA or DSA images of the eight cases. Case 1,2,3 and 4 on the top row from left to right and Case 5,6,7 and 8 on the bottom row from left to right.

To evaluate the TLS method, we employed another two segmentation methods, the Region Growing Threshold (RGT), the Chan-Vese model (CV) (the details of which are described in chapter 3), both of which are commonly used in the field of medical imaging. The results obtained from 3D automatic aneurysm segmentations, from the Region Growing Threshold (RGT), the Chan-Vese model (CV), and the Threshold-Based Level Set (TLS), were compared to results obtained via manual segmentation, performed by an expert radiologist over eight data sets of CTA imagery. Evaluation was based upon six validation metrics: volume difference (VD), Jaccards measure (volume overlap metric, JM), false positive ratio (rfp), false negative ratio (rfn), Hausdorff distance (maximum surface distance, HD), and mean absolute surface distance (MASD).

4.6.1 Experiment Setting

For quantitative evaluation, manual segmentation of eight aneurysms using open source software, 3D Slicer, was conducted by an expert radiologist. The results obtained were utilized as a ground truth (GT) for the comparison of other methods. A region of interest (ROI), a good representation of the targeted region for segmentation, was selected depending on aneurysm size. All experiments were performed on cropped data sets to reduce calculation time and memory usage, with preparatory work completed prior to the conduction of the experiments.

4.6.1.1 Parameter Setting

- The threshold-based level set

  The initial zero level set is a rectangular prism surface, constructed by subtraction of two pixels on either side of the ROI. Thus, three parameters needed to be set: α, β from Eq.4.1 and c from Eq.4.7. All eight experiments utilized a fixed setting of $\alpha = 10$, $\beta = 3$. c is selected automatically depending upon the image quality generated by the medical imaging modalities in the range 0.1 to 10^{-4}. The role of this has been detailed in Section 4.5.

- The Chan-Vese model

  Apart from its representation by factional form, CV can also be expressed through the level set form. The associated evolution PDE in the level set framework is represented as:

$$\frac{\partial \varphi}{\partial t} = |\nabla \varphi| \left[\lambda_2 \left(I - \mu_{out} \right)^2 - \lambda_1 \left(I - \mu_{in} \right)^2 - \alpha + \beta div \left(\frac{\nabla \varphi}{|\nabla \varphi|} \right) \right] \tag{4.8}$$

  where μ_{in} is the mean of the target object of intensity, μ_{out} represents the mean of the background of intensity and λ_1, λ_2, α, β are positive constants. The initial zero

level set is a cuboid surface, constructed in the same manner as the TLS, with the parameters in Eq.4.8 fixed for all cases; $\lambda_1 = \lambda_2 = 0.001$, $\alpha = 0$, $\beta = 0.3$.

- The region growing threshold

  Details of the region growing threshold are explained in chapter 3, section 3.1. The RGT selection criterion is described as per the following equation:

$$I(X) \in [X - T_1, X - T_2] \tag{4.9}$$

  According to each case, an initial seed point is required to determine the starting loci within the specific aneurysm. For low and high intensity thresholds T_1 and T_2 in Eq.4.9, T_1 was selected to utilize the threshold of the TLS result for each case, with T_2 representing the highest intensity of the aneurysm.

4.6.2 Evaluation

- Aneurysm volume was calculated through use of the boundary geometry, segmented using various methods. The volume difference (VD) was calculated using the equation, $VD = \left|\frac{(V_s - V_g)}{V_g}\right| \times 100\%$, where V_g represents the volume of GT and V_s represents the volume of the TLS, RGT or CV methods.

- Jaccards measure (JM) is a volume overlap metric, used to count the percentage of voxel intersections for the paired segmentations. This can be seen as $JM = \frac{2 \times |S_g \cap S_s|}{S_g \cup S_s}$, where S_g represents the voxels created by the GT and S_s the voxels generated through use of the TLS, RGT or CV methods.

- False positive ratio (rfp) represents the percentage of the extra voxels of S_s, located outside of S_g. When the rfp equates to zero, no voxels in S_s will be located outside of S_g. Accordingly, $rfp = \frac{|S_s| - |S_g \cap S_s|}{|S_g|}$, where S_g represents the voxels created by the GT and S_s represents the voxels generated by the TLS, RGT or CV methods.

- False negative ratio (rfn) represents the percentage of the lost voxels of S_s, which cover the internal surface of the S_g. This may be seen as $rfn = \frac{|S_g|-|S_g \cap S_s|}{|S_g|}$, where S_g represents the voxels created by the GT and S_s represents the voxels generated by the TLS, RGT or CV methods.

- Hausdorff distance (HD) measures maximum surface distance. This measure is extremely sensitive to outliers and may not reflect the overall degree of correlation.

- The mean absolute surface distance (MASD), indicates the average degree of difference between two surfaces and does not depend on aneurysm size.

4.6.3 Results

The Figure4.3 presents the process of CV segmentation in eight cases via use of 2D contour evolution. In this, we can see that the CV method is able to locate the object (aneurysm) efficiently and quickly. However, this technique is less accurate. This insufficient and over segmented result can be seen in case 2 and case 8 respectively.

The Figure 4.4 illustrates the results of TLS segmentation of eight cases via the use of 2D contour evolution. To compare with the results from the CV method, more contour evaluations were conducted around the boundary of the aneurysms. This clearly indicates that the TLS method is able to work on the detail of the aneurysm boundary. In case 8 (Right bottom of Figure 4.3), the yellow contour represents the output of the CV method, with evidence that the result obtained is over segmented. The red contour represents the TLS result, which uses information from the image edge in order to adjust the contour towards the right position. The results from TLS segmentation of eight cases presenting via 3D model are illustrated in Figure 4.5. All segmentation results across the eight cases, including RGT, CV and TLS are presented in Figure 4.6.

The calculated values of VD, JM, rfp, rfn, HD and MASD for the eight cases considered

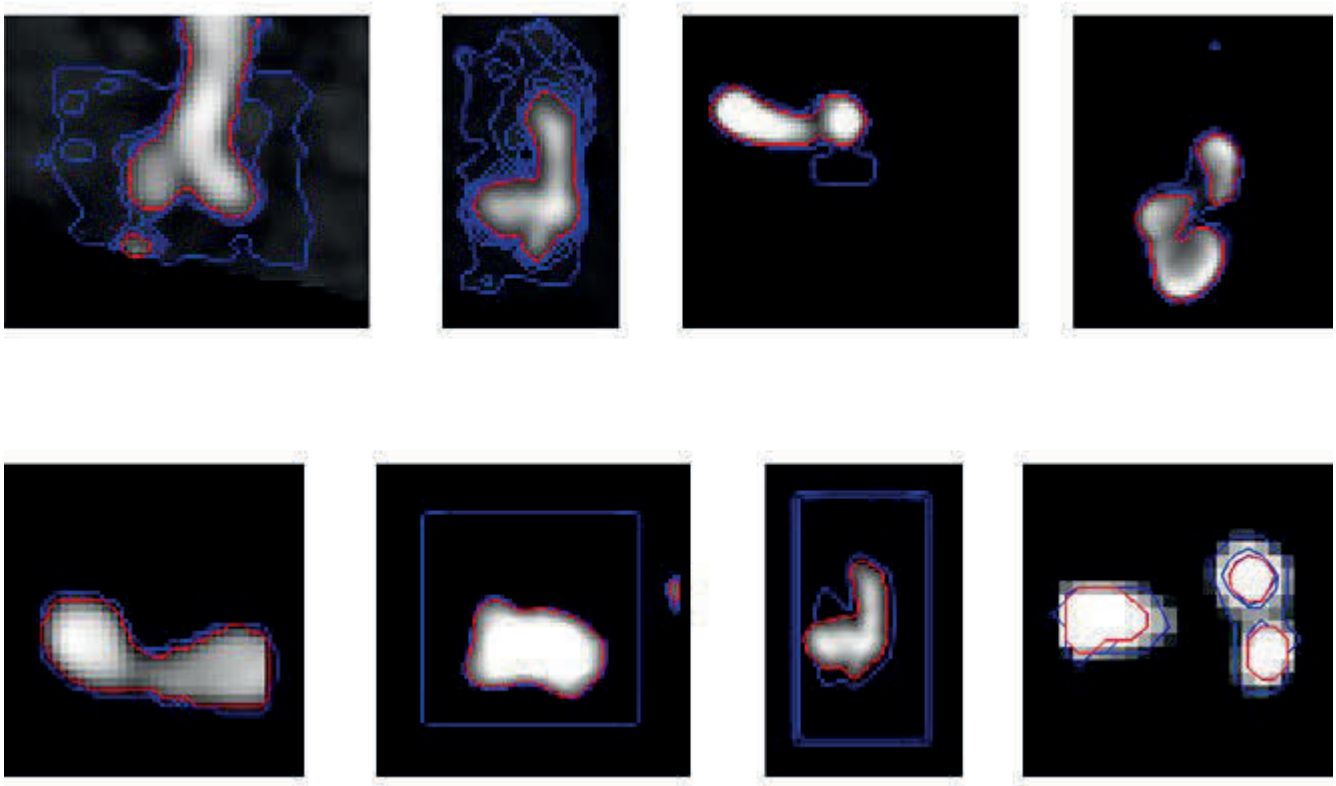

Figure 4.3: CV method contour evolution process of eight cases. The blue lines represent the contour changes during the evolution process and the red line marks the final contour that stops at the apparent boundary of the aneurysms. Top to bottom and left to right, represents Case 1 to Case 8 respectively.

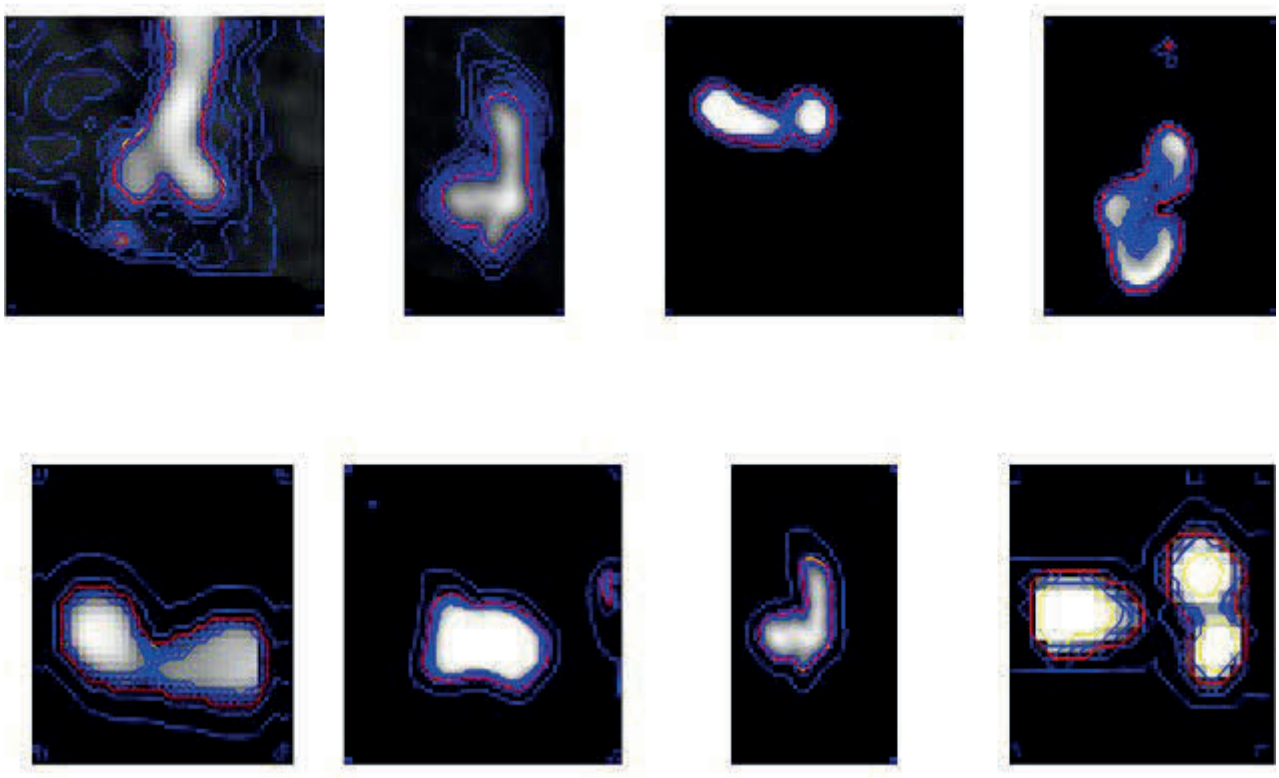

Figure 4.4: TLS method contour evolution process of eight cases. The blue lines represent the contour changes during the evolution process, the yellow lines indicate the primary CV result and the red line marks the final contour that stops at the apparent boundary of the aneurysms.

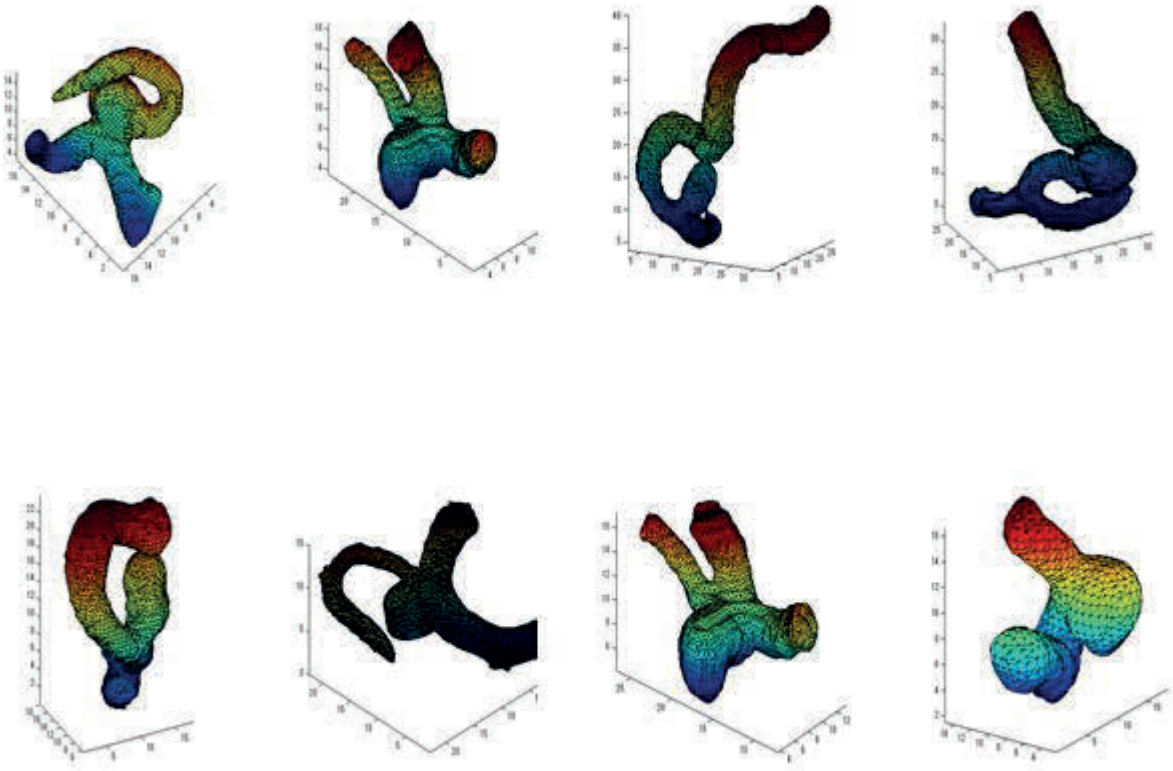

Figure 4.5: TLS segmentation results of eight cases presenting by 3D model.

Colour is proportional to the surface height (Z direction) from blue to red.

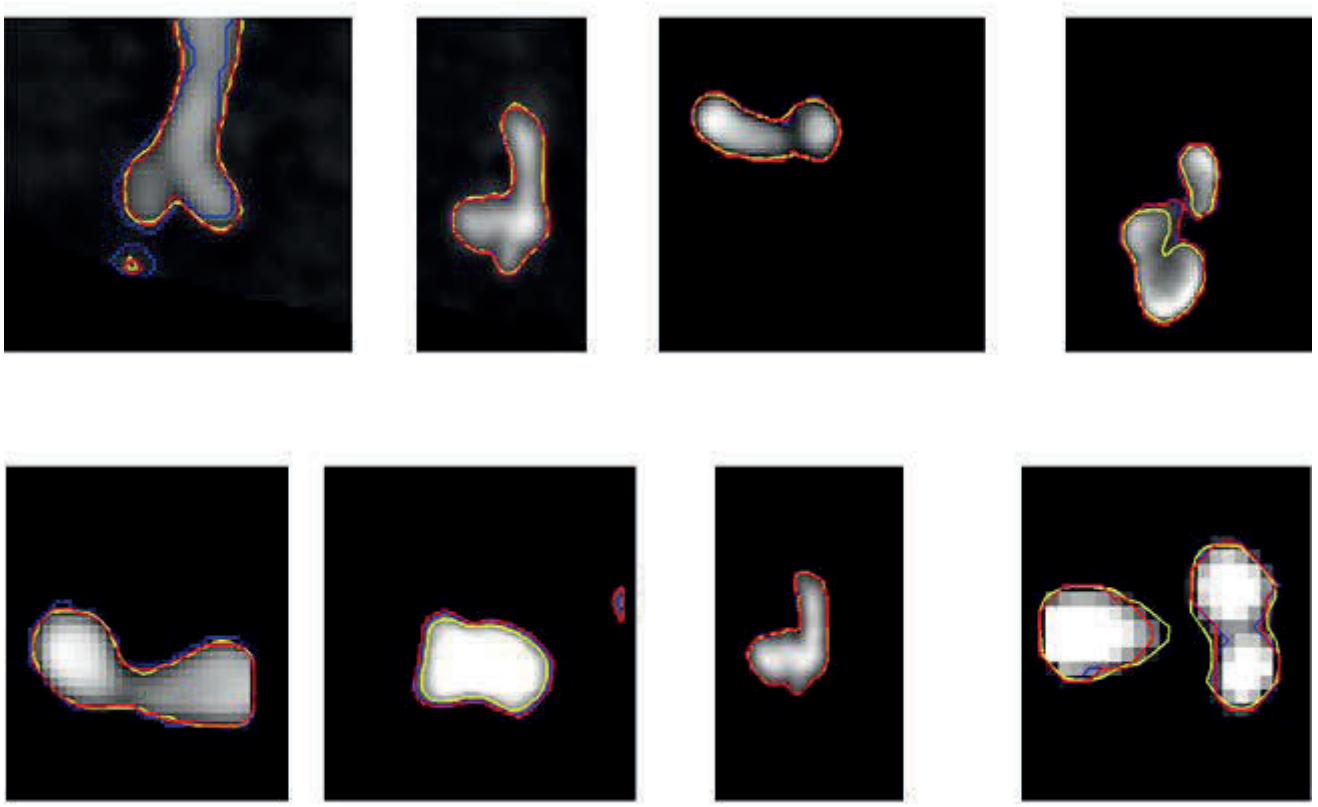

Figure 4.6: The segmentation results of eight cases, represented by 2D contours. The blue contour represents the result of the Region Growing Threshold (RGT), the yellow and red represent the results of the Chan-Vese (CV) and the Threshold-based Level Set (TLS) respectively.

	$Case1$	$Case2$	$Case3$	$Case4$	$Case5$	$Case6$	$Case7$	$Case8$	$Average \pm SD$
$VD(\%)$									
GT	0	0	0	0	0	0	0	0	
TLS	1.55	4.6	4.48	0.46	2.92	0.12	3.5	2.27	2.51±1.72
RGT	7.65	4.47	8.86	1.37	5.52	6.09	3.21	10.90	6.01±3.9
CV	11.63	18.23	5.60	4.04	2.47	2.51	24.18	14.02	10.34±8.06
$JM(\%)$									
GT	100	100	100	100	100	100	100	100	
TLS	91.87	89.66	88.57	93.25	91.64	92.35	91.55	93.79	91.59±1.74
RGT	90.12	88.24	87.02	93	91.39	90.9	94.27	89.58	90.57±2.38
CV	88.24	84.02	86.73	89.53	91.85	91.82	76.96	89.59	87.34±4.93
$rfp(\%)$									
GT	0	0	0	0	0	0	0	0	
TLS	4.97	2.91	3.20	1.65	3.60	3.99	4.06	2.11	3.31±1.08
RGT	0.64	3.80	14.72	0.92	9.22	1.64	5.95	0.13	4.63±5.13
CV	11.84	18.02	13.26	5.38	4.6	5.54	28.75	11.62	12.38±8.09
$rfn(\%)$									
GT	0	0	0	0	0	0	0	0	
TLS	3.57	3.25	1.51	5.21	1.40	3.97	4.73	4.23	3.48±1.40
RGT	9.26	8.40	0.17	6.15	0.18	7.61	0.12	10.30	5.27±4.40
CV	1.32	0.84	1.78	5.66	3.93	3.09	0.92	0	2.19±1.89
$HD(pixel)$									
GT	0	0	0	0	0	0	0	0	
TLS	0.51	0.65	0.68	1.17	0.79	1.89	0.65	0.79	0.89±0.45
RGT	0.77	0.64	0.89	1.41	0.55	1.86	0.49	0.76	0.92±0.47
CV	0.75	1.17	1.04	2.09	1.19	0.51	1.00	0.95	1.09±0.46
$MASD(pixel)$									
GT	0	0	0	0	0	0	0	0	
TLS	0.08	0.08	0.07	0.09	0.07	0.05	0.07	0.10	0.08±0.02
RGT	0.10	0.10	0.12	0.10	0.10	0.07	0.07	0.10	0.10±0.02
CV	0.06	0.06	0.07	0.11	0.08	0.05	0.07	0.10	0.08±0.02

Table 4.1: The results of segmentation size and volume comparison.

are tabulated in Table 4.1. The average values are also shown. Figure 4.7 depicts the volume of the aneurysm. The minimum VD can be seen in the TLS method. The average value of VD is seen to be 2.51%, though the maximum VD is seen for Case 7 using the CV method. The values of JM indicate that the TLS method has the highest overlap rate in comparison to the other two methods, with an average of 91.59%. A study of rfp and rfn indicates a 3.31% overflow and 3.48% absence on average for the TLS method. The largest rfp and the smallest rfn were found to occur via use of the CV method. These results likewise indicate that the largest volume was generated by the CV method, when compared to all other methods.

Results obtained for the surface distance metrics (HD and MASD) indicate the reliability of all segmentation methods, with the HD values for the TLS method between 0.51 to 1.89 pixels and the maximum MASD found to be 0.08.

Figure 4.8 depicts the 3D geometry of Case 4, restructured via three segmentation methods. Only TLS was effective in fully reconstructing the parent artery and aneurysm, while the other two methods were not able to construct a portion of the artery. One reason for this is that the aneurysm size in Case 4 is larger in comparison to other cases and is a DSA image, The obvious changes of the blood speed in the large aneurysm is reflected in the image with the intensity inhomogeneous distribution. Both RGT and CV models are only able to function under homogeneity images [99]. Another point is that the distal parent artery itself is curved to lie proximal to the aneurysm. These results likewise indicate that the TLS method may be utilized in the segmentation of aneurysms with blurred boundaries and inhomogeneous images.

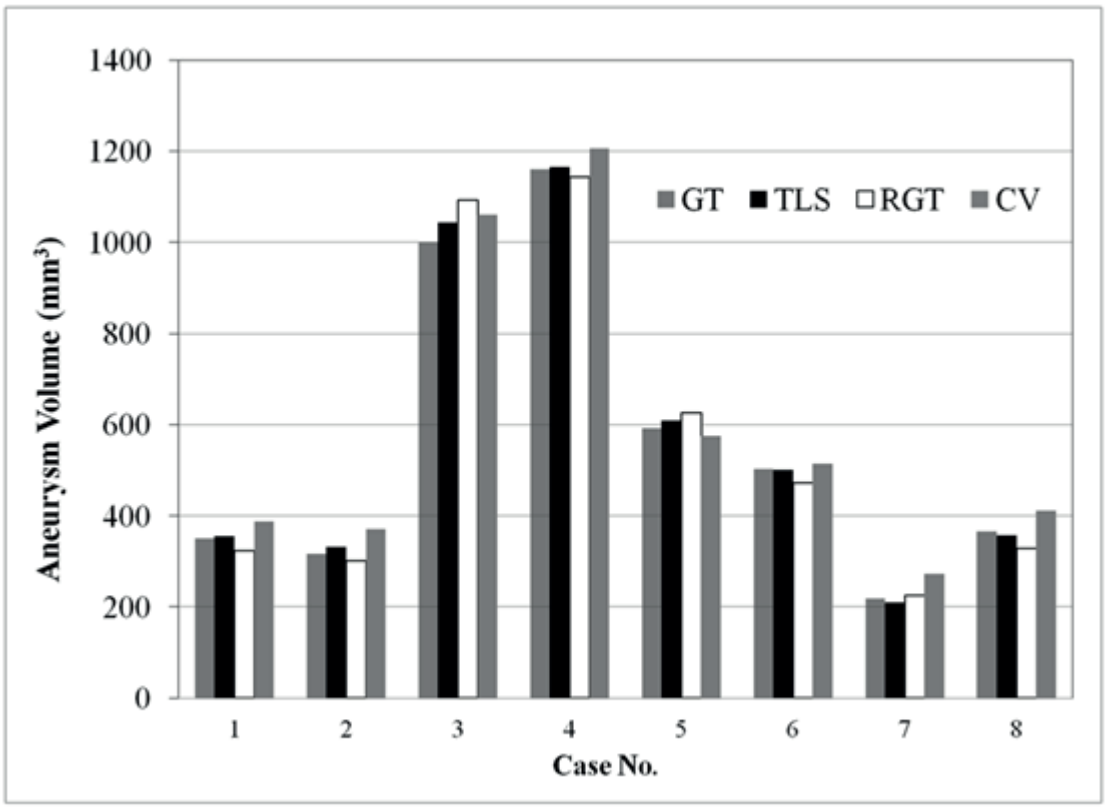

Figure 4.7: Aneurysm volume against segmentation methods.

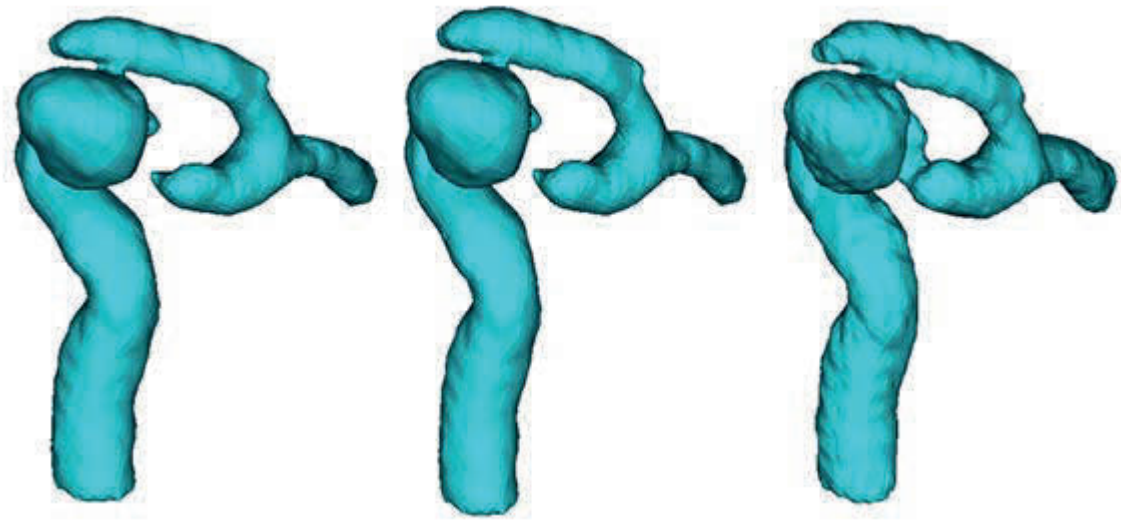

Figure 4.8: 3D geometries of segmentation results comparison, from left to right; CV, RGT, and TLS.

4.7 Conclusion

The TLS method is able to segment intracranial aneurysms with blurred boundaries, complex cerebrovascular anatomical shapes and inhomogeneous images under automatic conditions. By comparison and contrast to other approaches, the TLS method results show that it has the highest volume overlap rate (JM), the lowest volume difference (VD) and greater attention to a local geometry of intracranial aneurysms which is an extremely important improvement in clinical application.

In summary, we found that the volume of the aneurysm models is able to reach a difference of 24% with different segmentation methods. The anatomical shapes of local aneurysms were likewise found to significantly influence segmentation results. The geometry overlapping characters (Jaccards measure), maximum surface distance, and mean absolute surface distance have also exhibited variations across different segmentation methods. This study revealed the existence of inherent limitations in the application

of cerebrovascular segmentation present in current segmentation methods.

Chapter 5

Influence of Medical Image Segmentation Methods on Intracranial Aneurysm Haemodynamic

Patient-specific haemodynamic technology has, in recent years, been increasingly utilised in clinical applications. The results from computational haemodynamic simulation results, i.e. blood pressure, velocity, wall shear stress (WSS), and energy loss (EL) support vascular surgeons in disease diagnoses and surgical preparation. Furthermore, this is an active area of research in recent years, in attempt to explain aneurysm formation, development and rupture. Computational haemodynamic simulation is typically performed via the use of geometric results obtained via medical image segmentation. However, even when employed upon the same set of medical imaging data, the geometry and volume of intracranial aneurysm models are highly dependent upon the varying segmentation methods, described in chapter 4. This chapter will investigate the influence of this technology

upon each haemodynamic characteristics, caused by changes in the geometry, caused by three segmentation methods; the Region Growing Threshold (RGT), Chan-Vese model (CV) and Threshold-Based Level Set (TLS). Section 5.1 will introduce computational fluid dynamics (CFD) technology application in intracranial aneurysms with current circumstances, whilst Section 5.2 will expand upon patient data collection. In total, 45 patients with three different anatomical locations were introduced in this study. The experimental methods and setting of parameters will be listed in Section 5.3, whilst results will be detailed in Section 5.4. In summary, we discovered that the average VD of all three segmentation methods lay in the vicinity of 9.3% (SD=± 4.6%). The computational haemodynamic simulation was performed via the use of three varying categories of segmentation methodology, alongside measurement of typical haemodynamic characteristics; i.e. energy loss (EL) and wall shear stress (WSS). From this, we were able to garner an average of 21.9% (SD=±8.6%, $P < 0.01$) the difference in EL between the varying segmentation methods. On the other hand, the difference in WSS sat at an average of 23.8% (SD=±8.5%, $P < 0.01$) and 126.4% (SD=±124.4%) for the highest and lowest volumes of WSS respectively. These results indicated that the difference in EL and greatest WSS appeared to be both relatively stable and subject to control via the influence of segmentation method. However, the results of the lowest WSS, were seen to be significantly dependent upon the surface geometry of the aneurysm surface. It is thereby essential, in order to confirm the quality of segmentation processes in the application of patient-specific analyses of cerebrovascular haemodynamics - to validate these individual segmentation methods as separate technologies.

5.1 Background

Rupture of intracranial aneurysm (IA) is a much studied topic, with reports indicating the presence of un-ruptured IAs in approximately 5% of the adult population [100, 101]. Though the rupture rate of IAs is not high [102] it may lead to serious consequences including disability and mortality [103]. On the other hand, current treatments of IAs also carry significant risks. To counter this, accurate assessment of IA is thereby essential in order for clinicians to balance the risk of surgery against the risk of natural IA rupture [104, 105].

Computed Tomography Angiography (CTA) is widely applied in neurovascular imaging as a non-invasive diagnostic tool for the detection and evaluation of intracranial aneurysms. This makes it possible to visualize three dimensional (3D) cerebral aneurysms, allowing us to reconstruct patient-specific vessels. Currently, the 3D geometry blood vessel has been applied in the performance of haemodynamic simulations, with the results subsequently applied as an intelligent tool for the diagnosis and support of aneurysmal treatment. Computational fluid dynamics (CFD) technology has since been applied to calculate blood pressure, velocity, wall shear stress (WSS), and energy loss (EL) [106] - parameters that are difficult to obtain via direct measurement. These haemodynamic parameters have provided useful information in support of vascular surgeons in disease diagnoses and surgical preparation. Moreover, reconstruction of vascular structure from patient specific 3D angiography was used extensively to explain aneurysm formation, development and rupture [107–109]. As such, various types of aneurysm morphology simulation have become the mainstay method for assessing the role of morphology in predicting the risk of rupture [21, 110]. Indeed, by improving the generation of idealized bifurcation models [111], classifying the saccular intracranial aneurysm [112] and conducting in-vitro analysis of bifurcation aneurysms, this method has become even more effective [113, 114]. Despite this, however, a study placing focus on the effect of hemodynamic parameters

including wall shear stress (WSS) in 20 middle cerebral artery (MCA) aneurysms, has shed light on evidence that proved the pathogenic effect of high WSS in the initiation of aneurysms and low WSS in both the growth and rupture of cerebral aneurysms [115]. Cebral et al. [116] performed CFD for a total of 62 cerebral aneurysms at various locations, with findings that indicated the presence of high-speed narrow jet flows in ruptured cases, resulting in high flow at the inlet regions of the aneurysm. Under normal conditions, spatial average was found to be higher within ruptured aneurysms than those within the parent artery. However, a marked reduction was also seen at the top or within the bleb area of the ruptured aneurysm. It is thus unclear whether high or low flow induce aneurysm rupture. Some purport that high flows may induce aneurysm rupture 11 while others claim that low flow at the aneurysm dome poses significant dangers to aneurysm integrity [117].

Further studies concentrating on the energy loss (EL) of 4 ruptured and 26 unruptured internal carotid artery aneurysms found that the EL of ruptured cases was 5 times greater than those of the unruptured cases [106]. Furthermore, a study of 210 cerebral aneurysms revealed the presence of higher kinetic energy ratio in ruptured aneurysms, when compared with their unruptured counterparts [118]. Likewise, a study of 26 aneurysms indicated a reasonable association between larger regions of low WSS and the appearance of ruptured aneurysms [119].

The accuracy of CFD simulation is highly dependent upon vessel geometry [120], with methods of medical image segmentation directly influencing the accuracy of aneurysm model construction, particularly regarding the shapes and volumes of the vessel. Despite the many methods, each with varying approaches and algorithms, there are currently no dominant segmentation methods, in terms of effectiveness, across all areas [92–94]. Our previous study has indicated that the volume of the aneurysm models exhibit variances across different segmentation methods, with the technique likewise influencing the local

geometric shapes of the aneurysms modelled [95]. The validation and verification of such methods will thus be an essential process, comparing segmentation methods and adjusting the parameters of these segmentation techniques in order to confirm the quality of patient-specific cerebral-vascular haemodynamic analysis. Moreover, though a number of commercial segmentation software packages have since been released to the market, there is a current lack of methodological discussion and information regarding validation processes.

In this thesis, 45 aneurysm patients, including vascular and cerebral aneurysm CTA imagery across three locations; the internal carotid artery (ICA), middle cerebral artery (MCA) and anterior communicating artery (AComA), are used for analysis. Three segmentation methods; the Region Growing Threshold (RGT), Chan-Vese model (CV) [75], and the Threshold-Based Level Set (TLS) [78] proposed by our group are applied to segment data from these images. Subsequent comparisons of differences were then drawn, utilising calculations made via the above three segmentation methods, and CFD simulations were performed in order to compare their respective influences upon haemodynamics research.

5.2 Patient Data

Fourty-five patients with middle size aneurysms were selected from the patient database; 15 ICA, 15 MCA, and 15 AComA aneurysm patients. Three-dimensional Computer Tomograph Angiograph (3D-CTA) (GE and Siemens) were performed upon all patients, with cross-sectional images acquired via a CT angiography scanner under the same protocols, a table speed of 9 mm/s and zero-degree table. Scanning was initiated from the common carotid artery and continued parallel to the orbito-meatal line to the level of the Circle of Willis, during which intravenous injection of contrast material was administered

at a rate of 3.5 mls/s. Aneurysm image was 512×512 pixel field, whilst slices of continuous thickness were used to segment and reconstruct 3D vascular geometry. Pixels were expressed in Hounsfield Units (HU), with the CTA imaging carried out from the period spanning 2008 to 2012. The age of patients ranged between $62 - 71$ years, with aneurysm size between $4 - 9$ mm in this study. Patients selected in this study were all female.

Clinical studies were performed with the consent of the patient in relation to acquisition of aneurysm images. These protocols were approved of by the local institutional review board and the regional research ethics committees.

5.3 Experiment

For quantitative evaluation, manual segmentation of 45 aneurysms using open source software, 3D Slicer (http://www.slicer.org), was conducted by an expert radiologist. The results were utilized as a ground truth (GT) for the comparison of other methods. A region of interest (ROI), a good representation of the targeted region for segmentation, was selected depending on the aneurysm size. All experiments were performed on cropped data sets to reduce calculation time and memory usage, with preparatory work completed prior to the conduction of the experiments.

5.3.1 Segmentation Methods and Parameter Setting

Three different segmentation methods, the region growing threshold (RGT), the Chan-Vese model (CV) and we proposed the threshold-based level set (TLS) are employed to produce three geometry 3D models for one patient case. These geometric models are used in the later CFD calculation to compare the difference of the features caused by the segmentation methods. Details of the RGT, CV and TLS are described in chapter 3 and 4. The parameter setting used in the experiment for each segmentation method

is given as follows: For the RGT, the low intensity threshold T_1 is selected to utilize the threshold of the TLS result for each case, with the high intensity T_2 representing the highest intensity of the aneurysm in the medical image. For the TLS, the initial zero level set is a rectangular prism surface, constructed by subtraction of two pixels on either side of the ROI. All forty five experiments utilized a fixed setting of $\alpha = 10$, $\beta = 3$. c is selected automatically depending on the image quality generated by the medical imaging modalities in the range 0.1 to 10^{-4}. For the CV, The initial zero level set is a cuboid surface, constructed in the same manner as the TLS, with the parameters fixed for all cases; $\lambda_1 = \lambda_2 = 0.001$, $\alpha = 0$, $\beta = 0.3$.

5.3.2 Haemodynamic Simulation Methods

5.3.2.1 Simulation Process

FD simulation includes three stages: 1) the segmentation of an aneurysm from medical imaging data recorded in DICOM format and generation of a Standard Tessellation Language (STL) format geometry data; 2) mesh generation and 3) CFD analysis (Figure 5.1). In the first stage, the segmentation methods mentioned above were introduced to reconstruct vessel and aneurysm geometry. In the second stage, ANSYS ICEM was employed in the formation of a mesh for CFD simulation. For the third stage, the geometric models were transferred to a haemodynamic system for CFD analysis.

5.3.2.2 Mesh Generation

As the accuracy of CFD results depend highly upon grid resolution and boundary conditions, a series of verification and validation analyses of mesh independent tests have been carried out at the initiation of this study. When the mesh number was found to have reached approximately 400,000 the haemodynamic character; energy loss (EL),

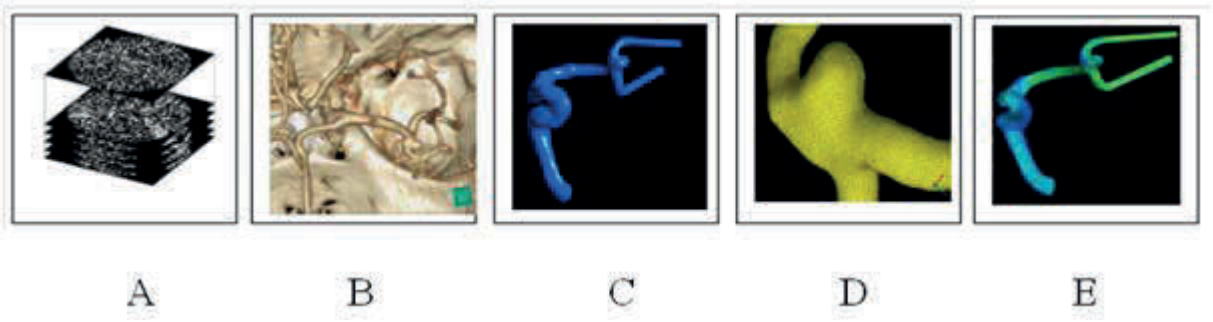

Figure 5.1: Components of the computational analysis system: A: DICOM image obtained from CT or MRI scans. B: 3D angiographic image. C: Numerical model (STL format). D: Mesh generation for finite element model. E: Haemodynamic results.

began to converge into a constant. Thus, accurately reliable results could be obtained with the total of 563,000 finite elements and 240,000 nodes used in this study. In order to accurately calculate the WSS, five layers of prism mesh were inserted onto the arterys internal surface. The distance of the first prism mesh to the artery surface was set to 0.01 mm.

5.3.2.3 Fluid Dynamic Calculation

Flow simulation is based on the Navier-Stokes (N-S) momentum equation and continuity equation defined as below:

$$\begin{cases} \frac{\partial}{\partial t}\left(\rho u_i\right) + \frac{\partial}{\partial x_j}\left(\rho u_i u_j\right) = \frac{\partial p}{\partial x_i} + \frac{\partial}{\partial x_j}\left[\mu\left(\frac{\partial u_i}{\partial x_j} + \frac{\partial u_j}{\partial x_i}\right)\right] \\ \frac{\partial \rho}{\partial t} + \frac{\partial}{\partial x_j}\left(\rho u_j\right) = 0 \end{cases} \tag{5.1}$$

Where i, j =1, 2, 3, x_1, x_2, x_3 represents coordinate axes, u_i, u_j and p are the velocity vectors and the pressure in the point of the fluid domain, ρ and μ are blood density and viscosity, t is time.

5.3.2.4 Blood Flow Modeling and Boundary Conditions

In this study, calculations were performed with steady flow rate 250 ml/min, 150 ml/min, and 100 ml/min at the parent artery inlet for idealized models using average flow rate in the ICA, MCA, and Acom respectively [121]. CFD calculations were performed via the use of CFX 14.1 solver package (ANSYS). In this study, an incompressible, steady-state laminar flow model was considered for the simulation. In large arteries (diameter > 0.5 mm) the Non-Newtonian behaviour of the blood flow is negligible, so blood was assumed to be a Newtonian fluid with blood flow density and dynamic viscosity of 1050 kg/m^3 and 0.0035 Pa.s respectively [115]. By adopting the conventional assumption of a lack of resistance in the cerebral circulation, outlet boundary conditions were set to zero pressure [122]. Along the artery and aneurysm wall, a no-slip flow boundary condition was imposed at the vessel's inner lumen and arteries were assumed to be rigid.

5.3.2.5 Haemodynamic Result Analysis; Energy Loss

Energy loss is calculated as the power difference from inlet to outlet, and can be calculated as follows:

$$EL = \sum \left(P_i + \rho \frac{1}{2} v_i^2 \right) - \sum \left(P_o + \rho \frac{1}{2} v_o^2 \right) \tag{5.2}$$

where ρ is density, v is velocity, i indicates inlet, and o means outlet. In order to calcualte the difference from each segmentation method, the energy loss difference is calculated via the following equation;

$$\triangle EL\,(\%) = \frac{|EL_{GT} - EL_i|}{EL_i} \times 100 \tag{5.3}$$

where, GT is Ground truth method, i is segmentation method RGT, CV, and TLS.

5.3.2.6 Haemodynamic Result Analysis; Wall Shear Stress (WSS)

The wall shear stress (WSS) is derived from predicted flow velocities. The parameter is known to be associated with initial thickening and thrombosis formation, with the WSS defined as:

$$WSS = -\mu \frac{\partial v_t}{\partial n} \mid_{wall} \tag{5.4}$$

where μ is the dynamic viscosity, v represents the velocity parallel to the wall and is the unit vector perpendicular to the wall. Like EL, the WSS is also calculated via the difference between each segmentation method;

$$\triangle WSS\,(\%) = \frac{|WSS_{GT} - WSS_i|}{WSS_i} \times 100 \tag{5.5}$$

where, GT is Ground truth method, i indicates segmentation method RGT, CV, and TLS.

5.3.3 Segmentation Results Evaluation

Aneurysm volume size was calculated through use of the boundary geometry, segmented by various segmentation methods. The volume difference (VD) was calculated via utilisation of the equation, $VD = \left|\frac{(V_s - V_g)}{V_g}\right| \times 100\%$, where V_g represents the volume of GT and V_s represents the volume of the TLS, RGT or CV methods. Jaccards measure (JM) is a volume overlap metric, utilised to count the percentage of voxel intersections for the paired segmentations. $JM = \frac{2 \times |S_g \cap S_s|}{S_g \cup S_s}$, where S_g represents the voxels created by the GT and S_s the voxels generated through use of the TLS, RGT or CV methods. Hausdorff distance (HD) measures the maximum surface distance. This measure is extremely sensitive to outliers and may not reflect the overall degree of correlation.

5.4 Results

Table 5.1 listed the details of all the segmentation and haemodynamics simulation results classified by the intracranial aneurysm locations and segmentation methods.

	ICA	MCA	$AcomA$
$VD(\%)\pm SD$			
TLS	6.2±2.9	8.5±4.7	6.4±4.8
RGT	6.4±3.5	8.8±3.5	9.1±3.6
CV	13.5±4.1	10.3±7.6	14.3±6.2
$JM(\%)\pm SD$			
TLS	93.0±1.2	92.0±1.5	92.3±1.5
RGT	92.5±1.8	90.2±2.1	92.1±1.6
CV	90.2±1.9	89.5±1.9	88.0±2.9
$HD(pixel)$			
TLS	0.74	0.70	0.72
RGT	0.77	0.75	1.06
CV	1.04	1.61	1.04
$EL(\%)\pm SD$			
TLS	14.8±5.5	17.9±8.4	29.2±5.8
RGT	21.2±7.2	28.8±8.1	26.6±10.8
CV	23.1±8.0	22.5±11.4	25.0±13.0
$WSS(high,\%)\pm SD$			
TLS	15.3±4.8	20.3±8.6	19.0±5.8
RGT	22.0±7.3	26.2±13.6	31.4±13.6
CV	23.7±4.8	21.7±8.5	36.3±9.5
$WSS(low,\%)\pm SD$			
TLS	103.5±98.2	269.4±391.2	60.0±18.7
RGT	96.1±112.8	268.7±205.0	82.4±67.6
CV	99.8±95.7	52.4±16.1	104.9±114.5

Table 5.1: The segmentation and haemodynamics simulation results.

5.4.1 Geometric Shapes Observation

Figure 5.2 (e) represents a picture that was taken during treatment of an IA. Two protrusions; A and B, can be clearly observed in the IA, with protrusion A located upon the larger protrusion B. Figure 5.2 (c) and (d) indicate that the results of RGT and TLS methods segment both A and B protrusions. On the other hand, analysis of Figure 5.2 (b)

reveals that the CV method leads to the display of protrusion B only, whilst protrusion A is not replicated in the segmented result.

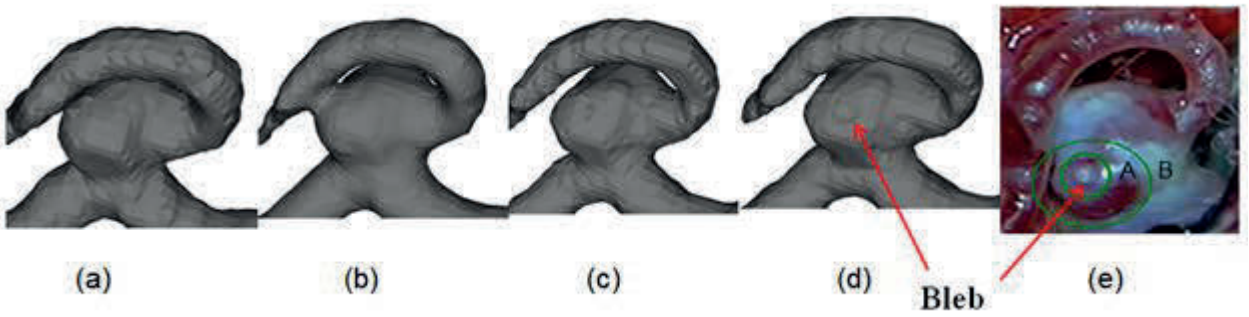

Figure 5.2: Segmentation results comparison (aneurysm with bleb), from left to right: (a) GT, (b) CV, (c) RGT, (d) TLS, and (e) photo from open head surgery. The aneurysm bleb was only able to be observed by the TLS method (d).

5.4.2 Aneurysm Segmentation Results

All model volume differences are listed in Figure 5.3. The largest difference in terms of aneurysm volume, compared with the manual GT method, is around 15%, 17% and 18% within the ICA, MCA, and AComA aneurysms respectively. The maximum VD usually occured in cases whereby the aneurysm connected with multiple arteries. The results of VD from TLS method appeared smaller than that of the other segmentation methods. The average VD of TLS segmentation methods were 5.5% (SD=±2.9%), 8.7% (SD=±4.7%), 9.1% (SD=±4.8%) for ICA, MCA, and AComA aneurysms respectively. The study indicated that the volume differences seen in aneurysm size may be controlled at a maximum under 15% (SD=±6.2%), through the use of various segmentation methods. The geometry volume overlap ratio was calculated via the use of JM, with the results depicted in Figure 5.4. The average overlap ratio are; 91.9%, 91.5%, and 90.6% for ICA, MCA, and AComA aneurysms respectively. The TLS method appears higher in terms of

overlap ratio than the other methods. HD measurements indicate the maximum surface distance to outliers. The maximum HD usually occurs at the top of the intracranial aneurysm; e.g. bleb location. Figure 5.5 depicts the results of HD within three types of aneurysm. The HD results obtained via the TLS method was shown to be lower than 0.8 pixels, coinciding with the results obtained via the manual GT method. The greatest HD was seen to occur in the MCA intracranial aneurysm, a result hypothesized to be due to intracranial aneurysm surface roughness; i.e. from blebs, and the entailing increase in segmentation complexity.

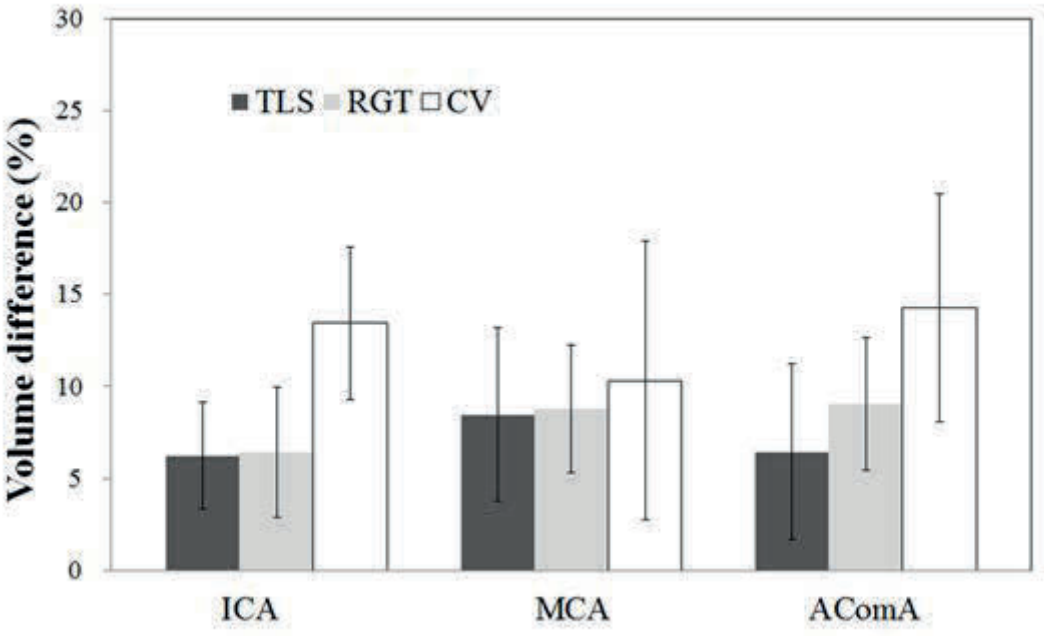

Figure 5.3: Volume difference against segmentation methods.

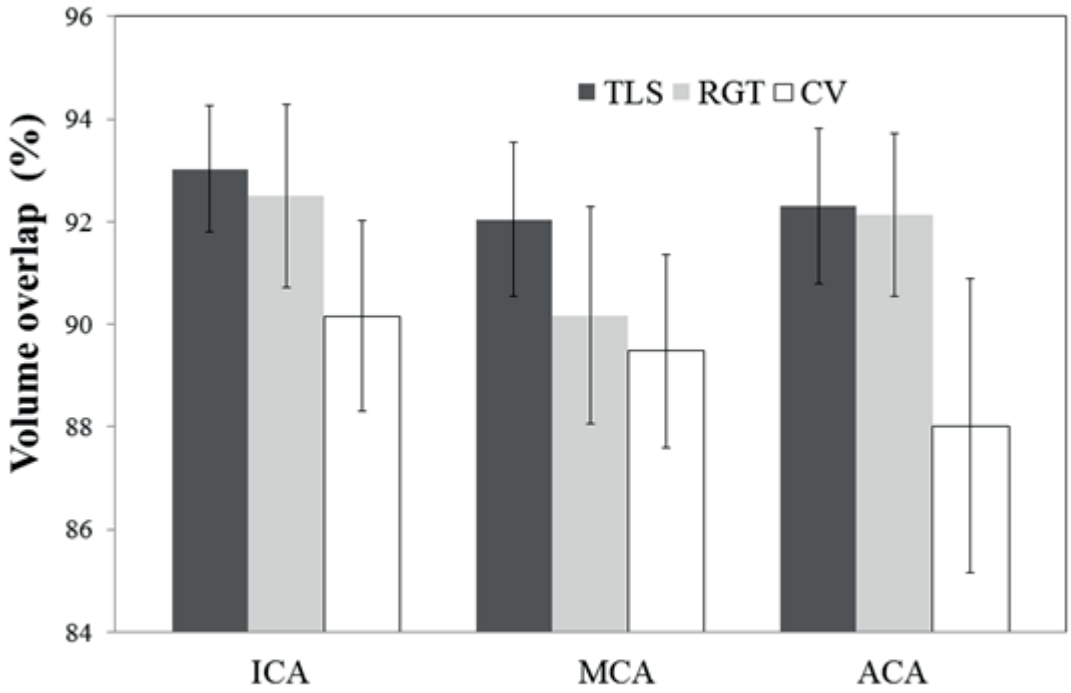

Figure 5.4: Comparison of aneurysm and vessel volume overlap results.

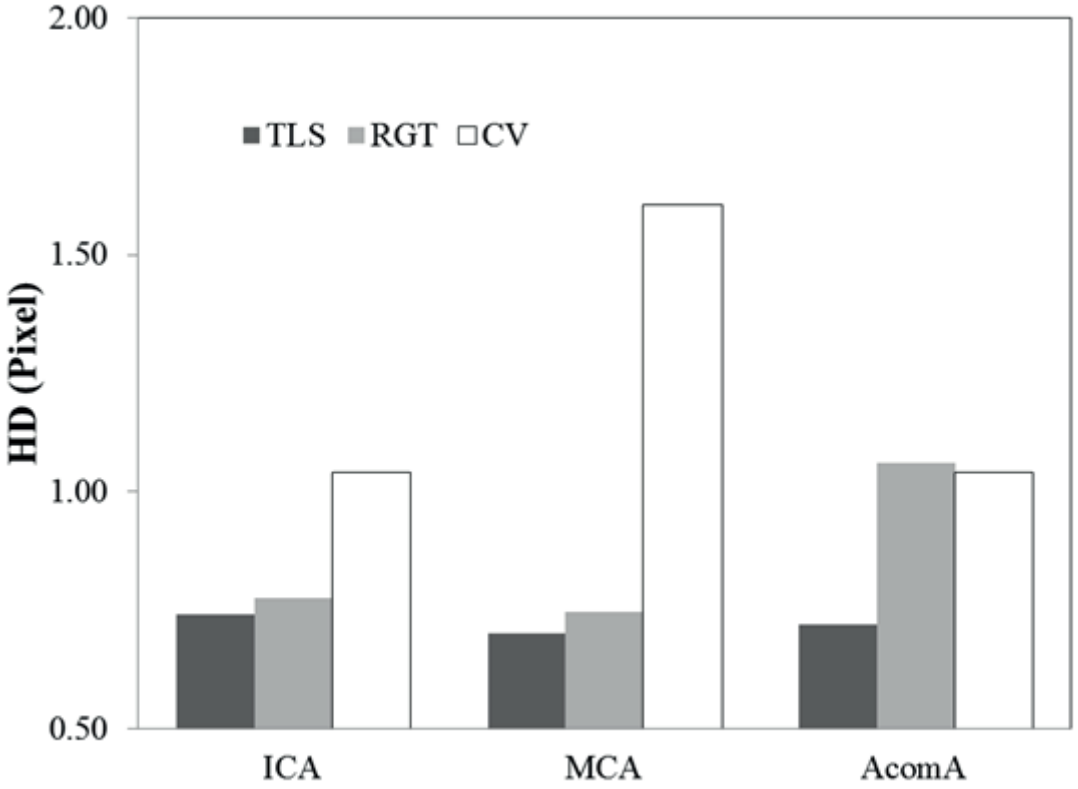

Figure 5.5: Comparison of aneurysm HD results.

5.4.3 Haemodynamic Simulation Results

CFD simulation is performed via a process that includes segmented geometries. In order to compare various models under the same flow conditions; inflow was assumed at 150 ml/min. The outflow condition is extended to a length distant enough to allow pressure recovery at the outlets. Figure 5.6 depicts the results of EL differences, with the average EL differences calculated from TLS, RGS, and CV segmentation methods shown to be 18.2% (SD=±6.8%), 24.4% (SD=±9.3%), and 23.2% (SD=±9.8%) respectively (P<0.01). Figure 5.7, on the other hand, illustrates pressure distribution upon the aneurysm sur-

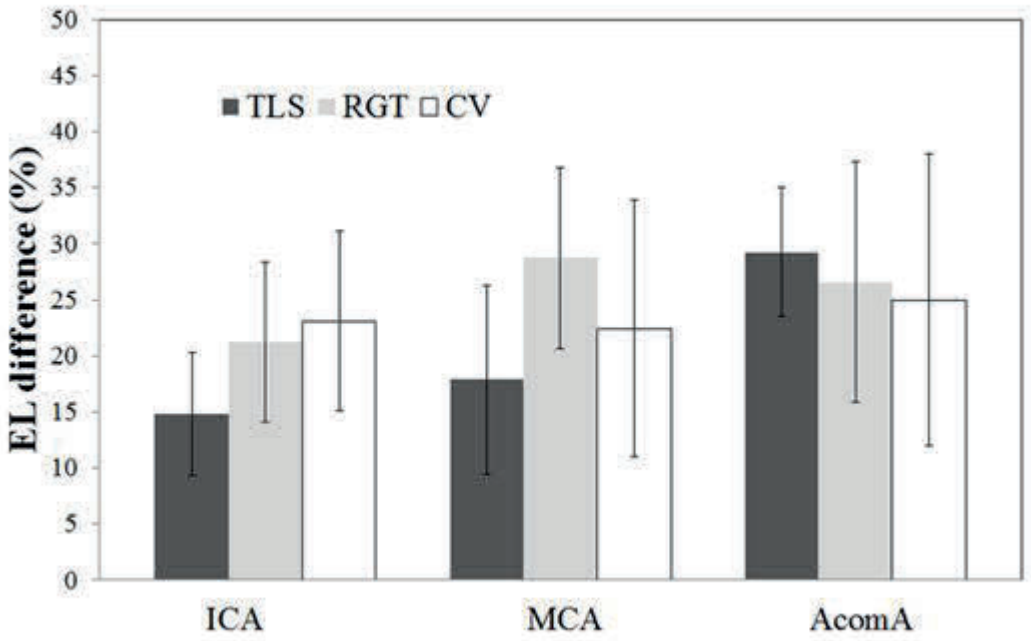

Figure 5.6: Haemodynamic results; EL.

face, with the distributions exhibiting variations across the various segmentation methods. Figure 5.8 depicts the average results of the highest WSS, calculated via the use of the three methods of segmentation. The average of the highest WSS difference, calculated

from TLS, RGS, and CV segmentation methods were found to be 16.8% (SD=±6.8%), 26.4% (SD=±8.3%), and 28.3% (SD=±7.8%) respectively (P<0.01). In this study, the highest WSS was observed at the inlet of aneurysm neck, seen in Figure 5.9. We found significant discrepancies for the lowest WSS, measured via each method. The average differences from the 45 intracranial aneurysms were found to be 144.3% (SD=±169.4%), 149.1% (SD=±129.4%), and 85.7% (SD=±75.4%) for TLS, RGT, and CV respectively (P> 0.1). The lowest WSS was found at the top of the aneurysm, a location with a high risk of rupture, with most IA ruptures occurring commonly at the top of the IA, rather than at its neck [123]. In particular, for ICA, MCA and AComA IAs respectively, there was a 99.8% (SD=±102.2%), 196.8% (SD=±204.1%), and 82.4% (SD=±66.9%) difference when compared to the results obtained via manual GT segmentation method. This shows that the haemodynamic results are dependent upon the accuracy of segmentation methods. Figure 5.8 illustrates the distribution of WSS via the use of different segmentation methods, with the maximum difference of the lowest WSS found to be 1033% in the AComA IA segmented via use of the RGT method. These results indicate that local differences arose for WSS, particularly in the region of the bulb.

5.5 Discussion

The three segmentation methods introduced in this study are popular technologies, commonly utilised in medical image reconstruction. Though vessel boundary is rather easily extrapolated via the RGT method, its issues lie with the sensitivity of threshold selection and seed position [124]. Based on level set technology, the CV method is capable of defining vessel boundaries despite lack of clarity, and is thereby able to model images with approximate boundaries [75]. This level of accuracy, however, is not sufficient for the conductance of haemodynamics studies. To counter this, the TLS method was proposed

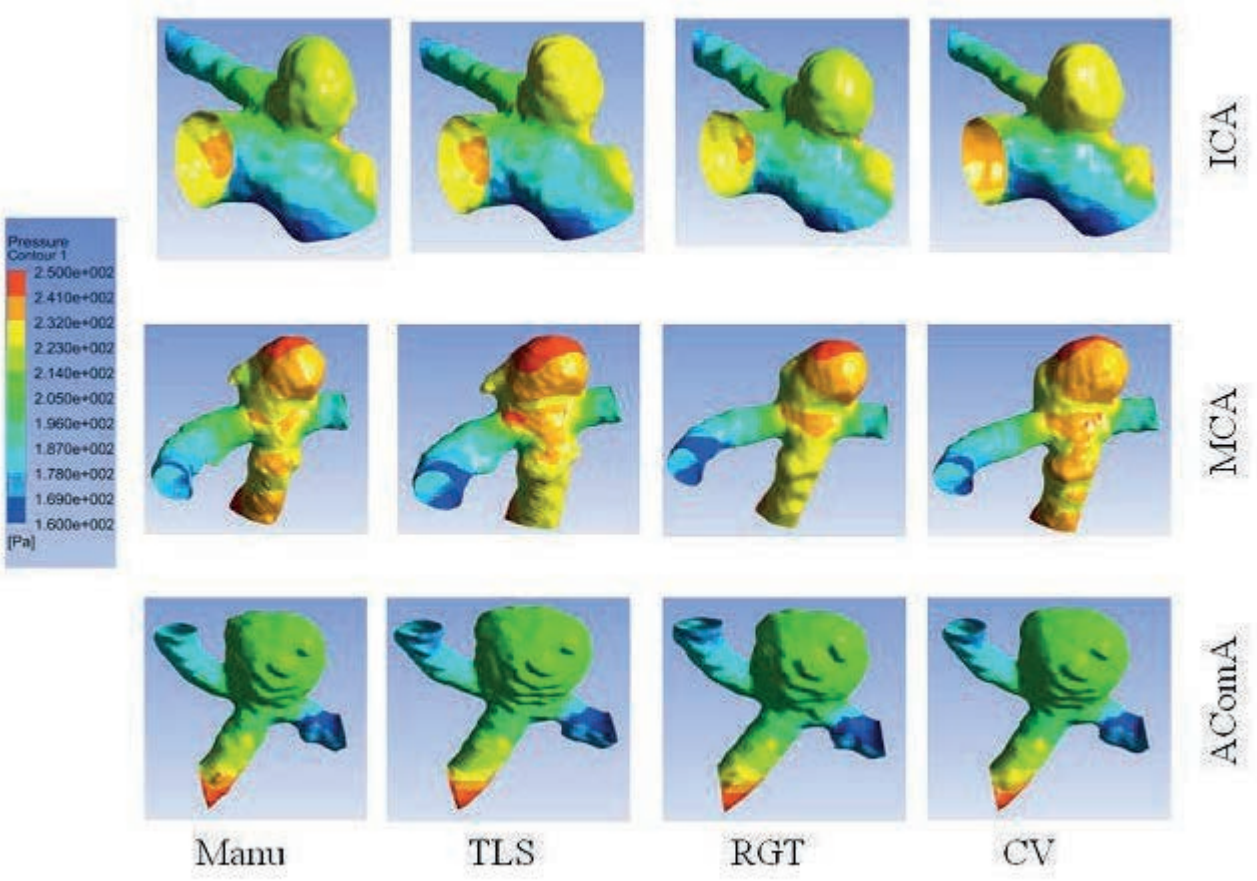

Figure 5.7: Pressure distributions.

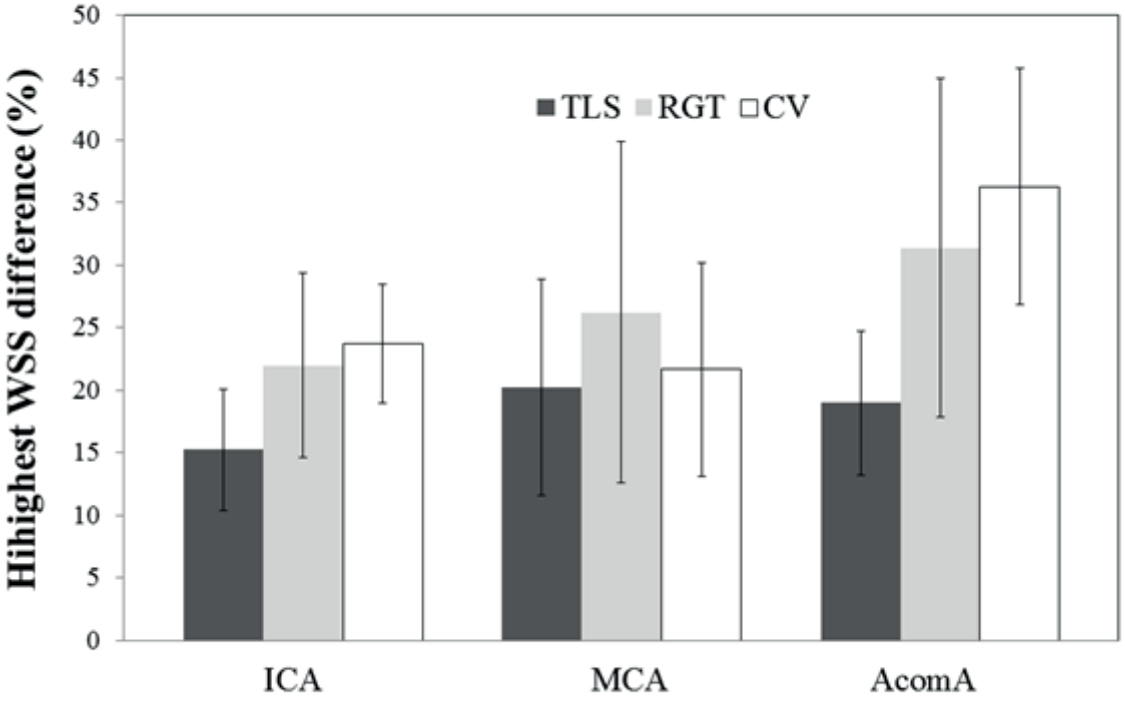

Figure 5.8: Haemodynamic results; WSS (highest volume).

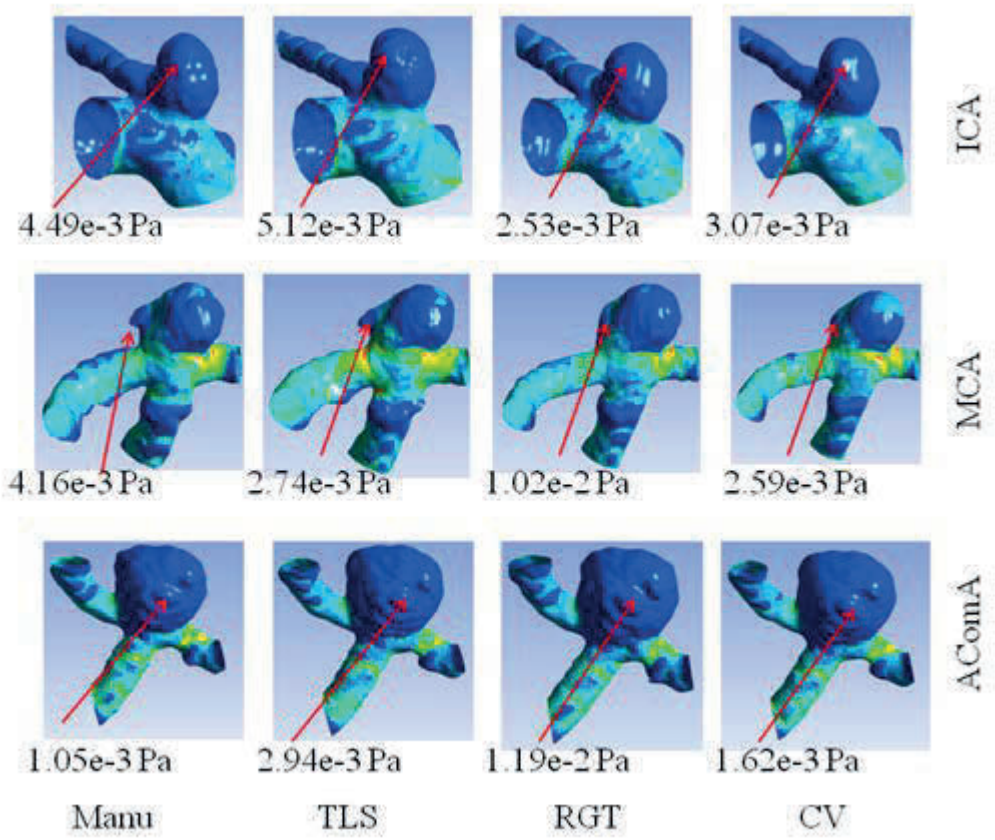

Figure 5.9: WSS distributions.

to improve upon these segmentation applications, a technique with the ability to segment aneurysms automatically without the setting of a seed point or intensity threshold, and is likewise available for the segmentation of complex cerebrovascular anatomical shapes[28]. Our results have confirmed that the reconstructed geometry, segmented via the use of TLS, is able to be controlled within an acceptable range (VD < 10% SD=±5%, JM>90%, and HD<1 Pixel), with the differences found to be significantly lower than previous methods.

Our haemodynamic results indicate that the volumes of EL difference are to be controlled to a level with deviations of less than 20% between the differing segmentation methods. The results of TLS method also reveal the lowest difference and deviation (18.2%, SD=±6.8%) when compared to the other models of segmentation. On the other hand, we found that the results of WSS were notably dependent upon technique, particularly in terms of the quality of the lowest WSS. WSS is known to be calculated via local velocity vectors near the vessel surface (Equation 4), a major reason behind its sensitivity to and influence by the local surface geometry. As mentioned in equation 2, EL is a magnitude volume which is typically only influenced by the flow parameter at both the inlet and outlet. Although the local geometry of the aneurysm likewise influences the subsequent loss of flow power, the EL values obtained have been found to lie within a statistically reasonable range. Using the TLS method, VD and overlap difference can be restricted to a certain range (ie: under VD <10% SD=±5%, JM>90%, and HD<1 Pixel). The values of EL were thus maintained at a given level throughout this study, with a deviation range below 20%. However, the results of WSS are uncontrollable and uncertain, with the maximum difference of WSS, particularly for the lowest WSS, calculated to be over 1000% (10 times) different from segmentation methods. We therefore believe that it may be enough proof to introduce WSS parameters in estimating the risk of aneurysm rupture, with further discussions to come, when these segmentation methods are fully validated.

5.6 Conclusion

Three dichotomous segmentation methods were introduced for the analysis of 45 cerebral aneurysm models in terms of geometric shape, volume, and haemodynamic results. Although based on the same medical imagery and data, differing methods of image segmentation generated alterations in shape, volume, thereby resulting in significant haemodynamic results. The results of EL were observed to be statistically stable as opposed to the relative uncertainty of the WSS, with the occurrence of uncertain results negatively affecting the accuracy of patient-specific haemodynamic applications. The TLS method was proposed to improve cerebrovascular aneurysm segmentation applications, a technique with the ability to segment aneurysms automatically without the setting of a seed point or intensity threshold, and is likewise available for the segmentation of modifiable anatomical shapes.

We believe that a validation process to confirm the results of these segmentations, will be of vital importance in limiting the error arising from such manipulations of image data. With this, the results that are influenced by the segmentation process must be included in the haemodynamic study. A series of in-vitro and in-vivo validation will thereby be performed in our future projects in order to address this issue.

Chapter 6

Validation of the Threshold-based Level Set Segmentation Method via use of Silicone Models

In chapter 5, we stated the necessity and importance of the validation process for segmentation methods applied in medical imaging. In short, all medical applications based upon medical image segmentation technique should entail a process of segmentation method validation. We conducted in-vivo validation tests via the use of eight patient-specific aneurysm cases, with the results given in chapter 4. In this chapter, we performed a series of in-vitro validation tests via the use of three designed silicone aneurysm models and a patient-specific silicone aneurysm model. These silicone models were scanned by 3D CT with four different dilution rates of contrast agent. The outcomes were then applied to validate our previously proposed segmentation method; Threshold-Based Level Set (TLS). These results were likewise employed to investigate optimal parameter settings for the best segmentation results. Four different types of silicone aneurysm models were designed for this study.

Section 6.1 will detail in brief, the current situation of segmentation method validation in intracranial aneurysms research and an introduction of in-vivo validation testing . From Section 6.2 to Section 6.4 we will explain data acquisition, segmentation methods and parameter setting and the results of these methods of evaluation. Section 6.5 will describe the results of validation, followed by discussion, which will be listed Section 6.6. In summary, validation results obtained show that at the highest contrast solution, all segmentation methods achieved an overlap rate of more than 93% and less than 0.7 pixels of MASD. Even at the lowest contrast dilution, the TLS method is able to achieve an overlap of 89%. The TLS method provided a relatively stable geometry at various contrast densities. The study validated the accuracy of the proposed TLS segmentation method and discussed the optimal parameter settings for automatic segmentation.

6.1 Background

Recently, more researchers realized the importance of segmentation method validation based on the relationship between segmentation results and its further application in intracranial aneurysm research [100, 104, 106, 125–128]. However, challenges still remain regarding the validation of any kind of segmentation methods, a point particularly true for individual patients [19, 129–131]. Bogunovic et al. [132] reported an evaluation study for automated segmentation of cerebral vasculature with aneurysms using geodesic active region method in 3DRA and TOF-MRA, Firouzian et al [91] proposed and validated a Geodesic Active Contours-based level set method which employed region information for intracranial aneurysm segmentation in CTA.

To validate our previously proposed Threshold-Based Level Set (TLS) segmentation method [78], a series of in-vivo and in-vitro validation tests were performed. The details of the in-vivo validation were introduced in Chapter 4. Four types of aneurysm models which

were designed with differing complexities of shape were introduced for in-vitro validation tests, with the in-vitro process designed as following: First, four types of silicone models, manufactured by 3D printer, were scanned via 3D CT. These silicon aneurysm models were injected with four different dilution rates of contrast agent. the outcomes were then segmented via three segmentation methods; Region Growing Threshold (RGT), and Chan-Vese model (CV). Following this, four different evaluation measures were utilized as indexes of accuracy, and compared with the results; the measurement of arterial volume differences (VD), Jaccards measure (volume overlaps metric, JM), Hausdorff distance (maximum surface distance, HD) and mean absolute surface distance(MASD). Moreover, the consistency of segmentation methods in segmented results were investigated via statistical analyses using the intraclass correlation coefficient (ICC) [133] and paired T-tests. The validation results were likewise employed to investigate optimal parameter settings for the TLS method, in order to obtain the best segmentation results.

6.2 Experiment Data Acquisition

Four types of silicone aneurysm models with different aneurysm forms including saccular, fusiform and patient specified, different size and angles of parent artery were used in this study. The silicon models were set in one plastic container and the container was filled with water during CT scan (Figure 6.1). The silicone models were scanned via use of a 3D CTA machine (GE Healthcare, Discovery CT750). The resolution of each CT image was 512×512 pixel field ($0.12\text{mm} \times 0.12\text{mm}$), with slice thickness set to 0.625mm.

The first set of data was obtained without the use of contrast (therefore rendering the models with air). The other four sets of results were obtained by using four types of diluted contrast medium; 1:5, 1:10, 1:20, and 1:40.

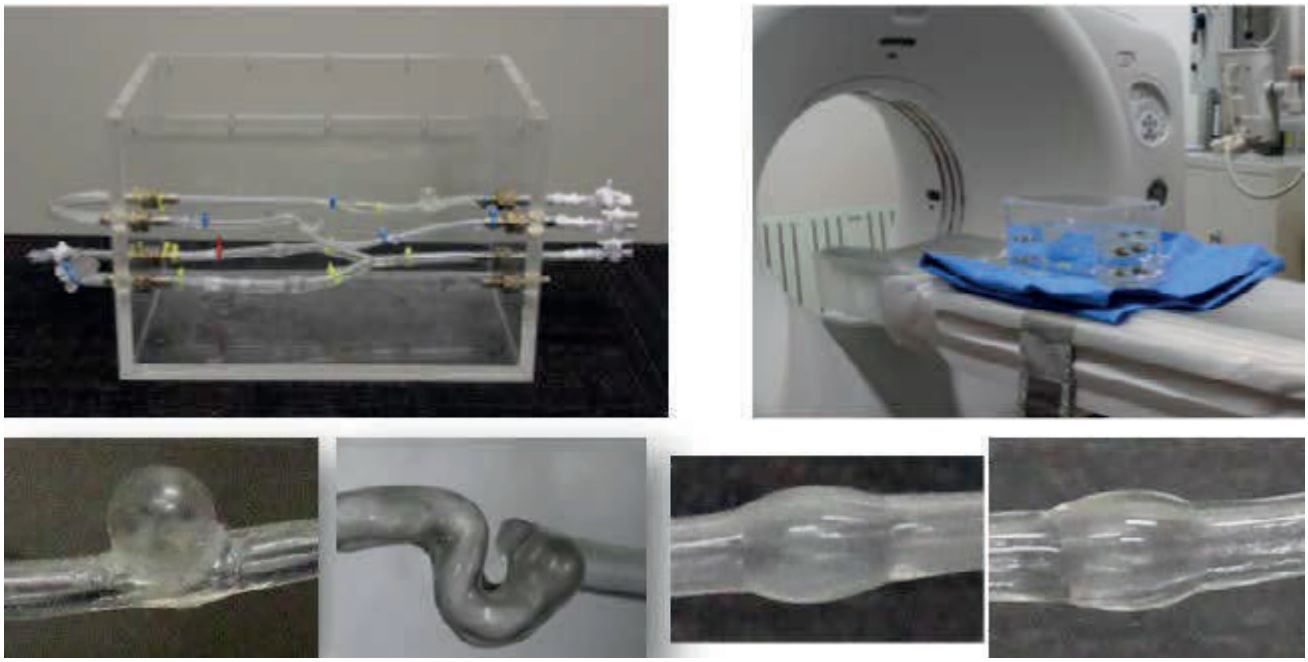

Figure 6.1: Experiment equipment. Four types of silicone aneurysm models and the CT scan. Top left: the silicone models in a plastic container. Top right: The models in the CT scan. Bottom from left to right: model 1 shift to model 4.

6.3 Contrast Medium and Dilution

The Omnipaque 350 (350 mgI/mL, Iohexol) contrast medium was used to dilute four differing amounts of contrast medium in the ratios 1:5,1:10,1:20 and 1:40 for each scan, with the dilution of the contrast medium 1:5 (D1:5, 20%) representative of one part contrast agent to four parts water. This principle can likewise be applied to the dilutions of 1:10 (D1:10, 10%), 1:20 (D1:20, 5 %) and 1:40 (D1:40, 2.5%). A histogram of the diluted intensity distributions is depicted in Figure 6.2. The intensity distributions of the real intracranial aneurysm DAS image was similar to the experiment image which utilised the D1:5 and D1:10 contrast medium. Moreover, the intensity ranges for the CTA image of the actual aneurysm, were similar to those of the experiment image, using the D1:5 and D1:10 contrast medium.

6.4 Data Preparation

For quantitative evaluation, linear registration was first performed for all five sets of data for the same silicone model, before a region of interest (ROI) was selected for all data.

6.4.1 Ground Truth

There are two ways to generate a ground truth for each silicone model in this study.

- Idealized silicone models (three designed models: model 1, model 3 and model 4): Three silicone models were ideally designed via use of an open-source Computer-Aided Design (CAD) system (FreeCAD, http://www.freecadweb.org). Figure 6.3 shows the silicone models and Table 6.1 lists all design sizes for these models. A 3D printer was used to generate 3D aneurysm models as foundations for the manufacture

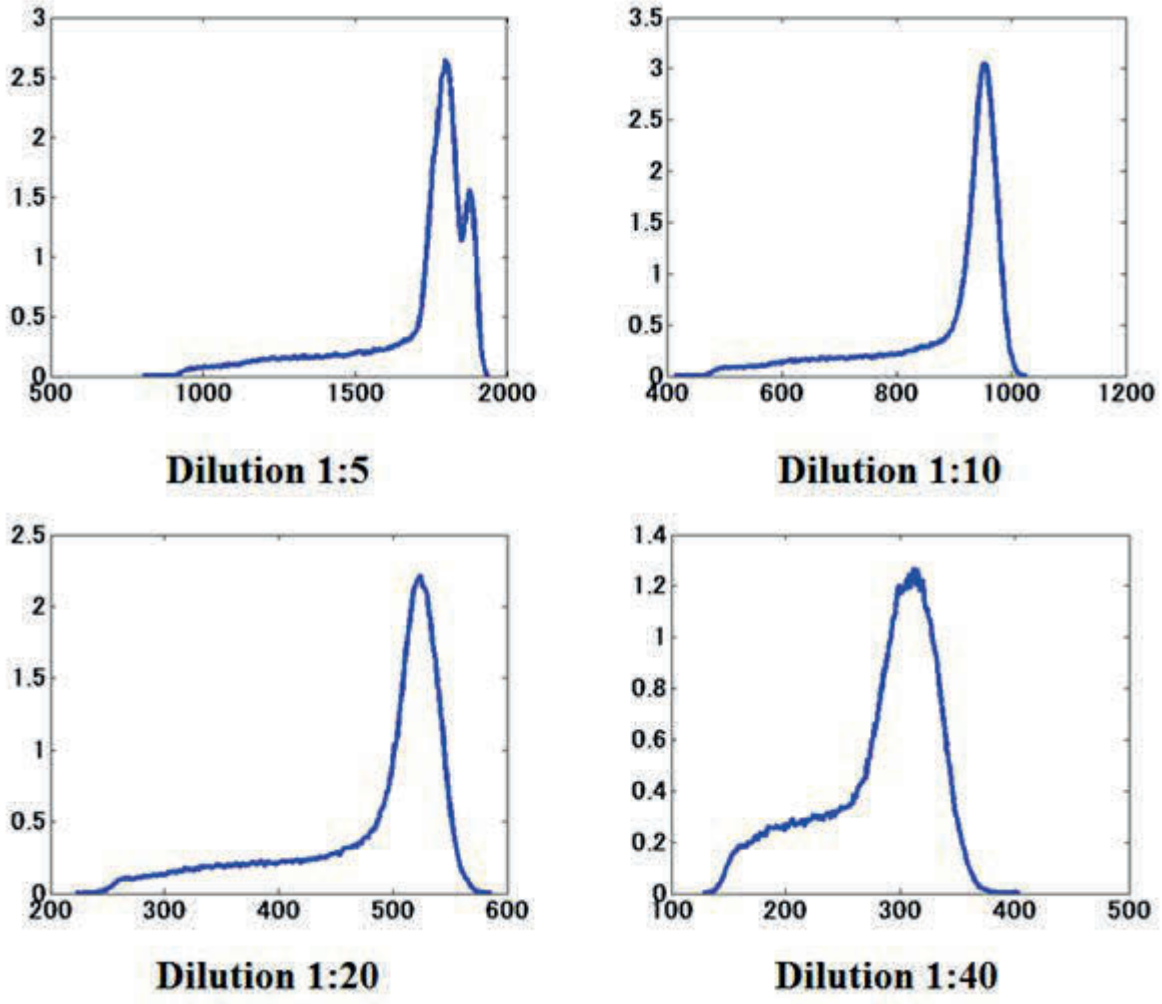

Figure 6.2: Histogram of diluted contrast medium intensity distributions (HU) in experiment images.

of silicone models. Firstly, both the non contrasted CT image data set for the silicone model and this model′ CAD model data set were imported into the 3D Slicer (open source (http://www.slicer.org)). Secondly, CAD model data set was registered and calibrated with the CT image data set. Following this, a set of binary image data for the CAD model was generated via the PolyData To Label Map module of 3D Slicer. This binary image data was used as the ground truth (GT) of the idealized silicone model in the comparison procedure. Figure 6.4 depicts an example using model 3.

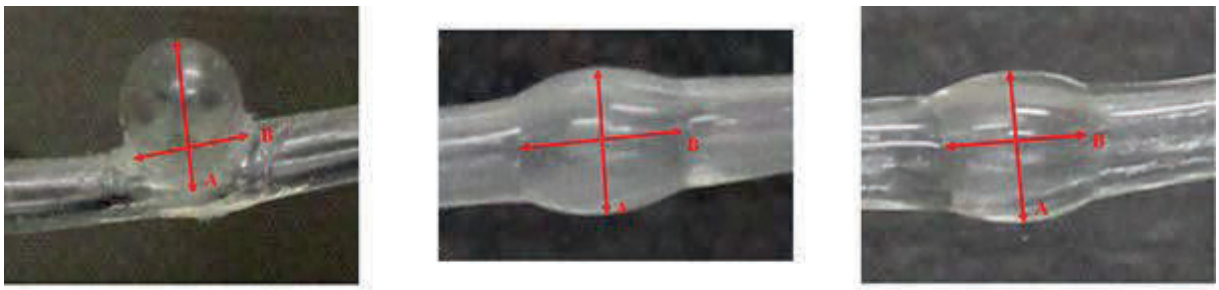

Figure 6.3: Three designed silicone aneurysm models.

	$DesignSize(mm)$			
	$BulgeDiameter(A)$	$BulgeLength(B)$	$TubeDiameter$	$Thickness$
$Model1$	14	12	6	0.6
$Model3$	10	18.32	6	0.6
$Model4$	12	18.32	8	0.6

Table 6.1: Design size of the three silicone models.

- Patient specified silicone aneurysm model (one model: model 2):

  The patient specified silicone aneurysm model is shown in Figure 6.5. To generate a ground truth for model 2, a set of data in which contrast medium was not utilised, was segmented via manual means. This manual segmentation was conducted by an experienced radiologist through the use of 3D Slicer. The result obtained via manual

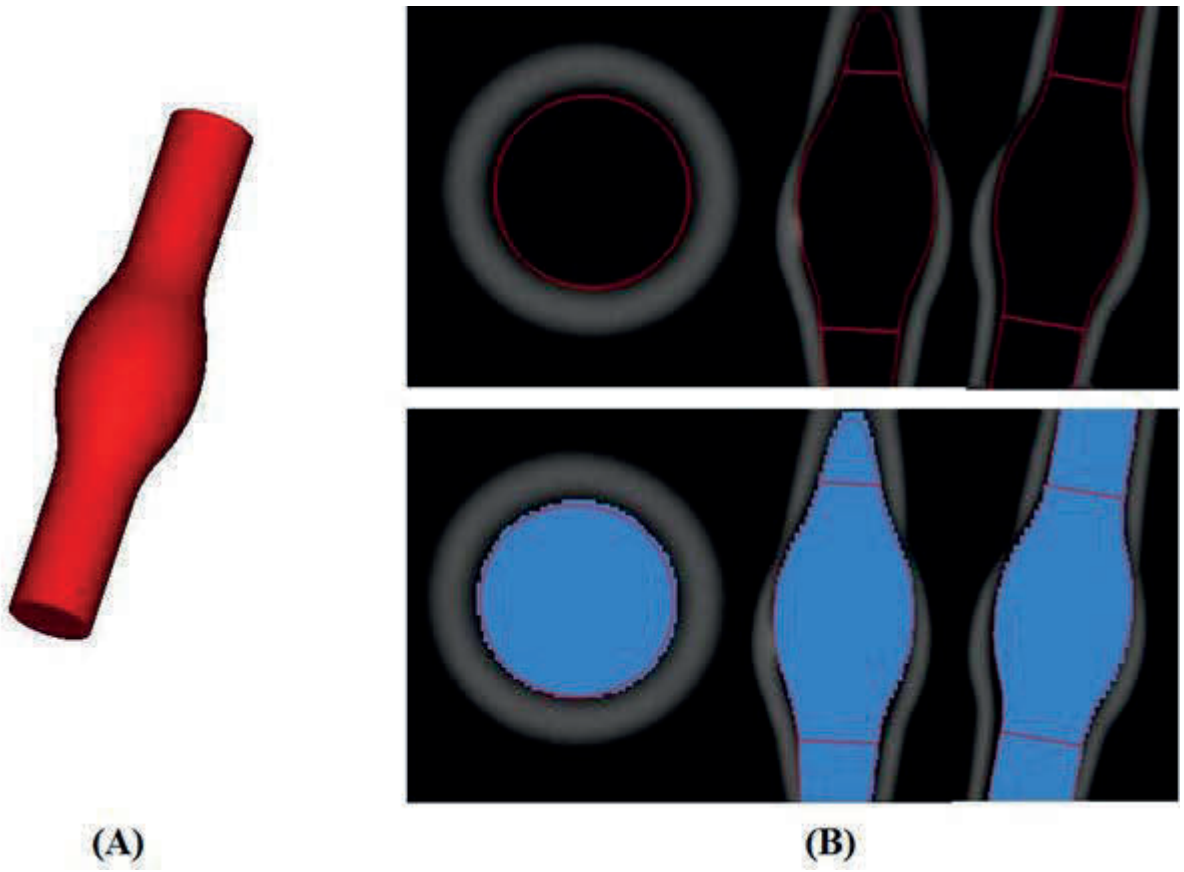

Figure 6.4: An example (model 3) for the generation of ground truth. (A) The red 3D model represents the CAD model. (B) The gray 2D images are the CT images of the silicone model, imported to 3D slicer in axial, sagittal and coronal planes; the red lines represent the surface lines of the CAD model in 2D, which are registed and calibrated with the CT image, whilst the blue area represents the generated ground truth (GT).

segmentation was utilized as the ground truth (GT) for the patient specified silicone aneurysm model.

Figure 6.5: Patient specified silicone aneurysm model.

6.5 Segmentation Methods and Parameter Setting

Three segmentation methods were introduced in this study; Region Growing Threshold Connecting (RGT), Chan-Vese model (CV), and Threshold-Based Level Set (TLS). Details of the RGT, CV and TLS approaches were described in Chapters 3 and 4. Here we focus on the setting and selection of parameters.

6.5.1 The Region Growing Threshold (RGT)

To execute the RGT segmentation method $I(X) \in [X - T_1, X + T_2]$, two initial intensity thresholds (low and high) need to be inputted. The initial high threshold value is the highest intensity of the images, with the initial low threshold, also called the seed, potentially impacting the accuracy of segmentation results. In this study, two sets of RGT segmentation results based on two initial low threshold selection technique; RGT (ave) and RGT (best), were produced for all contrast solutions and models. RGT (ave) represents the results of segmentation when the initial low threshold value was selected to be fixed at 800 HU, 370 HU, 260 HU and 180 HU for the contrast dilutions 1:5, 1:10, 1:20, and 1:40 respectively. The initial low threshold value selection was based upon the histograms of diluted contrast medium intensity distributions (HU) in the experiment images (Figure 6.2). RGT (best) represents the best segmentation results selected from a range of intensity thresholds. We performed a series of RGT segmentation for the same image with differing initial low threshold values, with the results from segmentation compared to the ground truth (GT) and the overlap rates (JM) between the results and GT calculated. Figure 6-6 indicates the relationship between the overlap rates (JM) and the initial low threshold (T) in all dilution rates and models. E.g. in Figure D1:40, RGT (best) chose the initial low threshold value 180 HU for models 2, 3 and 4, and 200 HU for model 1.

6.5.2 The Threshold-based Level Set (TLS)

The initial zero level set is a rectangular prism surface, constructed via subtraction of two pixels on either side of the ROI. Two parameters thus need to be set: α, β from the TLS equation: $\frac{\partial \varphi}{\partial t} = |\nabla \varphi| \left(\alpha (I - T) + \beta div \left(g \frac{\nabla \varphi}{|\nabla \varphi|} \right) \right)$. β is a constant of curvature smoothness; as β increases, the curvature surface becomes increasingly smoother. Because

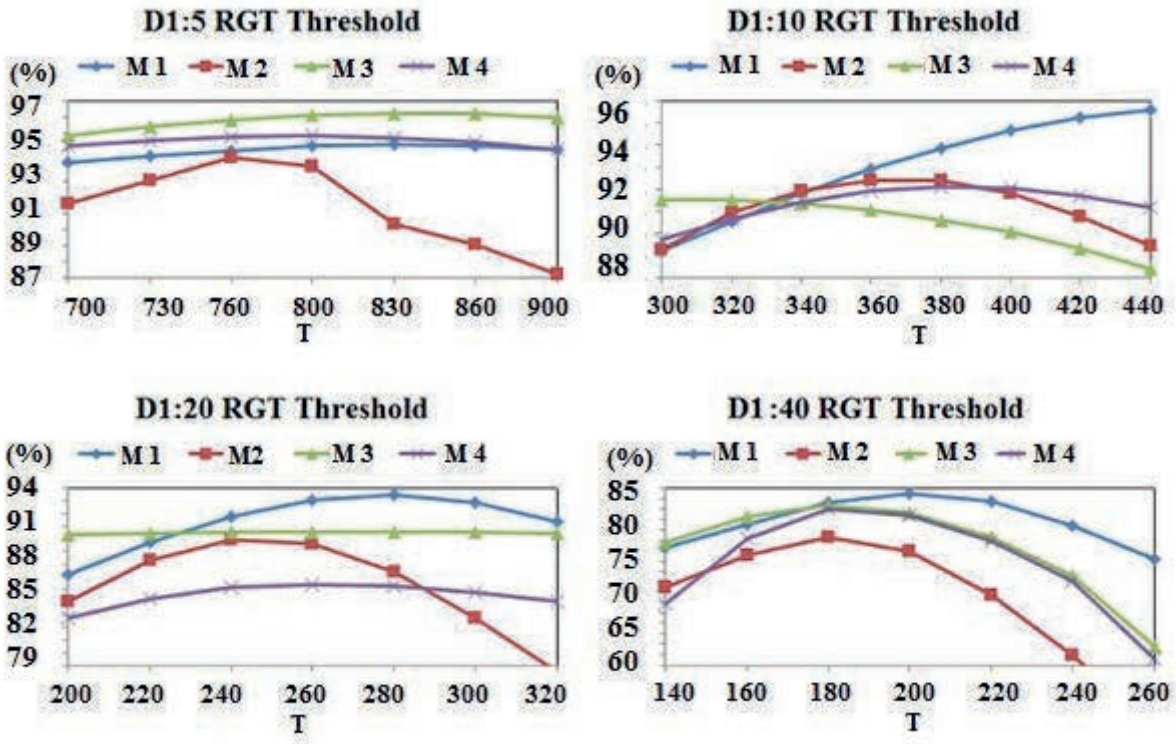

Figure 6.6: The region growing threshold selection for RGT (best). The relationship between the overlap rate (JM) and the initial low threshold (T).

the local surface shape of intracranial aneurysms are vital in preventing data loss from the aneurysm surface, in this study, we set β =1 to indicate a complete lack of smoothness. For selection of the best image propagation constant, for the application of the TLS method in intracranial aneurysm segmentation, a selection test for the image propagation constant was conducted.

6.5.2.1 TLS Image Propagation Constant α Selection Test

When β is set to 1, the image propagation constant is the only parameter to require optimization in the equation: $\frac{\partial \varphi}{\partial t} = |\nabla \varphi| \left(\alpha \left(I - T \right) + \beta div \left(g \frac{\nabla \varphi}{|\nabla \varphi|} \right) \right)$. α is a tuning parameter that allows for accurate bias adjustment of the TLS method and enables the dragging of TLS results towards a specific object of segmentation , or more precisely, an intracranial aneurysm. A validation test had been performed. In the test, we gave the image propagation constant α=5 at the first iteration, then increased by 1 at the next iteration. In each iteration, the segmentation results, e.g. volume and the mean of the aneurysm intensity value T, would change slightly. The relationship of the overlap rate (JM) and the α value is shown in Figure 6.7. From Figure 6.7 (a), we can see that the increases of JM are proportional to the rise in α across all models and dilution rates. When α=5, the JM is lower than others, meaning that the image propagation constant is not of adequate strength for the segmentation results to closely match reality. For example, in model 4, D1:5, we see that when α=5, the JM is 90%. When α rises to 10, JM is around 94%. A difference of JM for each iteration, with increasing is illustrated in Figure 6.7 (b). This figure clearly indicates that, after α rises to 15, the difference for the overlap rate (JM) is around zero for all models and dilution rates. Based on the test results of TLS image propagation for constant α, we suggest the use of the parameter $\alpha \geq 15$ or the accuracy of the TLS result. In this study , we will use α=15.

6.5.3 The Chan-Vese model (CV)

The initial zero level set for CV model is a cuboid surface, constructed in the same manner as the TLS method. we used a fixed setting for the parametters in the equation: $\frac{\partial\varphi}{\partial t} = |\nabla\varphi| \left[\lambda_2 \left(I - \mu_{out}\right)^2 - \lambda_1 \left(I - \mu_{in}\right)^2 - \alpha + \beta div\left(\frac{\nabla\varphi}{|\nabla\varphi|}\right)\right]$. For all models and dilution rates; $\lambda_1 = \lambda_2 = 0.005$, $\alpha = 0$, $\beta = 1$.

6.6 Segmentation Results Evaluation Methods

Silicone model volume size was calculated through use of the boundary geometry, segmented by various segmentation methods. The volume difference (VD) was calculated via utilisation of the equation, $VD = \left|\frac{(V_s - V_g)}{V_g}\right| \times 100\%$, where V_g represents the volume of GT and V_s represents the volume of the TLS, RGT or CV methods. Jaccards measure (JM) is a volume overlap metric, utilised to count the percentage of voxel intersections for the paired segmentations.

$JM = \frac{2\times|V_g \cap V_s|}{V_g \cup V_s}$, where V_g represents the voxels created by the GT and V_s the voxels generated through use of the TLS, RGT or CV methods. Hausdorff distance (HD) measures the maximum surface distance. This measure is extremely sensitive to outliers and may not reflect the overall degree of correlation. The mean absolute surface distance (MASD), indicates the average degree of difference between two surfaces and does not depend on aneurysm size.

To evaluate the efficacy of the segmentation methods across all dilution rates for the segmented results from the four silicone models, the intraclass correlation coefficient (ICC), a statistic tool, was employed to assess inter-method consistency, e.g. TLS vs. RGT, or TLS vs. CV. The ICC was defined as $ICC = \frac{M_D - M}{M_D + (k-1)M}$ where M_D represents the data variance for the contrast agent and the model variability and M, the residual variance due to the difference between segmentation methods, k represents the number

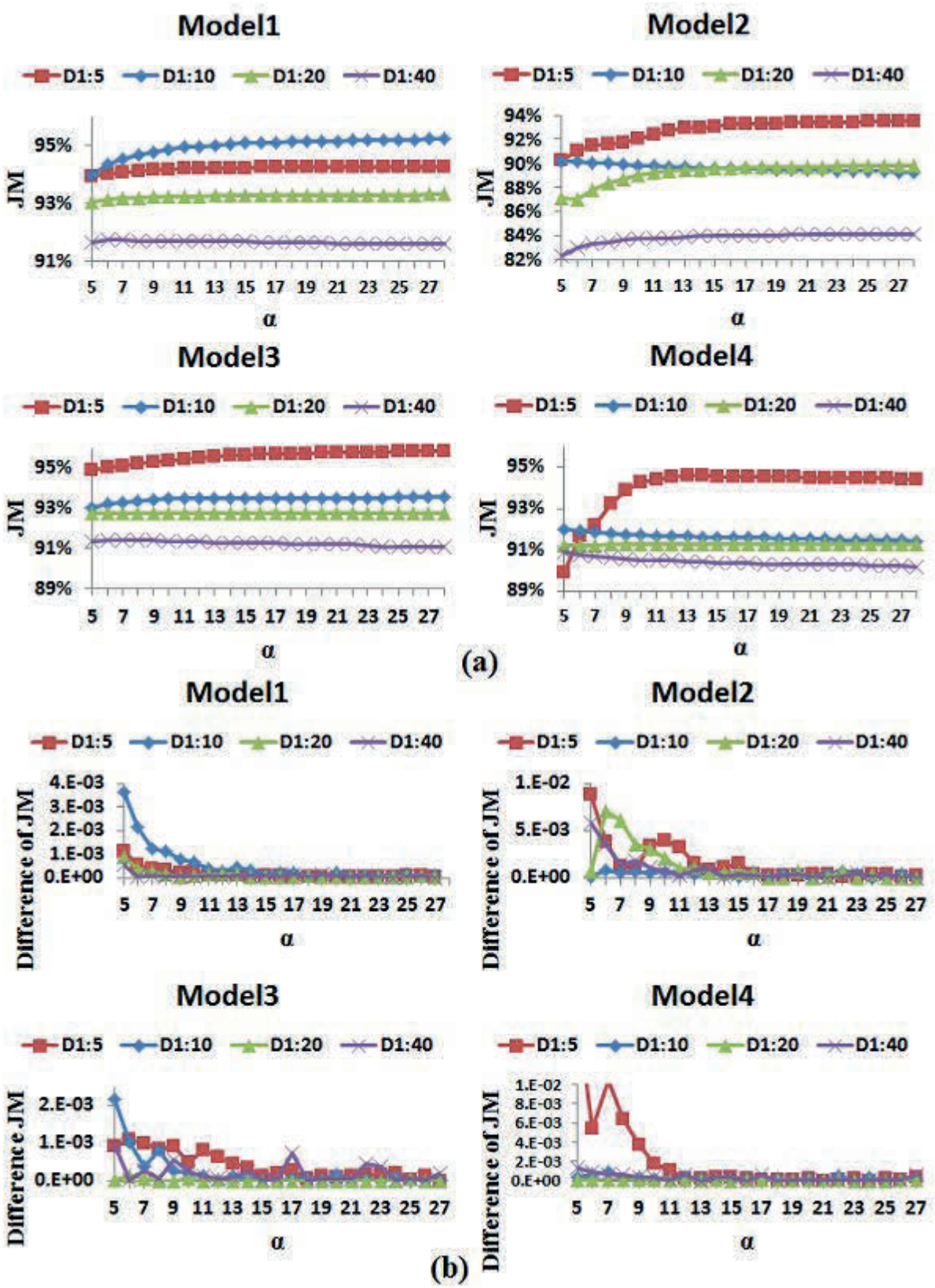

Figure 6.7: TLS image propagation constant selection test results. (a) The overlap rate (JM) versus . (b) The difference of JM versus .

of different methods compared, namely k=2 in this study. The ICC ranges from 0 to 1, indicating the degree of inter-method consistency. When $ICC = 1$, the two segmentation methods compared are of high consistency, the results of segmentation will thus not be impacted by the methods used.

6.7 Results

6.7.1 TLS Segmentation Results

Two types of TLS segmentation results are listed in Table 6.2. In Table 6.2, the volume and the mean of the boundary threshold (T) of the models were directly calculated via use of the TLS method, and the volume overlap rate (JM), the volume difference, the maximum surface distance (HD) and the mean absolute surface distance (MASD) were obtained from the TLS method for comparison with the ground truth. Figures 6-8 illustrates the TLS segmented results of all models in 2D and 3D. The highest volume overlap rate (JM) was observed in the contrast dilution rate D 1:5 for all models. The poor performance of JM between all models was perceived in the patient specified model (model 2). The biggest volume difference (VD) was also seen in the patient specified model regardless of contrast dilution rates. Models 1 and 2 feature the largest HD across all contrast dilution rates. HD measures the maximum surface distance between TLS and the ground truth and is sensitive to outliers. In this study, Figures 6.8(a) Model 1 and Figures 6.8(b) Model 2 (blue arrows) clearly illustrate that the outliers were found in the aneurysm neck position, the bleb location and the vessel bending point. The mean absolute surface distance (MASD) measures the average surface difference between TLS and the ground truth. The results show that all models in all contrast dilution rates expressed less than a 1.5 pixel difference, when compared with the ground truth. Even Models 1 and 2, though having the higher HD, indicating a difference in location, had a

MASD that was relatively small as MASD reflects the overall degree of correlation. In summary, TLS exhibited better performance in high contrast medium situations. The reason for this is that a high contrast medium would make the boundary between models and the background sharper within CTA scan images. Its boundaries are crisp steps, not gradual, thus a good quality of images contributes to a greater segmentation result. The model shapes impact some TLS results slightly, e.g. HD, VD. Overall, TLS results were not impacted by model shapes in high contrast medium situations.

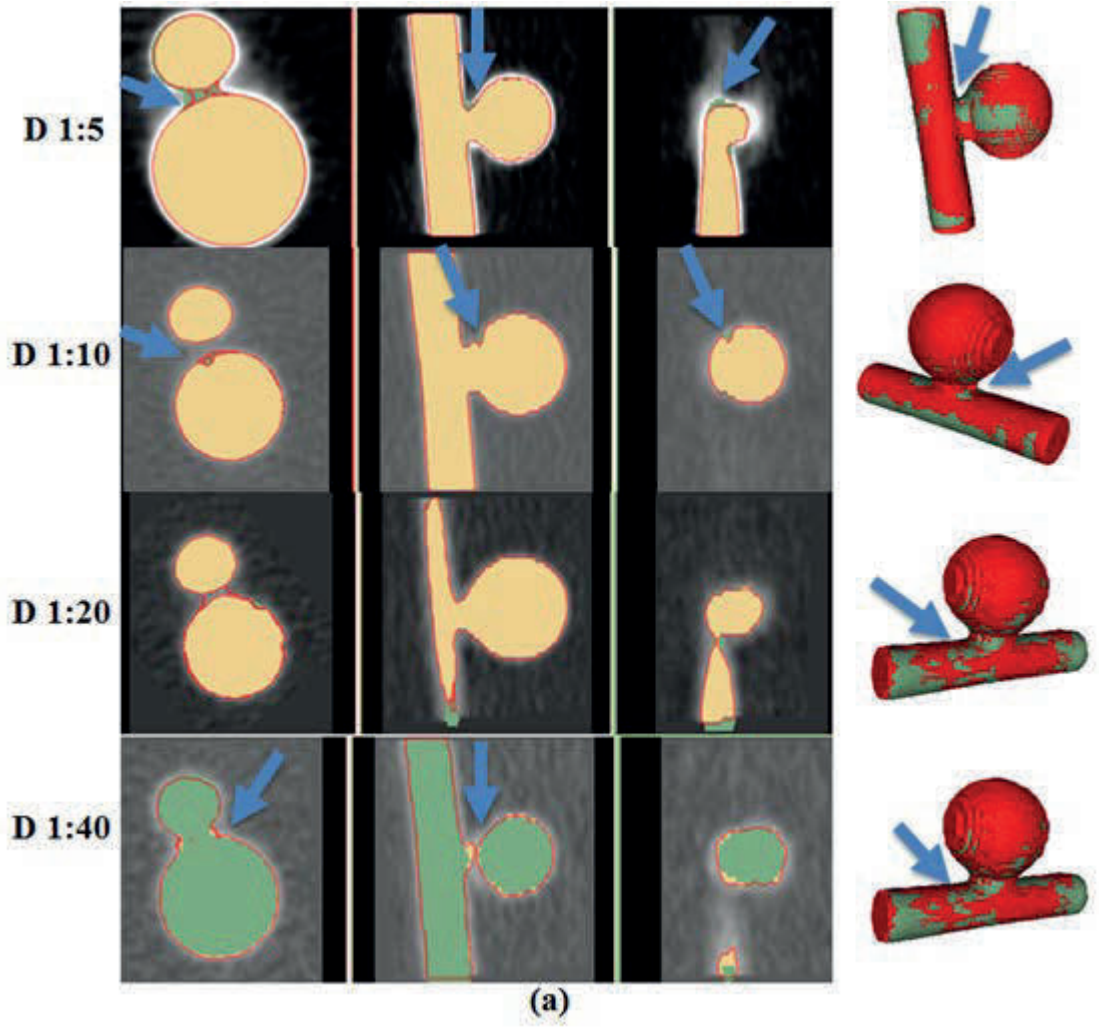

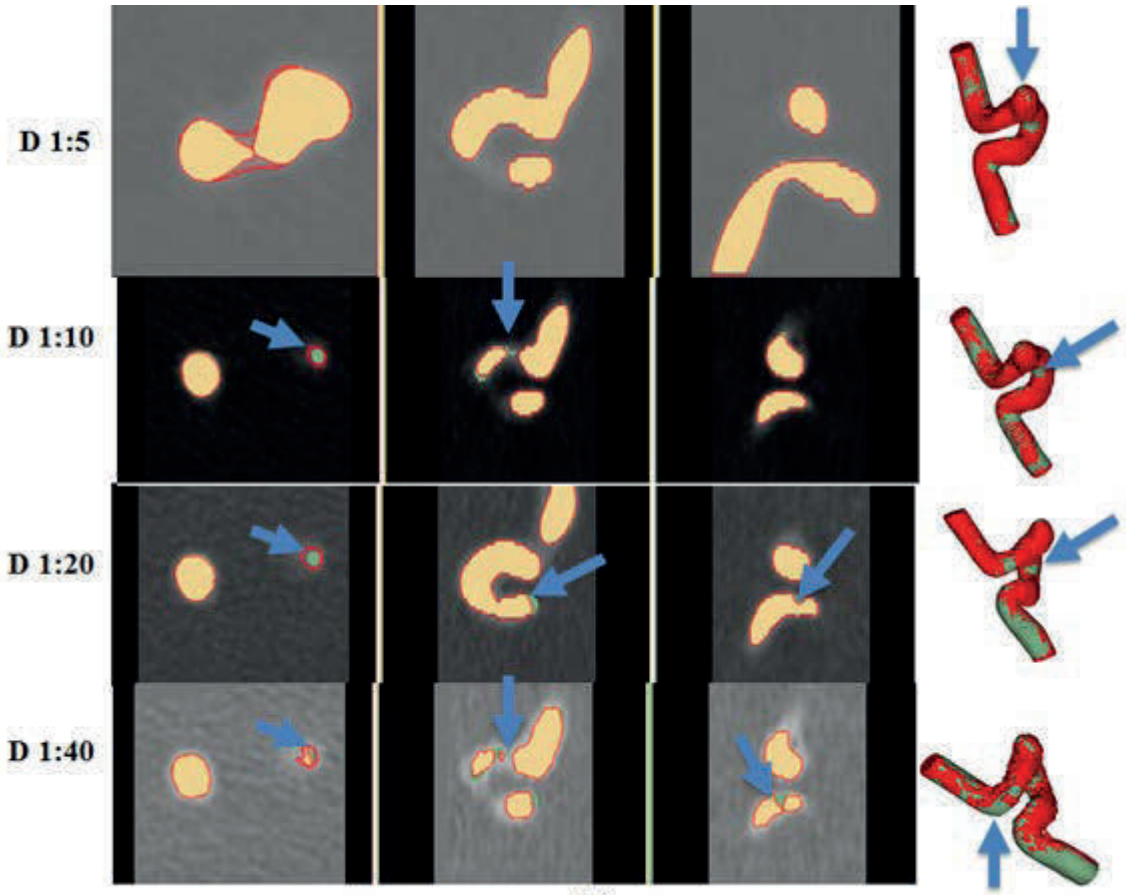

(b)

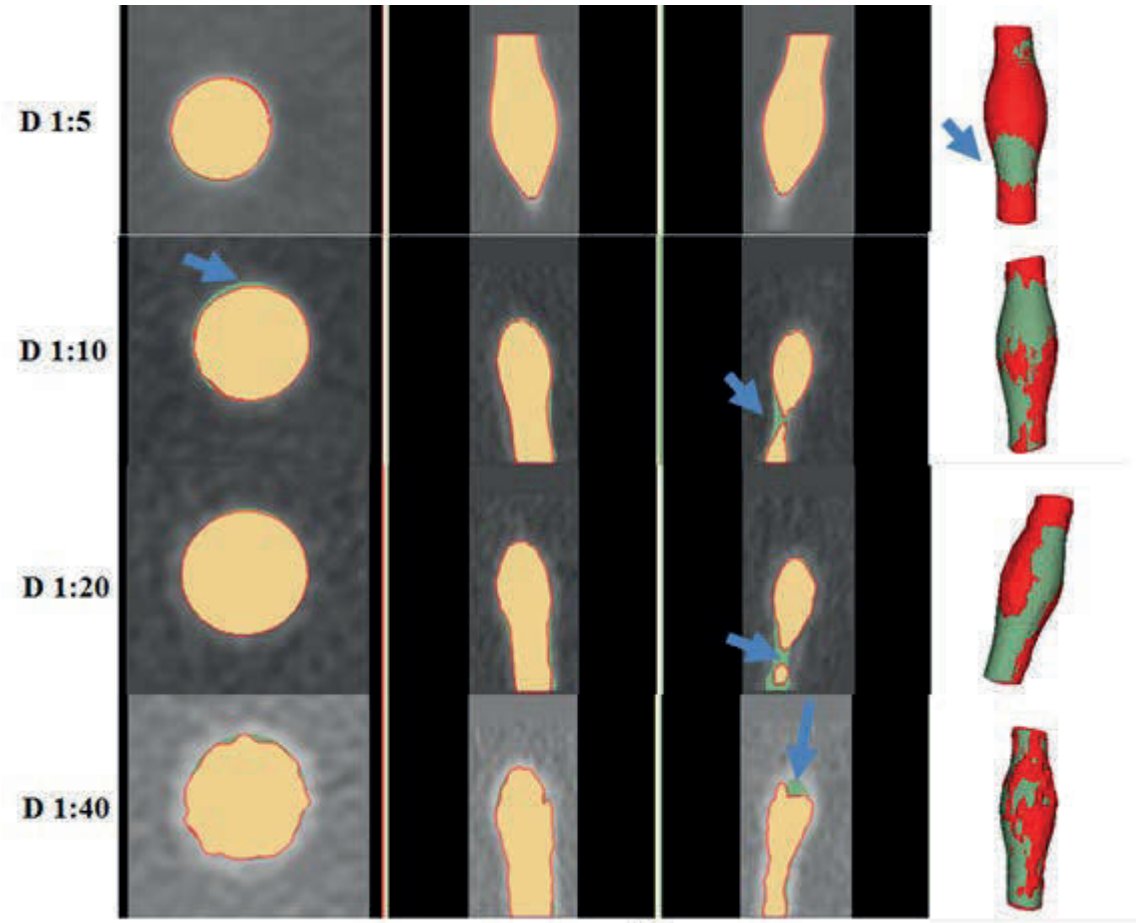

(c)

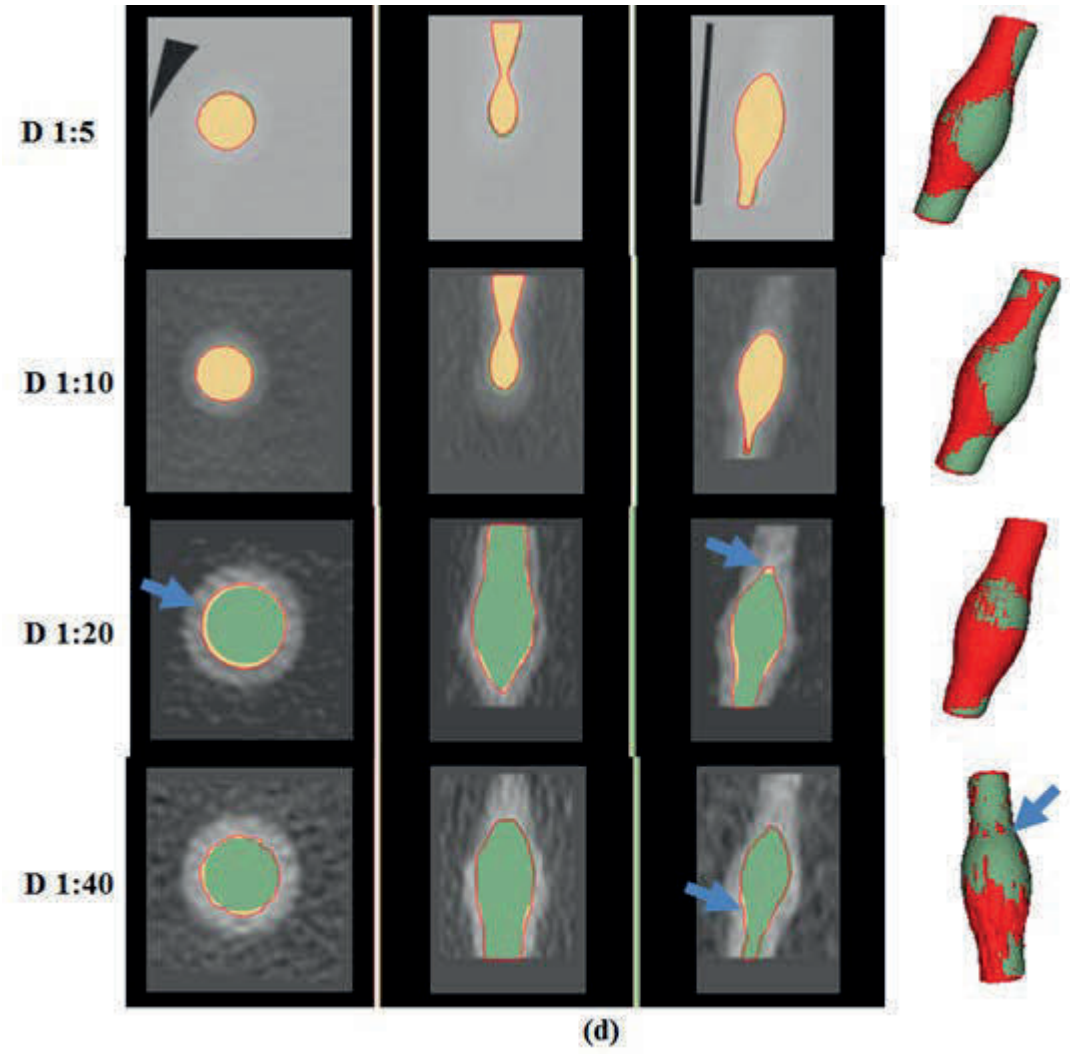

Figure 6.8: TLS segmentation results of model 1 (a), model 2 (b), model 3 (c) and model 4 (d), in 2D and 3D. The grey image is a CT scan image, the beige image is the TLS segmented result and the green image represents the ground truth image. The blue arrows point to a difference in the location. Row 1: contrast dilution 1:5, row 2: contrast dilution 1:10, row 3: contrast dilution 1:20, and row 4: contrast dilution 1:40.

	$Model1$	$Model2$	$Model3$	$Model4$	$Mean \pm SD$
$D1:5$					
$Volume$	2448.02	1299.11	1396.10	1392.26	
T	898.09	677.32	849.80	916.54	
$JM(\%)$	94.24	92.31	96.08	92.32	93.74±1.80
$VD(\%)$	0.01	6.45	0.69	6.66	3.45±3.59
$HD(pixel)$	7.51	5.63	4.10	4.84	5.52±1.47
$MASD(pixel)$	0.71	0.76	0.47	0.86	0.70±0.17
$D1:10$					
$Volume$	2506.76	1207.68	1400.26	1351.31	
T	456.46	440.51	308.22	463.13	
$JM(\%)$	93.09	91.97	91.62	91.86	92.13±0.65
$VD(\%)$	0.70	4.69	0.92	1.43	1.95±1.85
$HD(pixel)$	9.18	5.64	5.80	7.85	7.12±1.70
$MASD(pixel)$	0.60	0.77	0.99	0.91	0.81±0.17
$D1:20$					
$Volume$	2396.85	1299.08	1390.47	1542.07	
T	293.03	251.43	179.35	312.15	
$JM(\%)$	93.35	90.15	90.70	90.18	91.10±1.53
$VD(\%)$	0.89	3.74	1.23	1.34	1.80±1.31
$HD(pixel)$	13.36	12.85	6.50	12.11	11.21±3.18
$MASD(pixel)$	1.23	0.88	0.99	1.18	1.07±0.16
$D1:40$					
$Volume$	2403.13	1257.20	1333.02	1337.07	
T	218.34	196.97	200.86	202.24	
$JM(\%)$	91.76	82.87	91.31	91.00	89.24±4.26
$VD(\%)$	1.70	9.16	2.82	1.98	3.91±3.53
$HD(pixel)$	11.36	13.90	10.52	6.15	10.48±3.22
$MASD(pixel)$	1.24	1.41	0.98	0.96	1.15±0.22
$Mean \pm SD$					
$Volume$	2438.69±50.78	1265.77±43.47	1379.96±31.55	1405.68±93.89	
$JM(\%)$	93.11±1.03	89.33±4.41	92.43±2.46	91.34±0.95	
$VD(\%)$	0.84±0.69	6.01±2.38	1.42±0.96	2.85±2.56	
$HD(pixel)$	10.35±2.55	9.51±4.49	6.73±2.72	7.74±3.16	
$MASD(pixel)$	0.94±0.34	0.95±0.31	0.86±0.26	0.98±0.14	

Table 6.2: TLS segmentation results.

6.7.2 Segmentation Methods Comparison Results

Comparison of all segmentation methods are listed in Table 6.3. These segmentation results were generated via TLS, RGT and CV methods. Two results, however, were produced via the RGT method - RGT (best) and RGT (ave). Details are listed in Section 6.5.1. In total, four segmentation results as evaluated by JM, VD, HD and MASD were compared in this section. By comparing these segmentation results in different models and under medium contrast dilution rates, we aim to investigate the applicability, accuracy and alternatives of segmentation methods when utilised in certain situations.

Figure 6.9 a) depicts the volume overlap rate (JM) by models. The TLS achieved a JM of over 89% across all models. The JM value of model 2 revealed the lowest value across all segmentation methods. As model 2 has the most complex shape, it indicates that the shape of the model could have impact upon volume overlap rate. Figure 6.9 b) indicates the overlap rate (JM) by dilution. When the contrast agent decreased from high D1:5 to low D1:40, the value of JM declined across all TLS, RGT and CV methods, with the average overlap ratios found to be 91.70±2.92%, 89.59±4.30%, and 83.03±11.46% for TLS, RGT (ave), and CV respectively. When compared to other methods, the TLS method appears higher in terms of overlap ratio.

Figure 6.10 a) depicts the volume difference (VD) across various models. The largest VD was recorded in model 2, across all segmentation methods. The VD for model 2 were found to be : 6.01±2.38%, 11.13±5.10% and 33.92±30.31% for TLS, RGT (ave), and CV respectively.

Figure 6.10 b) illustrates volume difference (VD) by dilution. The highest VD across all methods was recorded with a dilution of 1:40. These were 3.91±3.53%, 12.77±4.74% and 52.62±24.93% for TLS, RGT (ave), and CV respectively. The TLS method appears lower in terms of VD than the other methods. The VD of the TLS was found to be under 7%, across all models and contrast dilutions.

$(CI = 95\%)$	$Mean \pm SD$	Min	Max
TLS			
$JM(\%)$	91.70±2.92	90.15	93.26
$VD(\%)$	2.78±.65	1.37	4.19
$HD(pixel)$	8.58±.31	6.82	10.35
$MASD(pixel)$	0.93±.25	0.80	1.06
$RGT(best)$			
$JM(\%)$	91.81±3.14	90.14	93.48
$VD(\%)$	1.05±0.80	0.63	1.48
$HD(pixel)$	8.03±2.84	6.51	9.54
$MASD(pixel)$	0.94±0.39	0.73	1.15
$RGT(ave)$			
$JM(\%)$	89.59±4.30	87.30	91.89
$VD(\%)$	6.84±4.89	4.23	9.45
$HD(pixel)$	8.83±3.48	6.97	10.69
$MASD(pixel)$	1.10±0.44	0.86	1.33
CV			
$JM(\%)$	83.03±11.46	76.93	89.14
$VD(\%)$	20.40±23.80	7.72	33.08
$HD(pixel)$	15.02±9.09	10.18	19.86
$MASD(pixel)$	1.45±1.03	0.91	2.00

Table 6.3: Comparison of segmentation methods.

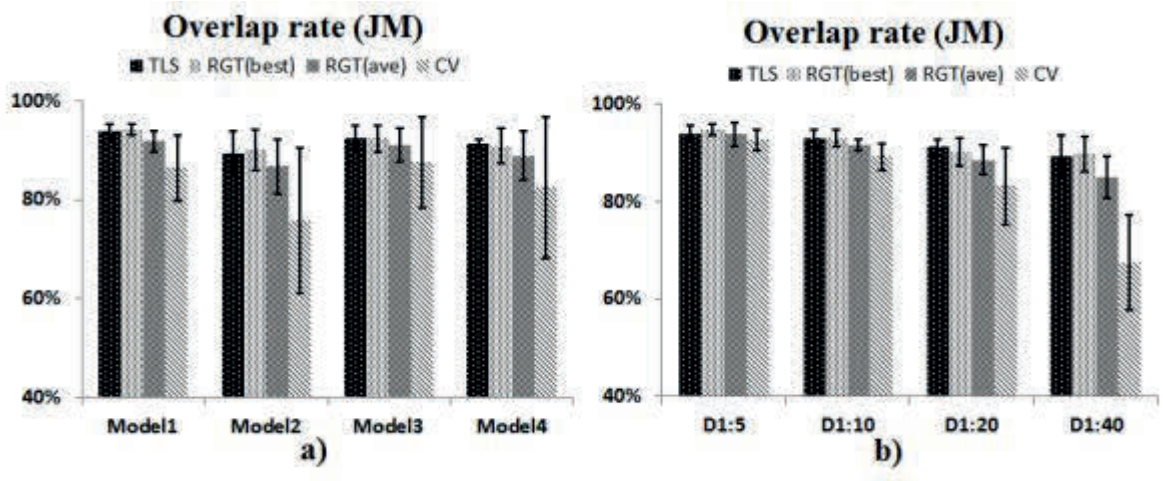

Figure 6.9: Volume overlaps results comparison by model and contrast medium dilution.

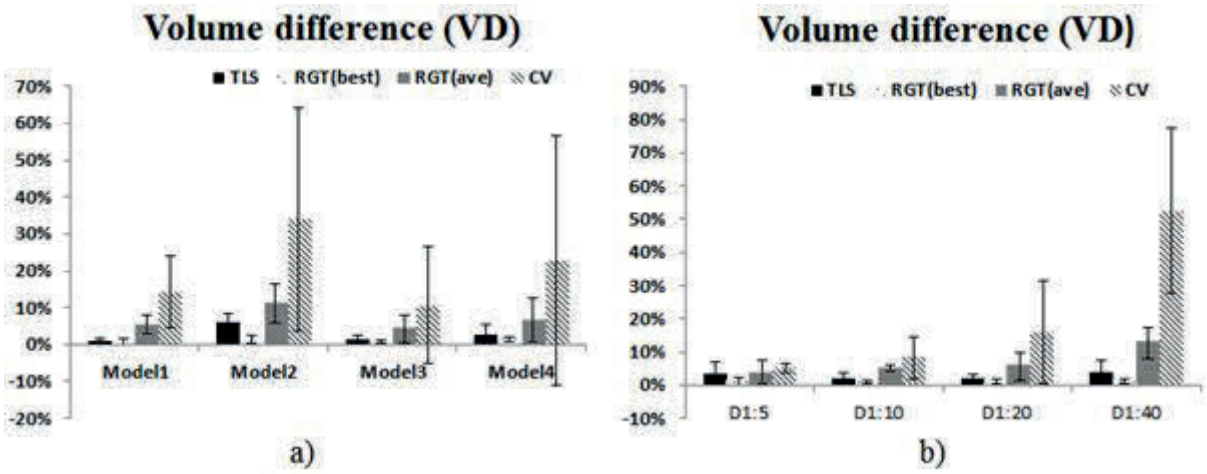

Figure 6.10: Volume difference against segmentation methods by model and contrast medium dilution.

	$TLSvs.RGT(best)$		$TLSvs.RGT(ave)$		$TLSvs.CV$	
	ICC	$P-value$	ICC	$P-value$	ICC	$P-value$
JM	0.90	0.754	0.81	0.002	0.36	0.002
VD	0.19	0.014	0.44	0.001	0.09	0.007
HD	0.81	0.259	0.70	0.712	0.38	0.004
MASD	0.68	0.883	0.66	0.045	0.20	0.043

Table 6.4: Statistical results.

HD measurements indicate the maximum surface distance to outliers (Figure 6.11). MASD represents the mean absolute surface distance (Figure 6.12). The largest HD and MASD were found to be: 11.21±3.18, 1.15±0.22; 13.26±1.30, 1.45±0.17; 22.29±10.43, 2.68±1.36 pixels through all models and contrast dilutions for TLS, RGT (ave), and CV respectively. The TLS method appears lower in terms of HD and MASD when compared to other methods.

Furthermore, as RGT is a semi-objective method, the intensity threshold setting may affect the results of segmentation From Figure 6.9, we can see that the JM of RGT (best) was better than the JM of TLS in model 2 and the contrast solutions D1:5 and D1:40. The RGT (best) also achieved, VD was lower than 1.48±1.10%, whilst the largest of HD was 11.05±0.47 pixels and the largest of MASD was found to be 1.27±0.58 pixels across all models and contrast solutions.

In this study, we found that model geometry shape has significant impact upon segmentation results in the aneurysm neck, bleb and bending locations. In Model 1, the segmentation results obtained from the TLS method indicated that JM was higher, VD and MASD was lower. This means that the TLS method was able to achieve high quality, global segmentation results. Despite this, the segmentation result HD, linked to local geometry shape, was high. As mentioned in Section 6.7.1 and Figure 6.8, the most outliers and differences were found to occur in the aneurysm neck, bleb and bending positions. Model 1 represents a saccular neck aneurysm. Other methods exhibited the same results as the TLS in Model 1. Model 2 is a patient-specified aneurysm model characterised by a greater number of bends and a complex structure. The global segmentation results JM, VD and the local segmentation result HD all exhibited poorer performance. Secondly, we found that apart from TLS method, both the RGT and CV also exhibited better performances in high contrast medium situations. A high contrast medium contributes to image quality with a sharp boundary, and allows for greater segmentation results across

all segmentation methods.

In summary, the TLS method exhibited better performance in JM, VD, HD and MASD when compared to RGT and CV methods under automatic operation. Although the RGT method is able to achieve the best performance (RGT (best)) when the initial threshold is set at the right value, it is hard to achieve this, especially in an automatic manner.

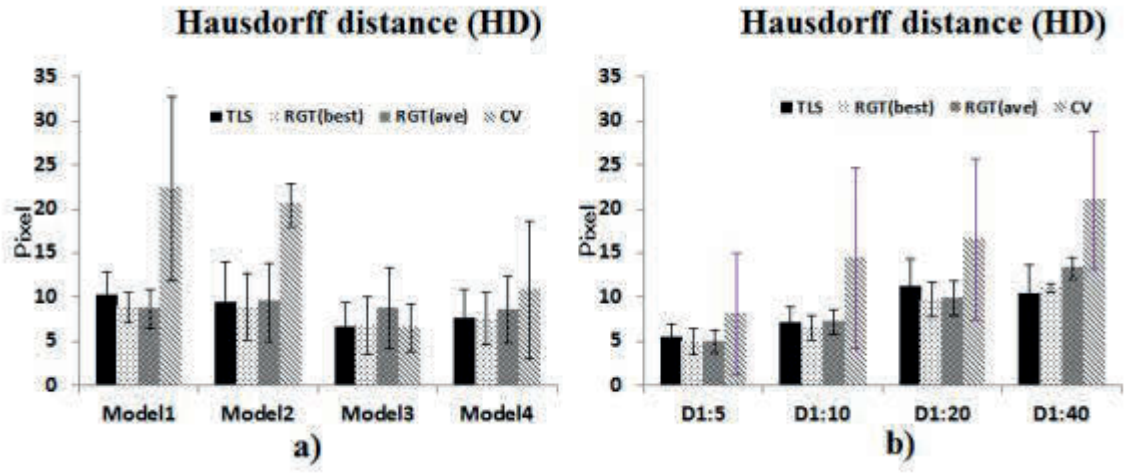

Figure 6.11: The maximum surface distance (HD) against segmentation methods by model and contrast medium dilution.

6.7.3 Statistic Analysis

The intraclass correlation coefficient (ICC) and the paired T-tests were performed upon three pairs of segmentation methods in order to evaluate their consistency in determining the values of JM, VD, HD and MASD, as depicted in Table 6.4. Excellent inter-method consistency and no statistically significant differences were found for JM for TLS vs. RGT(best) as ICC=0.90, p value=0.754. This indicates that the use of both segmentation methods were seen to generate statistically similar results in JM. Good agreement with no statistically significant differences were found for HD for both TLS vs. RGT (best) and TLS vs. RGT (ave) (ICC $\geq$0.70, p value $>$0.05). This indicates that both TLS and RGT

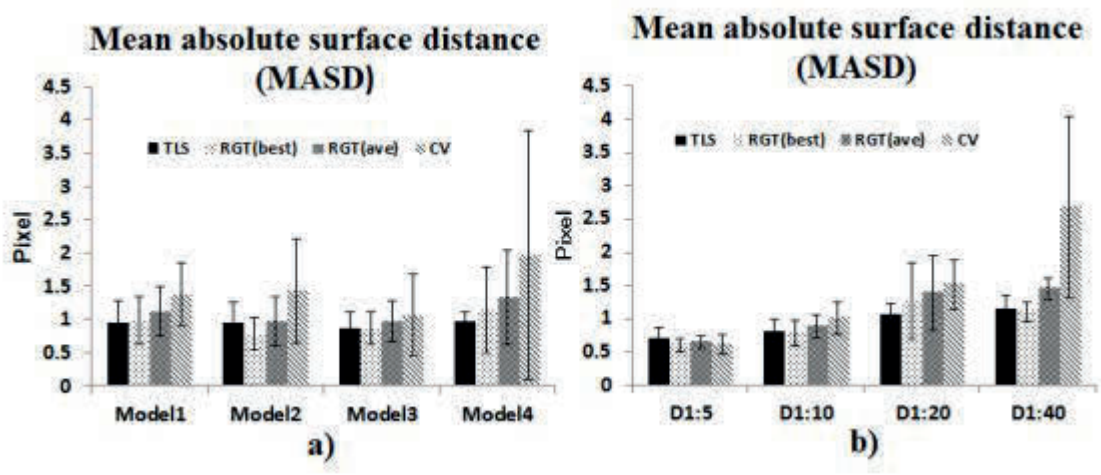

Figure 6.12: The mean absolute surface distance (MASD) against segmentation methods by model and contrast medium dilution.

(best) produced similar values for JM and HD, indicating that the two methods have a high degree of substitutability. RGT (best) exhibited the best segmentation result (Table 6.3 in this study, however, this was difficult to achieve, as the perfect initial threshold was hard to detect. As an alternative method, the TLS is able to achieve a similarly high level of performance under automatic situations.

The poorest value of ICC and statistically significant differences were found for VD across all comparison pairs and for all parameters characterized in TLS vs. CV (ICC $\leq$0.44, p value < 0.05). This raises implications for the application of particular segmentation methods when calculating specific results, particularly VD the value for which proved the most difficult to ascertain statistically significant outcomes.

6.8 Discussion

We used silicone models as an object of experiment. It is easy to use its actual size to calculate the real volume of the models. Based on this real volume, we are able to generate

to a greater degree of accuracy, the ground truth (GT) to validate the TLS method.

The shapes of both model 3 and 4 were simpler than model 1, but performance was found to be poorer when compared to model 1. This is due to the fact that neither model 3 nor 4 were connected in a Y shape. Moreover, as models 3 and 4 were not isolated, the shapes were more complex than that of model 1.

The segmented objects are intensity inhomogeneous, especially in the boundary area of objects - a common problem existing in medical imaging segmentation. It is clear, however, that this problem exists in low contrast medium dilution rates for CT scan images, more than they do for the high dilution rates in this study. Although the TLS is able to use region information to overcome this problem, performance in the low contrast medium dilution rates was found to be poorer than high dilution rates.

The influence of this problem on CV method performance is obvious. Although CV performs well when image contrast is high (more than 10%), its performance decreases very quickly with the contrast, in comparison to other methods which are more robust to contrast level. One possible reason for this, is that the homogeneity assumption of the CV model cannot be guaranteed in low-contrast images [99].

6.9 Conclusions

In this in-vitro study, a series of CT scans of silicone aneurysm models (SAM) were conducted in this study, with four different silicone models and four rates of contrast agent dilution used to generate various image data sets for validation of our previously proposed TLS segmentation method. The TLS method was able to achieve over 89% of the volume overlap rate and under 7% of the volume difference across all different degrees of silicone model shape complexities and contrast agent dilutions. We compared TLS with RGT and CV to investigate the influence of different methods on segmentation

results. For various level of contrast agent, TLS vs. RGT (best) exhibited reliability in overlap rate (JM) and HD, but no consistency in VD. CV reported a high JM and low MASD only under high contrast conditions. The study also found that the VD of each segmentation result was highly dependent on the method of segmentation. The TLS method is a technique with the ability to segment intracranial aneurysms automatically without the setting of a seed point or intensity threshold, and is likewise available for the segmentation of modifiable anatomical shapes. This method is thus a valuable tool for clinical diagnosis and surgical preparation, and will furthermore, play a vital role as an important tool for future haemodynamic research.

Chapter 7

Conclusions and Future Work

7.1 Conclusion

The primary focus of this thesis is on the development of an automatic technique enabled to detect local geometry and an accurate system for the segmentation of intracranial aneurysms. The study may be classified into two major parts: proposal of a new segmentation algorithm, the Threshold-based Level Set (TLS) for intracranial aneurysm and surrounding celebravascular structures, and validation of the TLS method via in-vivo and in-vitro experiments for clinical application.

In chapter 4 (Aim 1, 2 and 3), a new level set method for intracranial aneurysm segmentation was proposed. The details of the threshold-based level set segmentation method were explained, including the principle, formula, numerical scheme and parameter settings. We applied the TLS method to eight patient-specific aneurysm cases and compared the results of TLS segmentation with other segmentation approaches. From this, we found that various methods of segmentation were able to generate a range of geometric models with differences in shape and volume, the occurrence of uncertain results having the reductive potential to negatively affect clinical treatment decisions. Through

analysis of eight cerebral aneurysm models, this study indicated that the TLS method possessed the highest overlap rate in comparison to other methods, with an average of 91.59% with the minimum the volume difference. These results likewise indicate that the TLS method may be utilized in the segmentation of aneurysms with blurred boundaries and in inhomogeneous images. The TLS method has been proven to improve the accuracy of cerebrovascular aneurysm segmentation - a technique with the ability to segment aneurysms anatomically without the setting of a seed point or intensity threshold. This method is also suitable for the segmentation of complex cerebrovascular anatomical shapes.

In chapter 5 (aim 4 and 5), three dichotomous segmentation methods were introduced for the analysis of 45 cerebral aneurysm models in terms of geometric shape, volume, and haemodynamic results. The results of in-vivo validation showed that the TLS method appeared higher in terms of overlap ratio and smaller in terms of the volume difference when compared to the other methods across ICA, MCA, and AComA aneurysms. It also indicated that the volume differences and the overlap ratio of TLS may be controlled at a maximum of under 9% and a minimum of over 92% for all aneurysms respectively. Although based on the same medical imagery and data, different methods of image segmentation were found to generate alterations in shape and volume, thereby resulting in significantly differing haemodynamic results. To investigate the impact of segmentation results on patient specified analysis of haemodynamic simulation, computational haemodynamic simulation was performed via the use of three varying categories of segmentation methodology, alongside measurement of typical haemodynamic characteristics, including energy loss (EL) and wall shear stress (WSS). The results indicated that the difference in EL and greatest WSS appeared to be both relatively stable and subject to control by the influence of segmentation method. However, the results of the lowest WSS were seen to be significantly dependent upon the surface geometry of the aneurysm surface. It is

thereby essential to confirm the quality of segmentation processes, in order to optimise patient-specific analyses of cerebrovascular haemodynamics. We believe that a validation process to confirm the results of these segmentations, will be of vital importance in limiting the error arising from such manipulations of image data. With this, the results that are influenced by the segmentation process must be included in the haemodynamic study.

In chapter 6 (aim 6), a series of in-vitro experiments using CT scan, were conducted on silicone aneurysm models (SAM). In this, four different silicone models and four dilution rates of contrast agent were used to generate various image data sets for validation of our previously proposed TLS segmentation method. The TLS method was found to be able to achieve over 89% of the volume overlap rate and under 7% of the volume difference in all silicone model shapes with differeing degrees of complexity, and contrast agent dilutions. We compared TLS with Region Growing Threshold (RGT) and Chan-Vese model (CV) to investigate the influence of different methods on segmentation results. For various level of contrast agent, TLS vs. RGT (best) exhibited a reliability in overlap rate (JM) and maximum surface distance (HD), but no consistency in the volume difference. CV was seen to have a high JM and low mean absolute surface distance (MASD), though only under high contrast conditions. The study found the volume difference of the segmentation result to be highly dependent on the segmentation method. The TLS method was found to be a technique with the ability to automatically segment intracranial aneurysms without the setting of a seed point or intensity threshold, and is likewise available for the segmentation of modifiable anatomical shapes, with blurred boundaries and inhomogeneous images. It is thus a valuable tool for clinical diagnosis and surgical preparation, and will furthermore, play a vital role as an important tool for future haemodynamic research.

7.2 Future Work

7.2.1 Measurement of Geometrical Characterisation of Intracranial Aneurysms

Geometric indices (maximum diameter, neck diameter, height, aspect ratio, bottleneck factor, bulge location, volume, surface area) as defined on intracranial aneurysms, have been widely used in rupture risk assessment and surgical planning. However, most indices employed in clinical settings are currently evaluated on two dimensional images that inevitably fail to capture the three dimensional nature of complex aneurysmal shapes. In addition, they may suffer from poor inter and intra operator repeatability, since measurements are performed manually. The purpose of future work in this field, is thus to introduce objective and robust techniques for the 3D characterization of intracranial aneurysms, whilst preserving a close connection to the way aneurysms are currently characterized in clinical settings.

7.2.2 Medical Image Registration for Intracranial Aneurysms

Medical image registration is an important task in medical image processing. Image registration refers to the process of aligning data sets, which may be applied to images from the same subject acquired via the use of different modalities (e.g., CTA, MRA and DSA) or at different time points (e.g., follow-up scans). Image registration is able to be utilised in follow up patients with untreated intracranial aneurysms via the comparison of CTA images, taken at differing times, to analyse changes within the aneurysm. Image registration may also be used in the reconstruction of cerebral vessel models for patients with treated intracranial aneurysms, to avoid problems surrounding metal artifacts in CTA imaging . A large number of methods for image registration, ranging from simple

(e.g., rigid or affine transformations) to more complex transformations (e.g., deformable transforms) are described in the literature. However, no one method currently exhibits for all applications. The goal of future work in medical image registration is thus to find an optimum method for intracranial aneurysm registration.

Appendix A

Appendix Title

Paper 1: Image segmentation methods for intracranial aneurysm haemodynamic research

Paper 2: Investigation of Image Segmentation Methods for Intracranial Aneurysm Haemodynamic Research

Paper 3: Development of Image Segmentation Methods for Intracranial Aneurysms

Paper 4: A Comparison of Medical Image Segmentation Methods for Cerebral Aneurysm Computational Hemodynamics

An Ethics Approval Letter

Bibliography

[1] A. Osborn and J. Jacobs, *Diagnostic Cerebral Angiography.* Lippincott Williams & Wilkins, 1999.

[2] A. Keedy, "An overview of intracranial aneurysms," *Mcgill J Med*, vol. 9, no. 2, pp. 141–6, 2006.

[3] E. S. Connolly, A. A. Rabinstein, J. R. Carhuapoma, C. P. Derdeyn, J. Dion, R. T. Higashida, B. L. Hoh, C. J. Kirkness, A. M. Naidech, C. S. Ogilvy, A. B. Patel, B. G. Thompson, and P. Vespa, "Guidelines for the management of aneurysmal subarachnoid hemorrhage: A guideline for healthcare professionals from the american heart association/american stroke association," *Stroke*, vol. 43, no. 6, pp. 1711–1737, 2012.

[4] J. van Gijn and G. J. E. Rinkel, "Subarachnoid haemorrhage: diagnosis, causes and management," *Brain*, vol. 124, no. 2, pp. 249–278, 2001.

[5] J. E. Loewenstein, S. C. Gayle, E. J. Duffis, C. J. Prestigiacomo, and C. D. Gandhi, "The natural history and treatment options for unruptured intracranial aneurysms," *International Journal of Vascular Medicine*, vol. 2012, p. 11, 2012.

[6] M. Jensen, *Evaluation of the Cerebral Vessels: Endovascular Therapy.* Springer Milan, 2012, book section 5, pp. 27–36.

[7] Q. Zhang, R. Eagleson, and T. M. Peters, "Volume visualization: a technical overview with a focus on medical applications," *J Digit Imaging*, vol. 24, no. 4, pp. 640–64, 2011.

[8] R. A. Drebin, L. Carpenter, and P. Hanrahan, "Volume rendering," in *Proceedings of the 15th annual conference on Computer graphics and interactive techniques*. ACM, 1988, Conference Proceedings, pp. 65–74.

[9] M. Hadwiger, J. M. Kniss, C. Rezk-salama, D. Weiskopf, and K. Engel, *Real-time Volume Graphics*. A. K. Peters, Ltd., 2006.

[10] S. Parker, P. Shirley, Y. Livnat, C. Hansen, and P.-P. Sloan, "Interactive ray tracing for isosurface rendering," in *Proceedings of the conference on Visualization '98*. IEEE Computer Society Press, 1998, Conference Proceedings, pp. 233–238.

[11] M. K. Bosma, "Iso-surface volume rendering: speed and accuracy for medical applications," 2000.

[12] U. Tiede, K. H. Hoehne, M. Bomans, A. Pommert, M. Riemer, and G. Wiebecke, "Surface rendering," *IEEE Comput. Graph. Appl.*, vol. 10, no. 2, pp. 41–53, 1990.

[13] E. K. Fishman, D. R. Ney, D. G. Heath, F. M. Corl, K. M. Horton, and P. T. Johnson, "Volume rendering versus maximum intensity projection in ct angiography: What works best, when, and why," *RadioGraphics*, vol. 26, no. 3, pp. 905–922, 2006.

[14] S. Schreiner, C. B. Paschal, and R. L. Galloway, "Comparison of projection algorithms used for the construction of maximum intensity projection images," *J Comput Assist Tomogr*, vol. 20, no. 1, pp. 56–67, 1996.

[15] J. J. Choi, B.-S. Shin, Y. G. Shin, and K. Cleary, "Efficient volumetric ray casting for isosurface rendering," *Computers and Graphics*, vol. 24, no. 5, pp. 661–670, 2000.

[16] W. E. Lorensen and H. E. Cline, "Marching cubes: A high resolution 3d surface construction algorithm," *SIGGRAPH Comput. Graph.*, vol. 21, no. 4, pp. 163–169, 1987.

[17] A. Badry, R. Elshafey, and M. Khalil, "Detection, characterization and endovascular therapy planning of intracranial aneurysms with 16-channel multidetector row ct angiography," *Egyptian Journal of Radiology and Nuclear Medicine*, 2013.

[18] M. Groth, N. D. Forkert, J. H. Buhk, M. Schoenfeld, E. Goebell, and J. Fiehler, "Comparison of 3d computer-aided with manual cerebral aneurysm measurements in different imaging modalities," *Neuroradiology*, vol. 55, no. 2, pp. 171–8, 2013.

[19] H. Takao, Y. Murayama, T. Ishibashi, T. Saguchi, M. Ebara, H. Arakawa, K. Irie, K. Iwasaki, M. Umezu, and T. Abe, "Comparing accuracy of cerebral aneurysm size measurements from three routine investigations: computed tomography, magnetic resonance imaging, and digital subtraction angiography," *Neurol Med Chir (Tokyo)*, vol. 50, no. 10, pp. 893–9, 2010.

[20] S. Dhar, M. Tremmel, J. Mocco, M. Kim, J. Yamamoto, A. H. Siddiqui, L. N. Hopkins, and H. Meng, "Morphology parameters for intracranial aneurysm rupture risk assessment," *Neurosurgery*, vol. 63, no. 2, pp. 185–96; discussion 196–7, 2008.

[21] M. L. Raghavan, B. Ma, and R. E. Harbaugh, "Quantified aneurysm shape and rupture risk," *J Neurosurg*, vol. 102, no. 2, pp. 355–62, 2005.

[22] J. Xiang, S. K. Natarajan, M. Tremmel, D. Ma, J. Mocco, L. N. Hopkins, A. H. Siddiqui, E. I. Levy, and H. Meng, "Hemodynamic-morphologic discriminants for intracranial aneurysm rupture," *Stroke*, vol. 42, no. 1, pp. 144–52, 2011.

[23] C. W. Ryu, O. K. Kwon, J. S. Koh, and E. J. Kim, "Analysis of aneurysm rupture in relation to the geometric indices: aspect ratio, volume, and volume-to-neck ratio," *Neuroradiology*, vol. 53, no. 11, pp. 883–9, 2011.

[24] R. Yasuda, C. M. Strother, W. Taki, K. Shinki, K. Royalty, K. Pulfer, and C. Karmonik, "Aneurysm volume-to-ostium area ratio: a parameter useful for discriminating the rupture status of intracranial aneurysms," *Neurosurgery*, vol. 68, no. 2, pp. 310–7; discussion 317–8, 2011.

[25] T. Ries, K. Wegscheider, A. Wulff, K. Radelfahr, D. Saring, N. D. Forkert, and J. Fiehler, "Quantification of recurrence volumes after endovascular treatment of cerebral aneurysm as surrogate endpoint for treatment stability," *Neuroradiology*, vol. 53, no. 8, pp. 593–8, 2011.

[26] M. Groth, J. Fiehler, and N. D. Forkert, "Variability in visual assessment of cerebral aneurysms could be reduced by quantification of recurrence volumes," *AJNR Am J Neuroradiol*, vol. 32, no. 8, pp. E163–4; author reply E165, 2011.

[27] R. Cardenes, J. M. Pozo, H. Bogunovic, I. Larrabide, and A. F. Frangi, "Automatic aneurysm neck detection using surface voronoi diagrams," *IEEE Trans Med Imaging*, vol. 30, no. 10, pp. 1863–76, 2011.

[28] M. Piccinelli, D. A. Steinman, Y. Hoi, F. Tong, A. Veneziani, and L. Antiga, "Automatic neck plane detection and 3d geometric characterization of aneurysmal sacs," *Ann Biomed Eng*, vol. 40, no. 10, pp. 2188–211, 2012.

[29] I. Wanke, A. Doerfler, U. Dietrich, T. Egelhof, B. Schoch, D. Stolke, and M. Forsting, "Endovascular treatment of unruptured intracranial aneurysms," *AJNR Am J Neuroradiol*, vol. 23, no. 5, pp. 756–61, 2002.

[30] A. Doerfler, I. Wanke, S. L. Goericke, H. Wiedemayer, T. Engelhorn, E. R. Gizewski, D. Stolke, and M. Forsting, "Endovascular treatment of middle cerebral artery aneurysms with electrolytically detachable coils," *AJNR Am J Neuroradiol*, vol. 27, no. 3, pp. 513–20, 2006.

[31] A. Lauric, E. L. Miller, M. I. Baharoglu, and A. M. Malek, "3d shape analysis of intracranial aneurysms using the writhe number as a discriminant for rupture," *Annals of Biomedical Engineering*, vol. 39, no. 5, pp. 1457–1469, 2011.

[32] D. A. Orringer, A. Golby, and F. Jolesz, "Neuronavigation in the surgical management of brain tumors: current and future trends," *Expert Rev Med Devices*, vol. 9, no. 5, pp. 491–500, 2012.

[33] P. Marinho, L. Thines, L. Verscheure, S. Mordon, J. P. Lejeune, and M. Vermandel, "Recent advances in cerebrovascular simulation and neuronavigation for the optimization of intracranial aneurysm clipping," *Comput Aided Surg*, vol. 17, no. 2, pp. 47–55, 2012.

[34] J. N. Bruneton, "Spiral and multislice computed tomography of the body," *Clinical imaging*, vol. 27, no. 5, pp. 365–365, 2003.

[35] W. S. Moore and J. C. Jimenez, *A handbook of vascular disease management.* Singapore: World Scientific, 2011.

[36] M. Prokop and M. Galanski, *Spiral and multislice computed tomography of the body.* Stuttgart ; New York: Thieme, 2003.

[37] M. R. Harrigan and J. P. Deveikis, *Handbook of cerebrovascular disease and neurointerventional technique*, second edition. ed. Dordecht ;: Humana Press, 2013.

[38] K. Klingenbeck-Regn, S. Schaller, T. Flohr, B. Ohnesorge, A. F. Kopp, and U. Baum, "Subsecond multi-slice computed tomography: basics and applications," *European Journal of Radiology*, vol. 31, no. 2, pp. 110–124, 1999.

[39] L. W. Goldman, "Principles of ct and ct technology," *J Nucl Med Technol*, vol. 35, no. 3, pp. 115–28; quiz 129–30, 2007.

[40] R. Gupta, A. C. Cheung, S. H. Bartling, J. Lisauskas, M. Grasruck, C. Leidecker, B. Schmidt, T. Flohr, and T. J. Brady, "Flat-panel volume ct: fundamental principles, technology, and applications," *Radiographics*, vol. 28, no. 7, pp. 2009–22, 2008.

[41] H. J. Otero, M. L. Steigner, and F. J. Rybicki, "The "post-64" era of coronary ct angiography: understanding new technology from physical principles," *Radiol Clin North Am*, vol. 47, no. 1, pp. 79–90, 2009.

[42] J. F. Barrett and N. Keat, "Artifacts in ct: recognition and avoidance," *Radiographics*, vol. 24, no. 6, pp. 1679–91, 2004.

[43] S. Karimi, P. Cosman, C. Wald, and H. Martz, "Segmentation of artifacts and anatomy in ct metal artifact reduction," *Med Phys*, vol. 39, no. 10, pp. 5857–68, 2012.

[44] S. Radzi, G. Cowin, M. Robinson, J. Pratap, A. Volp, M. A. Schuetz, and B. Schmutz, "Metal artifacts from titanium and steel screws in ct, 1.5t and 3t mr images of the tibial pilon: a quantitative assessment in 3d," *Quant Imaging Med Surg*, vol. 4, no. 3, pp. 163–72, 2014.

[45] J. P. Villablanca, N. Martin, R. Jahan, Y. P. Gobin, Frazee, G. Duckwiler, J. Bentson, M. Hardart, D. Coiteiro, J. Sayre, and F. Vinuela, "Volume-rendered

helical computerized tomography angiography in the detection and characterization of intracranial aneurysms," *J Neurosurg*, vol. 93, no. 2, pp. 254–64, 2000.

[46] E. T. Chappell, F. C. Moure, and M. C. Good, "Comparison of computed tomographic angiography with digital subtraction angiography in the diagnosis of cerebral aneurysms: a meta-analysis," *Neurosurgery*, vol. 52, no. 3, pp. 624–31; discussion 630–1, 2003.

[47] J. E. Siebert, J. R. Pernicone, and E. J. Potchen, "Physical principles and application of magnetic resonance angiography," *Semin Ultrasound CT MR*, vol. 13, no. 4, pp. 227–45, 1992.

[48] D. Chien and R. R. Edelman, "Basic principles and clinical applications of magnetic resonance angiography," *Semin Roentgenol*, vol. 27, no. 1, pp. 53–62, 1992.

[49] R. R. Edelman, "Basic principles of magnetic resonance angiography," *Cardiovasc Intervent Radiol*, vol. 15, no. 1, pp. 3–13, 1992.

[50] B. M. Tress and P. M. Desmond, "Magnetic resonance angiography. i. basic principles," *Australas Radiol*, vol. 37, no. 3, pp. 236–8, 1993.

[51] r. Huston, J., D. A. Nichols, P. H. Luetmer, J. T. Goodwin, F. B. Meyer, D. O. Wiebers, and A. L. Weaver, "Blinded prospective evaluation of sensitivity of mr angiography to known intracranial aneurysms: importance of aneurysm size," *AJNR Am J Neuroradiol*, vol. 15, no. 9, pp. 1607–14, 1994.

[52] Z. Watanabe, Y. Kikuchi, K. Izaki, N. Hanyu, F. S. Lim, H. Gotou, J. Koizumi, T. Gotou, M. Kowada, and K. Watanabe, "The usefulness of 3d mr angiography in surgery for ruptured cerebral aneurysms," *Surg Neurol*, vol. 55, no. 6, pp. 359–64, 2001.

[53] W. M. Adams, R. D. Laitt, and A. Jackson, "The role of mr angiography in the pretreatment assessment of intracranial aneurysms: a comparative study," *AJNR Am J Neuroradiol*, vol. 21, no. 9, pp. 1618–28, 2000.

[54] M. Okahara, H. Kiyosue, M. Yamashita, H. Nagatomi, H. Hata, T. Saginoya, Y. Sagara, and H. Mori, "Diagnostic accuracy of magnetic resonance angiography for cerebral aneurysms in correlation with 3d-digital subtraction angiographic images: a study of 133 aneurysms," *Stroke*, vol. 33, no. 7, pp. 1803–8, 2002.

[55] P. Brugieres, J. Blustajn, C. Le Guerinel, J. F. Meder, P. Thomas, and A. Gaston, "Magnetic resonance angiography of giant intracranial aneurysms," *Neuroradiology*, vol. 40, no. 2, pp. 96–102, 1998.

[56] O. De Jesus and N. Rifkinson, "Magnetic resonance angiography of giant aneurysms. pitfalls and surgical implications," *P R Health Sci J*, vol. 16, no. 2, pp. 131–5, 1997.

[57] T. Metens, F. Rio, D. Baleriaux, T. Roger, P. David, and G. Rodesch, "Intracranial aneurysms: detection with gadolinium-enhanced dynamic three-dimensional mr angiography-initial results," *Radiology*, vol. 216, no. 1, pp. 39–46, 2000.

[58] H. R. Jager, H. Ellamushi, E. A. Moore, J. P. Grieve, N. D. Kitchen, and W. J. Taylor, "Contrast-enhanced mr angiography of intracranial giant aneurysms," *AJNR Am J Neuroradiol*, vol. 21, no. 10, pp. 1900–7, 2000.

[59] W. A. Willinek, J. Gieseke, M. von Falkenhausen, M. Born, D. Hadizadeh, C. Manka, H. J. Textor, H. H. Schild, and C. K. Kuhl, "Sensitivity encoding (sense) for high spatial resolution time-of-flight mr angiography of the intracranial arteries at 3.0 t," *Rofo*, vol. 176, no. 1, pp. 21–6, 2004.

[60] D. Y. Yoon, K. J. Lim, C. S. Choi, B. M. Cho, S. M. Oh, and S. K. Chang, "Detection and characterization of intracranial aneurysms with 16-channel multidetector row

ct angiography: a prospective comparison of volume-rendered images and digital subtraction angiography," *AJNR Am J Neuroradiol*, vol. 28, no. 1, pp. 60–7, 2007.

[61] D. P. Harrington, L. M. Boxt, and P. D. Murray, "Digital subtraction angiography: overview of technical principles," *American Journal of Roentgenology*, vol. 139, no. 4, pp. 781–786, 1982.

[62] M. Castillo, *Digital Subtraction Angiography (DSA): Basic Principles.* John Wiley and Sons, Ltd, 2014, pp. 207–220.

[63] J. Menke, J. Larsen, and K. Kallenberg, "Diagnosing cerebral aneurysms by computed tomographic angiography: meta-analysis," *Ann Neurol*, vol. 69, no. 4, pp. 646–54, 2011.

[64] C. J. Prestigiacomo, A. Sabit, W. He, P. Jethwa, C. Gandhi, and J. Russin, "Three dimensional ct angiography versus digital subtraction angiography in the detection of intracranial aneurysms in subarachnoid hemorrhage," *J Neurointerv Surg*, vol. 2, no. 4, pp. 385–9, 2010.

[65] J. B. Bederson and J. B. Bederson, "Guidelines for the management of aneurysmal subarachnoid hemorrhage: A statement for healthcare professionals from a special writing group of the stroke council, american heart association," *Stroke (1970)*, vol. 40, no. 3, pp. 994–1025, 2009.

[66] M. Larobina and L. Murino, "Medical image file formats," *Journal of Digital Imaging*, vol. 27, no. 2, pp. 200–206, 2014.

[67] r. Wiggins, R. H., H. C. Davidson, H. R. Harnsberger, J. R. Lauman, and P. A. Goede, "Image file formats: past, present, and future," *Radiographics*, vol. 21, no. 3, pp. 789–98, 2001.

[68] O. S. Pianykh, *Digital imaging and communications in medicine (DICOM) : a practical introduction and survival guide*, 2nd ed. Heidelberg ; New York: Springer, 2012.

[69] M. Kass, A. Witkin, and D. Terzopoulos, "Snakes: Active contour models," *International Journal of Computer Vision*, vol. 1, pp. 321–331, 1988.

[70] V. Caselles, F. Catt, T. Coll, and F. Dibos, "A geometric model for active contours in image processing," *Numerische Mathematik*, vol. 66, no. 1, pp. 1–31, 1993.

[71] R. Malladi, J. A. Sethian, and B. C. Vemuri, "Shape modeling with front propagation: a level set approach," *Pattern Analysis and Machine Intelligence, IEEE Transactions on*, vol. 17, no. 2, pp. 158–175, 1995.

[72] S. Osher and J. A. Sethian, "Fronts propagating with curvature-dependent speed: Algorithms based on hamilton-jacobi formulations," *Journal of Computational Physics*, vol. vol 79, pp. 12–49, 1988.

[73] V. Caselles, R. Kimmel, and G. Sapiro, "Geodesic active contours," *International Journal of Computer Vision*, vol. 22, no. 1, pp. 61–79, 1997.

[74] S. Kichenassamy, A. Kumar, P. Olver, A. Tannenbaum, and A. Yezzi, "Gradient flows and geometric active contour models," in *Computer Vision, 1995. Proceedings., Fifth International Conference on*, 1995, Conference Proceedings, pp. 810–815.

[75] T. F. Chan and L. A. Vese, "Active contours without edges," *IEEE TRANSACTIONS ON IMAGE PROCESSING*, vol. vol. 10, no. 2, pp. 266–277, 2001.

[76] R. Kimmel, *Fast Edge Integration*. Springer New York, 2003, book section 4, pp. 59–77.

[77] L. Jundong, "Robust image segmentation using local median," in *Computer and Robot Vision, 2006. The 3rd Canadian Conference on*, 2006, Conference Proceedings, pp. 31–31.

[78] Y. Sen, Y. Qian, A. Avolio, and M. Morgan, "Development of image segmentation methods for intracranial aneurysms," *Comput Math Methods Med*, vol. 2013, p. 715325, 2013.

[79] N. D. Forkert, A. Schmidt-Richberg, J. Fiehler, T. Illies, D. Moller, H. Handels, and D. Saring, "Fuzzy-based vascular structure enhancement in time-of-flight mra images for improved segmentation," *Methods Inf Med*, vol. 50, no. 1, pp. 74–83, 2011.

[80] B. E. Chapman, J. O. Stapelton, and D. L. Parker, "Intracranial vessel segmentation from time-of-flight mra using pre-processing of the mip z-buffer: accuracy of the zbs algorithm," *Medical image analysis*, vol. 8, no. 2, pp. 113–26, 2004.

[81] P. A. Yushkevich, J. Piven, H. C. Hazlett, R. G. Smith, S. Ho, J. C. Gee, and G. Gerig, "User-guided 3d active contour segmentation of anatomical structures: significantly improved efficiency and reliability," *NeuroImage*, vol. 31, no. 3, pp. 1116–28, 2006.

[82] M. Droske, B. Meyer, M. Rumpf, and C. Schaller, "An adaptive level set method for medical image segmentation," in *Information Processing in Medical Imaging*, ser. Lecture Notes in Computer Science, M. Insana and R. Leahy, Eds. Springer Berlin Heidelberg, 2001, vol. 2082, pp. 416–422.

[83] M. E. Leventon, W. E. L. Grimson, and O. Faugeras, "Statistical shape influence in geodesic active contours," *Proceedings of the IEEE Computer Society Conference on Computer Vision and Pattern Recognition*, vol. 1, pp. 316–323, 2000.

[84] J. A. Sethian, *Level Set Methods and Fast Marching Methods: Evolving Interfaces in Computational Geometry, Fluid Mechanics, Computer Vision, and Materials Science.* Cambridge University Press, 1999.

[85] S. Demirci, G. Lejeune, and N. Navab, "Hybird deformable model for aneurysm segmentation," in *Biomedical Imaging: From Nano to Macro, 2009.*, 2009, Conference Proceedings, pp. 33– 36.

[86] N. Wilson, K. Wang, R. W. Dutton, and C. Taylor, "A software framework for creating patient specific geometric models from medical imaging data for simulation based medical planning of vascular surgery," in *MICCAI '01 Proceedings of the 4th International Conference on Medical Image Computing and Computer-Assisted Intervention*, 2001, Conference Proceedings, pp. 449–456.

[87] M. W. Law and A. C. Chung, "Vessel and intracranial aneurysm segmentation using multi-range filters and local variances," *MICCAI*, vol. 10(Pt 1), pp. 866–874, 2007.

[88] M. Hernandez and A. F. Frangi, "Non-parametric geodesic active regions: method and evaluation for cerebral aneurysms segmentation in 3dra and cta," *Medical image analysis*, vol. 11, no. 3, pp. 224–41, 2007.

[89] R. Manniesing, B. K. Velthuis, M. S. van Leeuwen, I. C. van der Schaaf, P. J. van Laar, and W. J. Niessen, "Level set based cerebral vasculature segmentation and diameter quantification in ct angiography," *Medical image analysis*, vol. 10, no. 2, pp. 200–14, 2006.

[90] T. Deschamps, P. Schwartz, D. Trebotich, P. Colella, D. Saloner, and R. Malladi, "Vessel segmentation and blood flow simulation using level-sets and embedded boundary methods," *International Congress Series*, vol. 1268, pp. 75–80, 2004.

[91] A. Firouzian, R. Manniesing, Z. H. Flach, R. Risselada, F. van Kooten, M. C. Sturkenboom, A. van der Lugt, and W. J. Niessen, "Intracranial aneurysm segmentation in 3d ct angiography: method and quantitative validation with and without prior noise filtering," *Eur J Radiol*, vol. 79, no. 2, pp. 299–304, 2011.

[92] T. Zuva, O. O. Olugbara, S. O. Ojo, and S. M. Ngwira, "Image segmentation, availabletechniques, developments and open issues," *Canadian Journal on Image Processing and Computer Vision*, vol. Vol. 2 No. 3, pp. 20–29, 2011.

[93] D. Lesage, E. D. Angelini, I. Bloch, and G. Funka-Lea, "A review of 3d vessel lumen segmentation techniques: models, features and extraction schemes," *Medical image analysis*, vol. 13, no. 6, pp. 819–45, 2009.

[94] H. Zhang, J. E. Fritts, and S. A. Goldman, "Image segmentation evaluation: A survey of unsupervised methods," *Computer Vision and Image Understanding*, vol. 110, no. 2, pp. 260–280, 2008.

[95] Y. Sen, Y. Qian, Y. Zhang, and M. Morgan, "A comparison of medical image segmentation methods for cerebral aneurysm computational hemodynamics," in *2011 4th International Conference on Biomedical Engineering and Informatics*, vol. 2, 2011, Conference Proceedings, pp. 901–904.

[96] J. Weickert, B. H. Romeny, and M. A. Viergever, "Efficient and reliable schemes for nonlinear diffusion filtering," *IEEE Trans Image Process*, vol. 7, no. 3, pp. 398–410, 1998.

[97] R. Goldenberg, R. Kimmel, E. Rivlin, and M. Rudzsky, "Fast geodesic active contours," *IEEE Trans Image Process*, vol. 10, no. 10, pp. 1467–75, 2001.

[98] J. Russell and R. Cohn, *Chebyshev's inequality*. Book on Demand Ltd, 2012.

[99] P. T. Truc, T. S. Kim, S. Lee, and Y. K. Lee, "A study on the feasibility of active contours on automatic ct bone segmentation," *J Digit Imaging*, vol. 23, no. 6, pp. 793–805, 2010.

[100] M. H. Vlak, G. J. Rinkel, P. Greebe, J. G. van der Bom, and A. Algra, "Trigger factors and their attributable risk for rupture of intracranial aneurysms: A case-crossover study," *Stroke*, vol. 42, pp. 1878–1882, 2011.

[101] L. Jonathan, J. K. Song, and D. W. Newell, "Cerebral aneurysms," *N Engl J Med*, vol. 355, pp. 928–939, 2006.

[102] N. de Rooij, F. Linn, J. van der Plas, A. Algra, and G. Rinkel, "Incidence of subarachnoid haemorrhage: a systematic review with emphasis on region, age, gender and time trends," *Journal of neurology, neurosurgery, and psychiatry*, vol. 78(12), pp. 1365–1372, 2007.

[103] L. H. Phillips II, J. P. Whisnant, W. Michael O'Fallon, and T. M. Sundt Jr., "The unchanging pattern of subarachnoid hemorrhage in a community," *Neurology*, vol. 30, pp. 1034–1040, 1980.

[104] M. J. H. Wermer, I. C. van der Schaaf, A. Algra, and G. J. E. Rinkel, "Risk of rupture of unruptured intracranial aneurysms in relation to patient and aneurysm characteristics: an updated meta-analysis." *Stroke*, vol. 38(4), pp. 1404–1410, 2007.

[105] N. F. Kassell, J. C. Torner, E. C. Haley, J. A. Jane, Jr, H. P. Adams, and G. L. Kongable, "The international cooperative study on the timing of aneurysm surgery. part 1: Overall management results," *J Neurosurg*, vol. 73(1), pp. 18–36, 1990.

[106] Y. Qian, H. Takao, M. Umezu, and Y. Murayama, "Risk analysis of unruptured aneurysms using computed fluid dynamics technology: Preliminary results," *AJNR Am J Neuroradiol*, vol. 32(10), pp. 1948–55, 2011.

[107] M. A. Castro, C. M. Putman, and J. R. Cebral, "Computational modeling of cerebral aneurysms in arterial networks reconstructed from multiple 3d rotational angiography images," *Proceedings of SPIE*, pp. 233–244, 2005.

[108] D. A. Steinman, J. S. Milner, C. J. Norley, S. P. Lownie, and D. W. Holdsworth, "Image-based computational simulation of flow dynamics in a giant intracranial aneurysm," *AJNR Am J Neuroradiol*, vol. 24(4), pp. 559–566, 2003.

[109] T. Hassan, E. V. Timofeev, M. Ezura, T. Saito, A. Takahashi, K. Takayama, and T. Yoshimoto, "Hemodynamic analysis of an adult vein of galen aneurysm malformation by use of 3d image-based computational fluid dynamics," *AJNR Am J Neuroradiol*, vol. 24(6), pp. 1075–1082, 2003.

[110] B. Ma, R. E. Harbaugh, and M. L. Raghavan, "Three-dimensional geometrical characterization of cerebral aneurysms," *Annals of Biomedical Engineering*, vol. 32, no. 2, pp. 264–73, 2004.

[111] H. Zakaria, A. M. Robertson, and C. W. Kerber, "A parametric model for studies of flow in arterial bifurcations," *Ann Biomed Eng*, vol. 36, no. 9, pp. 1515–30, 2008.

[112] T. Hassan, E. V. Timofeev, T. Saito, H. Shimizu, M. Ezura, Y. Matsumoto, K. Takayama, T. Tominaga, and A. Takahashi, "A proposed parent vessel geometry-based categorization of saccular intracranial aneurysms: computational flow dynamics analysis of the risk factors for lesion rupture," *J Neurosurg*, vol. 103, no. 4, pp. 662–80, 2005.

[113] T.-M. Liou, T.-W. Chang, and W.-C. Chang, "Pulsatile flow through a bifurcation with a cerebrovascular aneurysm," *Journal of Biomechanical Engineering*, vol. 116, no. 1, pp. 112–118, 1994.

[114] H. J. Steiger, A. Poll, D. Liepsch, and H. J. Reulen, "Basic flow structure in saccular aneurysms: a flow visualization study," *Heart Vessels*, vol. 3, no. 2, pp. 55–65, 1987.

[115] M. Shojima, M. Oshima, K. Takagi, R. Torii, M. Hayakawa, K. Katada, A. Morita, and T. Kirino, "Magnitude and role of wall shear stress on cerebral aneurysm: computational fluid dynamic study of 20 middle cerebral artery aneurysms," *Stroke; a journal of cerebral circulation*, vol. 35, no. 11, pp. 2500–5, 2004.

[116] J. R. Cebral, M. A. Castro, J. E. Burgess, R. S. Pergolizzi, M. J. Sheridan, and C. M. Putman, "Characterization of cerebral aneurysmas for assessing risk of rupture by using patient-specific computational hemodynamics models," *AJNR Am J Neuroradiol*, vol. 26(10), pp. 2550–2559, 2005.

[117] L. Goubergrits, J. Schaller, U. Kertzscher, N. van den Bruck, K. Poethkow, C. Petz, H. C. Hege, and A. Spuler, "Statistical wall shear stress maps of ruptured and unruptured middle cerebral artery aneurysms," *J R Soc Interface*, vol. 9, no. 69, pp. 677–88, 2012.

[118] J. R. Cebral, F. Mut, J. Weir, and C. Putman, "Quantitative characterization of the hemodynamic environment in ruptured and unruptured brain aneurysms," *AJNR Am J Neuroradiol*, vol. 32, no. 1, pp. 145–51, 2011.

[119] L. D. Jou, D. H. Lee, H. Morsi, and M. E. Mawad, "Wall shear stress on ruptured and unruptured intracranial aneurysms at the internal carotid artery," *AJNR Am J Neuroradiol*, vol. 29, no. 9, pp. 1761–7, 2008.

[120] J. B. Thomas, J. S. Milner, B. K. Rutt, and D. A. Steinman, "Reproducibility of image-based computational fluid dynamics models of the human carotid bifurcation," *Annals of Biomedical Engineering*, vol. 31, no. 2, pp. 132–141, 2003.

[121] M. D. Ford, N. Alperin, S. H. Lee, D. W. Holdsworth, and D. A. Steinman, "Characterization of volumetric flow rate waveformes in the normal internal carotid and vertebral arteries," *Physiol Meas*, vol. 26(4), pp. 477–488, 2005.

[122] C. Karmonik, R. Klucznik, and G. Benndorf, "Comparison of velocity patterns in an acoma aneurysm measured with 2d phase contrast mri and simulated with cfd," *Technology and health care : official journal of the European Society for Engineering and Medicine*, vol. 16, no. 2, pp. 119–28, 2008.

[123] J. R. Cebral, M. Sheridan, and C. M. Putman, "Hemodynamics and bleb formation in intracranial aneurysms," *AJNR. American journal of neuroradiology*, vol. 31, no. 2, pp. 304–10, 2010.

[124] G. Hu and Mageras, *Survey of Recent Volumetric Medical Image Segmentation Techniques*. InTech, 2009.

[125] H. H. Chang, G. R. Duckwiler, D. J. Valentine, and W. C. Chu, "Computer-assisted extraction of intracranial aneurysms on 3d rotational angiograms for computational fluid dynamics modeling," *Med Phys*, vol. 36, no. 12, pp. 5612–21, 2009.

[126] P. Venugopal, D. Valentino, H. Schmitt, J. P. Villablanca, F. Vinuela, and G. Duckwiler, "Sensitivity of patient-specific numerical simulation of cerebal aneurysm hemodynamics to inflow boundary conditions," *J Neurosurg*, vol. 106, no. 6, pp. 1051–60, 2007.

[127] M. A. Castro, C. M. Putman, and J. R. Cebral, "Computational fluid dynamics modeling of intracranial aneurysms: effects of parent artery segmentation on intraaneurysmal hemodynamics," *AJNR Am J Neuroradiol*, vol. 27, no. 8, pp. 1703–9, 2006.

[128] T. Boskamp, D. Rinck, F. Link, B. Kummerlen, G. Stamm, and P. Mildenberger, "New vessel analysis tool for morphometric quantification and visualization of vessels in ct and mr imaging data sets," *Radiographics*, vol. 24, no. 1, pp. 287–97, 2004.

[129] M. Spiegel, T. Redel, T. Struffert, J. Hornegger, and A. Doerfler, "A 2d driven 3d vessel segmentation algorithm for 3d digital subtraction angiography data," *Phys Med Biol*, vol. 56, no. 19, pp. 6401–19, 2011.

[130] A. Popovic, M. de la Fuente, M. Engelhardt, and K. Radermacher, "Statistical validation metric for accuracy assessment in medical image segmentation," *International Journal of Computer Assisted Radiology and Surgery*, vol. 2, no. 3-4, pp. 169–181, 2007.

[131] L. Costaridou, *Medical image analysis methods*, ser. Electrical engineering and applied signal processing series. Boca Raton: CRC Press Taylor and Francis, 2005.

[132] H. Bogunovic, J. M. Pozo, M. C. Villa-Uriol, C. B. Majoie, R. van den Berg, H. A. Gratama van Andel, J. M. Macho, J. Blasco, L. S. Roman, and A. F. Frangi, "Automated segmentation of cerebral vasculature with aneurysms in 3dra and tof-mra using geodesic active regions: an evaluation study," *Med Phys*, vol. 38, no. 1, pp. 210–22, 2011.

[133] R. Ebel, "Estimation of the reliability of ratings," *Psychometrika*, vol. 16, no. 4, pp. 407–424, 1951.

Journal of Biomechanics ∎ (∎∎∎∎) ∎∎∎–∎∎∎

Contents lists available at ScienceDirect

Journal of Biomechanics

journal homepage: www.elsevier.com/locate/jbiomech
www.JBiomech.com

Image segmentation methods for intracranial aneurysm haemodynamic research

Yuka Sen *, Yi Qian, Alberto Avolio, Michael Morgan

The Australian School of Advanced Medicine, Macquarie University, 2 Technology Place, Sydney, NSW 2109, Australia

ARTICLE INFO

Article history:
Accepted 30 December 2013

Keywords:
Medical image segmentation
Intracranial aneurysm
Level set
Region growing threshold
Haemodynamics
Brain

ABSTRACT

Patient-specific haemodynamic technology is being increasingly utilised in clinical applications. Under normal circumstances, computational haemodynamic simulation is performed using geometric results obtained via medical image segmentation. However, even when employed upon the same set of medical imaging data, both the geometry and volume of intracranial aneurysm models are highly dependent upon varying insufficiently validated vascular segmentation methods. In this study, we compared three segmentation methods to segment the geometry of the aneurysm. These include: the Region Growing Threshold (RGT), Chan-Vese model (CV) and Threshold-Based Level Set (TLS). The results obtained were evaluated via measurement of arterial volume differences (VD), local geometric shapes, and haemodynamic simulation results. In total, 45 patient-specific aneurysm cases with three different anatomy locations were assessed in this study. From this, we discovered that the average VD of all three segmentation methods lay in the vicinity of 9.3% (SD= ±4.6%). The computational haemodynamic simulation was performed via the use of the vessel geometries. Analyses produced an average of 23.2% (SD= ±8.7%) difference in energy loss (EL) between the varying segmentation methods, with the difference in Wall Shear Stress (WSS) averaging 24.0% (SD= ±8.5%) and 126.4% (SD= ±124.4%) for the highest and lowest volumes of WSS respectively. The results of the lowest WSS, was seen to be significantly dependent upon the geometry of the aneurysm surface. It is therefore essential, in order to confirm the quality of segmentation processes in the application of patient-specific analyses of cerebrovascular haemodynamics – to validate these individual segmentation methods.

1. Introduction

Intracranial aneurysm (IA) ruptures are a much studied topic, with reports indicating the presence of un-ruptured IAs in approximately 5% of the adult population (Jonathan et al., 2006; Vlak et al., 2011). Although the rupture rate of IAs is low (de Rooij et al., 2007), rupture is associated with a high mortality and disability rate (Phillips II et al., 1980). Current treatments for IAs also carry a risk of death and disability. Therefore, identifying those IAs unlikely to rupture and avoiding treatment of these, is of great importance in minimising the side-effects and consequences of IAs (Kassell et al., 1990; Wermer et al., 2007).

CTA is widely applied in neurovascular imaging as a non-invasive diagnostic tool for the detection and evaluation of IAs. This makes it possible to visualise three dimensional (3D) aneurysms, allowing the reconstruction of patient specific vessels. Currently, the 3D blood vessel geometry has been applied in the performance of haemodynamic simulations, with the results subsequently utilised as an intelligent tool for both diagnosis and support of IA treatment. Computational fluid dynamics (CFD) technology has since been applied to calculate blood pressure, velocity, Wall Shear Stress (WSS), and energy loss (EL) – parameters that are difficult to obtain via direct measurement (Qian et al., 2011). These haemodynamic parameters have provided useful information in support of vascular surgeons in disease diagnoses and surgical preparation. Moreover, reconstruction of vascular structure from patient specific 3D angiography was used extensively to explain IA formation, development and rupture (Castro et al., 2005; Hassan et al., 2003; Steinman et al., 2003). As such, various types of IA morphology simulation have since become the mainstay method for assessing the role of morphology in predicting the risk of rupture (Ma et al., 2004; Raghavan et al., 2005). A number of studies focusing upon the effect of various hemodynamic parameters, including WSS, have addressed the impact of high WSS upon the initiation of IA formation and low WSS on both the growth and rupture of IAs (Cebral et al., 2005; Shojima et al., 2004). Moreover, Meng et al. (2013) have provided reviews to draw similar conclusions about the influence of high and low WSS upon IA growth and rupture.

The accuracy of CFD simulation is highly dependent upon vessel geometry (Thomas et al., 2003) with methods of medical image segmentation directly influencing the accuracy of IA model

* Corresponding author. Tel: +61 2 9812 3545; fax: +61 9812 3600.
E-mail address: yi.qian@mq.edu.au (Y. Sen).

0021-9290/$ - see front matter © 2014 Elsevier Ltd. All rights reserved.
http://dx.doi.org/10.1016/j.jbiomech.2013.12.035

construction, particularly in regards to vessel shape and volumes. Despite the many methods available, each with varying approaches and algorithms, there are currently no dominant segmentation methods, in terms of effectiveness, across all areas (Lesage et al., 2009; Zhang et al., 2008; Zuva et al., 2011). A previous study has indicated that the volume of the IA models exhibit variances across different segmentation methods, with the technique likewise influencing the local geometric shapes of the IAs modelled (Sen et al., 2011). Validation and verification processes for such methods will thus be an essential practice, allowing for the comparison of segmentation methods and adjustments of the parameters of these segmentation techniques in order to confirm the quality of patient-specific cerebral-vascular haemodynamic analysis. Moreover, though a number of commercial segmentation software packages have since been released to the market, there is a current lack of methodological discussion and information regarding validation processes.

In this paper, 45 IA patients, including vascular and IA CTA imagery across three locations: the internal carotid artery (ICA), middle cerebral artery (MCA) and anterior communicating artery (AComA), were used for analysis. Three segmentation methods: the Region Growing Threshold (RGT), Chan-Vese model (CV) (Chan and Vese, 2001), and the Threshold-Based Level Set (TLS) (Sen et al., 2013) were applied to segment data from these images. Subsequent comparisons of differences were then drawn, utilising calculations made using the above three segmentation methods, with CFD simulations performed in order to compare their respective influences upon haemodynamics parameters.

2. Materials and methods

2.1. Patient data

Forty-five patients with IAs were selected from patient databases at Macquarie University Hospital. 15 ICA, 15 MCA, and 15 AComA IA patients. 3D –CTA (GE) were performed on all patients, with cross-sectional images acquired via a CTA scanner under the same protocols. IA images were rendered in 512×512 pixel field, whilst slices of continuous thickness were used to segment and reconstruct 3D vascular geometry. Pixels were expressed in Hounsfield Units (HU), with the CTA imaging carried out for the period spanning 2008–2012. IA sizes ranged between 4 and 10 mm.

Clinical studies were performed with the consent of the patient in relation to the acquisition of IA images. These protocols were approved of by both the local institutional review board and regional research ethics committees.

2.2. Experiment setting

For quantitative evaluation, manual segmentation of 45 IAs using open source software [3D slicer (http://www.slicer.org)] was conducted by an experienced radiologist. The results were utilised as a ground truth (GT) for the comparison of other methods. A region of interest (ROI), a good representation of the targeted region for segmentation, was selected depending upon IA size.

2.3. Segmentation methods and parameter setting

2.3.1. Region growing threshold connecting (RGT)

The RGT method is initiated from a seed(s), selected within the area of the object to be segmented. This method requires two intensity values for the pixel of the object, with both a low threshold and high threshold value. Problems surrounding RGT include threshold selection and sensitivity to seed position (Hu, 2009).

2.3.2. Chan-Vese model (CV)

The CV model is based on the Mumford-Shah functional (Mumford and Shah, 1989). In the CV model, there is no utilisation of a term related to the image gradient. Instead, region intensity information is utilised for the target objects of segmentation. This model has exhibited a significantly effective performance in the segmentation of images with blurred boundaries.

2.3.3. Threshold-based level set (TLS)

The TLS method combines the geodesic active contour and the CV model together within the level set framework (Sen et al., 2013).

Under the level set scheme, the contour deforms by the function; $\frac{\partial \Gamma(t)}{\partial t} + F|\nabla\varphi| = 0$, with an embedded surface $\Gamma(t)$ represented as the zero level set of φ by $\Gamma(t) = \{x, y \in R | \varphi(x, y, t) = 0$. F is a function of speed, driving the $\Gamma(t)$ surface evolution in the normal direction. It is clear that F has a direct impact upon the quality of medical image segmentation. The associated evolution equation in the level set framework is as follows:

$$\frac{\partial \varphi}{\partial t} = |\nabla\varphi| \left[\alpha(I - T) + \beta div\left(g \frac{\nabla\varphi}{|\nabla\varphi|}\right)\right] \quad (1)$$

where I represents the image to be segmented, T represents the intensity threshold, g represents the image gradient (Sen et al., 2013). $\kappa = div\left(\frac{\nabla\varphi}{|\nabla\varphi|}\right)$ represents the curvature, α the image propagation constant and β the spatial modifier constant for the curvature κ. Both α and β weight the relative influence of each of these terms on the movement of the surface contour.

According to the theory of confidence intervals, the lower bound threshold of the IA can be defined by:

$$T_i = \mu_a - k_i \sigma_a \quad i \geq 0 \quad (2)$$

The threshold T is the difference between the mean of the contour of the IA (μ_a) and k times its standard deviation (σ_a). The intensities of the IA and its background regions are different. The lowest intensity threshold of the IA is the same as the highest intensity threshold of the background. Thus, $\mu_b + \kappa_b \sigma_b = \mu_a - \kappa_a \sigma_a$ would apply. The confidence level for both the IA and background is considered to be the same; $\kappa_b = \kappa_a = \kappa$. Therefore, k can be described as

$$k = \frac{\mu_a - \mu_b}{\sigma_a + \sigma_b} \quad (3)$$

We utilised the CV model method to perform an initial segmentation. From the segmentation results, the initial k_o can be calculated by Eq. (3). The initial T_o can subsequently be found using Eq. (2).

The initial zero level set is a rectangular prism surface, constructed by subtraction of two pixels on either side of the ROI. The parameter setting has since been discussed in our previous publication (Sen et al., 2013).

2.4. Haemodynamic simulation methods

2.4.1. Mesh generation

As the accuracy of CFD results depends highly upon grid resolution with use of a commercial software package ICEM CFD 14.1 (ANSYS, Canonsburg, PA, USA), a series of verification and validation analyses of mesh independent tests have been carried out upon commencement of this study. When the mesh number was found to have reached approximately 400,000 the results began to converge to a constant. Reproducible results could thus be obtained with a total of 600,000 finite elements and 240,000 nodes used in this study. In order to accurately calculate the WSS, five layers of prism mesh were inserted onto the artery's internal surface. The distance of the first prism mesh to the artery surface was set to 0.01 mm.

2.4.2. Blood flow modelling and boundary conditions

In this study, calculations were performed with steady flow rate of 250 ml/min, 150 ml/min, and 100 ml/min at the parent artery inlet for idealised models using average flow rate in the ICA, MCA, and AcomA respectively (Ford et al., 2005). CFD calculations were performed via the use of CFX 14.1 solver package (ANSYS). The blood was assumed to be a Newtonian fluid with blood flow density and dynamic viscosity of 1050 kg m^{-3} and 0.0035 Pa.s respectively (Shojima et al., 2004). By adopting the conventional assumption of a lack of resistance in the cerebral circulation, outlet boundary conditions at the section of extended 30 times of artery diameter were set to zero pressure (Karmonik et al., 2008).

2.4.3. Haemodynamic result analysis; energy loss

EL is calculated as the power difference from inlet to outlet, and can be calculated as follows:

$$EL = \sum\left(P_i + \rho\frac{1}{2}v_i^2\right) - \sum\left(P_o + \rho\frac{1}{2}v_o^2\right) \quad (4)$$

where ρ is density, v is velocity, I indicates inlet, and o means outlet. In order to calcualte the difference from each segmentation method, the energy loss difference is calculated via the following equation:

$$\Delta EL(\%) = \frac{|EL_{GT} - EL_I|}{EL_{GT}} \times 100 \quad (5)$$

where, GT is the ground truth method, and I is the segmentation method (TLS, RGT and CV).

2.4.4. Haemodynamic result analysis; wall shear stress (WSS)

The wall shear stress (WSS) is derived from predicted flow velocities, a parameter known to be associated with initial thickening and thrombosis formation.

Please cite this article as: Sen, Y., et al., Image segmentation methods for intracranial aneurysm haemodynamic research. Journal of Biomechanics (2014), http://dx.doi.org/10.1016/j.jbiomech.2013.12.035

WSS is defined as

$$WSS = -\mu \left.\frac{\partial v_t}{\partial n}\right|_{wall} \quad (6)$$

where n is the direction of vertical to the vessel wall, μ represents the dynamic viscosity, v is the velocity parallel to the wall and is a unit vector that lies perpendicular to the wall. Like EL, the WSS is also calculated via the difference between each segmentation method

$$\Delta WSS(\%) = \frac{|WSS_{GT} - WSS_I|}{EL_{GT}} \times 100 \quad (7)$$

where, GT is the ground truth method and I indicates the segmentation method (TLS, RGT and CV).

2.5. Segmentation results evaluation

IA volume size was calculated through use of the boundary geometry, segmented by various segmentation methods. The volume difference (VD) was calculated via utilisation of the equation, $VD = \left|\frac{(V_I - V_{GT})}{V_{GT}}\right| \times 100\%$, where V_{GT} represents the volume of GT and V_I represents the volume of the TLS, RGT or CV methods. Jaccard's measure (JM) is a volume overlap metric, utilised to count the percentage of voxel intersections for the paired segmentations; $JM = \frac{2|S_{GT} \cap S_I|}{S_{GT} \cup S_I}$, where S_{GT} represents the voxels created by the GT and S_I the voxels generated through use of the TLS, RGT or CV methods. Hausdorff distance (HD) measures the maximum surface distance. This measure is extremely sensitive to outliers and may not reflect the overall degree of correlation.

3. Results

3.1. Geometric shapes observation

Fig. 1e is a picture that was taken during treatment of an IA. Two protrusions; A and B, can be clearly observed in the IA, with protrusion A located upon the larger protrusion B. Fig. 1c and d indicates that the results of RGT and TLS methods segment both A and B protrusions. On the other hand, analysis of Fig. 1b reveals that the CV method leads to the display of protrusion B only, whilst protrusion A is not replicated in the segmented result.

3.2. Aneurysm segmentation results

All model volume differences are listed in Fig. 2. The largest difference in terms of IA volume, compared with the manual GT method, was found to be around 14.3% at AcomA IA via the use of the CV segmentation method. The maximum VD usually occurred in cases in which the IA was connected to multiple arteries. The results of VD from the TLS method appeared to be lower than those obtained via the other segmentation methods, with the average VD of TLS segmentation methods found to be 6.2% (SD= ± 2.9%), 8.5% (SD= ± 4.7%), 6.4% (SD= ± 4.8%) for ICA, MCA, and AComA IA respectively. Our study indicated that the volume differences seen in IA size may be controlled at a maximum under 15% (SD= ± 6.2%), through the use of various segmentation methods. The geometry volume overlaps ratio was calculated via the use of JM, with the results depicted in Fig. 3. The average overlap ratios are; 91.9%, 90.6%, and 90.8% for ICA, MCA, and AComA IAs respectively. The TLS method appears to exhibit higher values in terms of overlap ratio than the other two methods.

HD measurements indicate the maximum surface distance to outliers. The maximum HD usually occurs at the top of the IA; e.g. bleb location. Fig. 4 depicts the results of HD within three types of IA. The HD results obtained via the TLS method were shown to be lower than 0.8 pixel, coinciding with the results obtained via the manual GT method. The greatest HD was seen to occur in the MCA IA, a result hypothesised to be due to IA surface roughness; i.e. from blebs, and the entailing increase in segmentation complexity.

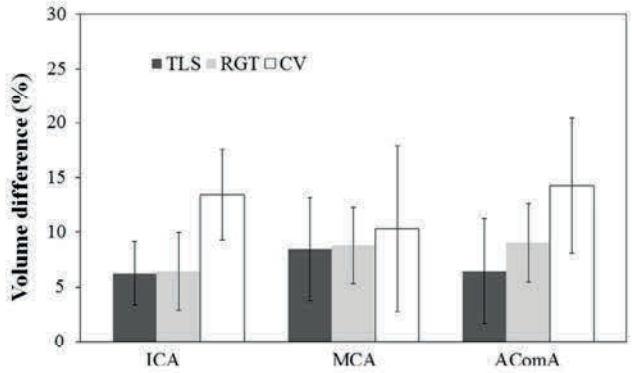

Fig. 2. Volume difference of segmentation methods in comparison to GT. The maximum volume differences may be controlled at under 15% (SD= ± 6.2%).

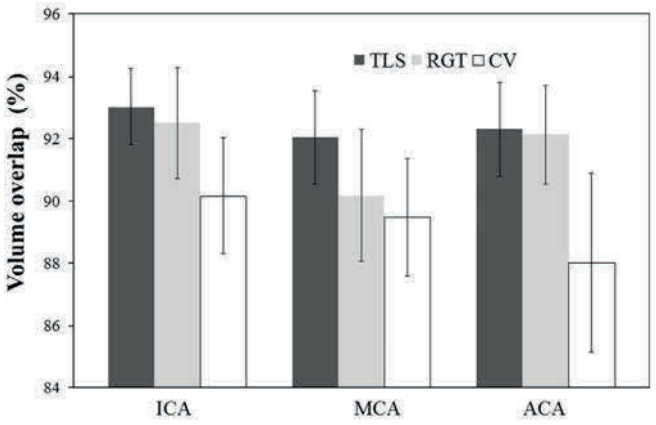

Fig. 3. Aneurysm and vessel volume overlap results comparison in relation to GT. The average overlap ratios are; 91.9%, 90.6%, and 90.8% for ICA, MCA, and AComA IAs respectively.

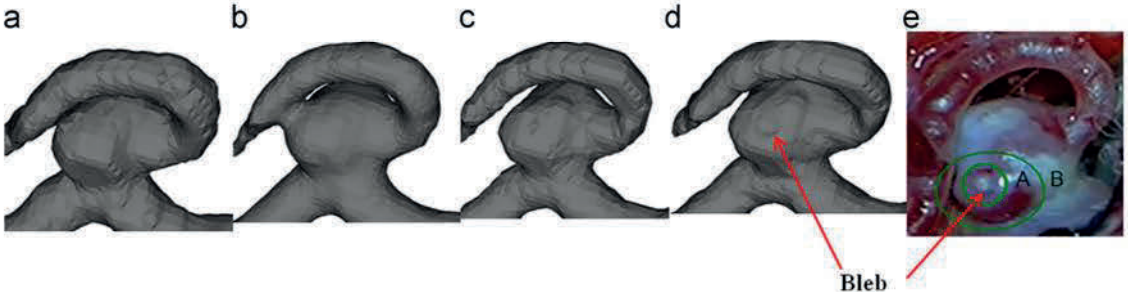

Fig. 1. Segmentation results comparison (aneurysm with bleb), from left to right: (a)GT, (b) CV, (c) RGT, (d) TLS, and (e) photo from open head surgery. The aneurysm bleb was only able to be observed by the TLS method (d).

Please cite this article as: Sen, Y., et al., Image segmentation methods for intracranial aneurysm haemodynamic research. Journal of Biomechanics (2014), http://dx.doi.org/10.1016/j.jbiomech.2013.12.035

3.3. Haemodynamic simulation results

CFD simulation is performed via a process that includes segmented geometries. Fig. 5 depicts the results of EL differences, with the average differences in EL calculated via the use of TLS, RGT, and CV segmentation methods found to be 20.6% (SD= ± 6.6%), 25.5% (SD= ± 8.7%), and 23.5% (SD= ± 10.8%) respectively ($P < 0.01$).

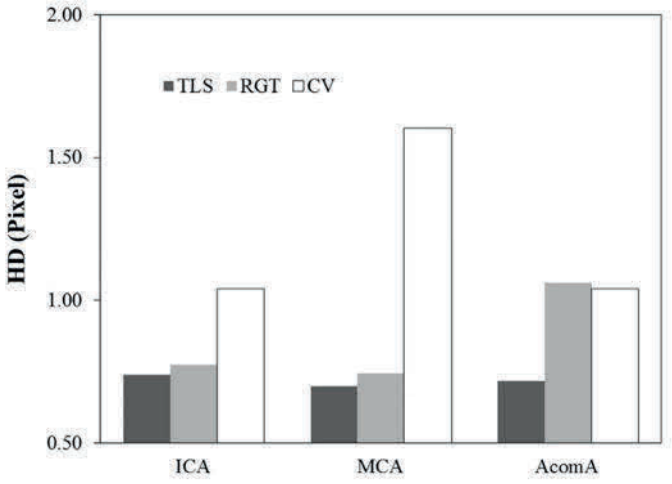

Fig. 4. Aneurysm HD results in comparison to GT. The TLS method was shown to be lower than 0.8 pixel compared to manual GT method.

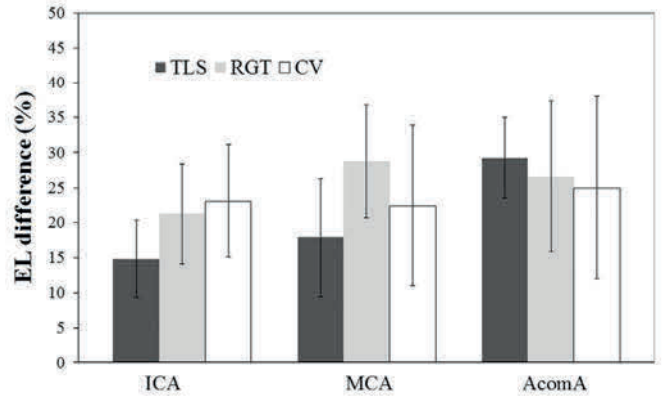

Fig. 5. Haemodynamic results; EL difference in comparison to GT. The average EL difference were 20.6% (SD= ± 6.6%), 25.5% (SD= ± 8.7%), and 23.5% (SD= ± 10.8%) for TLS, RGT, and CV respectively.

Fig. 6, on the other hand, illustrates pressure distributions upon the IA surface, with these distributions exhibiting insignificant variations across the various segmentation methods. Fig. 7 depicts the average results of the highest WSS, similarly calculated via the utilisation of the three segmentation methods. The average of the highest WSS difference, calculated from TLS, RGT, and CV segmentation methods, were found to be 18.2% (SD= ± 6.4%), 26.5% (SD= ± 11.5%), and 27.2% (SD= ± 7.6%) respectively ($P < 0.01$). In this study, the highest WSS was observed at the inlet of IA neck (seen in Fig. 8). We found significant discrepancies for the lowest WSS measured for each method. These average differences from the 45 IAs were found to be 144.3% (SD= ± 169.4%), 149.1% (SD= ± 128.5%), and 85.7% (SD= ± 75.4%) for TLS, RGT, and CV respectively ($P > 0.1$). The lowest WSS was found at the apex of the IA, a location which has a high risk of rupture, with most IA ruptures commonly occurring at the top of the IA, rather than its neck (Cebral et al., 2010). In particular, for ICA, MCA and AComA IAs respectively, there was a 99.8% (SD= ± 102.2%), 196.8% (SD= ± 204.1%), and 82.4% (SD= ± 66.9%) difference when compared to the results obtained via the manual GT segmentation method. This shows that the haemodynamic results are dependent upon the accuracy of segmentation methods. Fig. 8 illustrates the distribution of WSS via the use of different segmentation methods, with the maximum difference of the lowest WSS found to be 1033% in the AComA IA segmented by use of the RGT method. These results indicate that local differences arose for WSS, particularly in the region of the bulb.

Table 1 listed the details of all the segmentation and haemodynamics simulation results classified by IA locations and segmentation methods.

4. Discussion

The three segmentation methods assessed in this study are popular techniques, commonly utilised in medical image reconstruction. Although vessel boundary is easily extrapolated via the RGT method, there are problems related to the sensitivity of intensity threshold selection and seed position (Hu, 2009). Based on level set technique, the CV method is capable of defining vessel

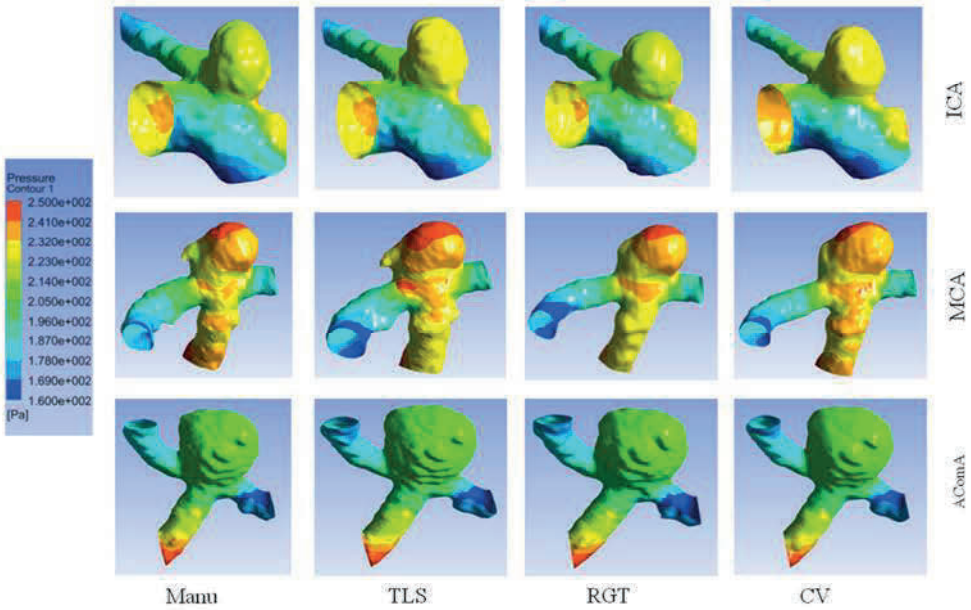

Fig. 6. Pressure distributions. The pressure distribution was insignificant.

Please cite this article as: Sen, Y., et al., Image segmentation methods for intracranial aneurysm haemodynamic research. Journal of Biomechanics (2014), http://dx.doi.org/10.1016/j.jbiomech.2013.12.035

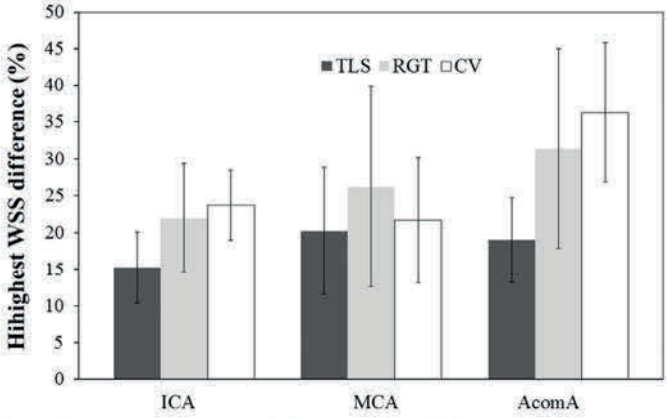

Fig. 7. Haemodynamic results; WSS (highest volume) difference in comparison to GT. The average of the highest WSS difference were 18.2% (SD= ± 6.4%), 26.5% (SD= ± 11.5%), and 27.2% (SD= ± 7.6%) for TLS, RGT and CV respectively.

boundaries despite lack of clarity, and is thereby able to allow modelling of images with approximate boundaries (Chan and Vese, 2001). This level of accuracy, however, is not sufficient for the conduction of haemodynamics studies. To counter this, the TLS method was proposed to improve upon these segmentation applications, a technique with the ability to segment IAs automatically without the setting of a seed point or intensity threshold, and is therefore applicable for the segmentation of complex cerebrovascular anatomical shapes (Sen et al., 2013). Our results have confirmed that the reconstructed geometry, segmented via the use of TLS, is able to be controlled within an acceptable range (VD < 10% SD= ± 5%, JM > 90%, and HD < 1 Pixel), with the differences significantly less than previous methods.

Our haemodynamic results indicate that the volumes of EL difference can be controlled to a level with deviations of around 23% between different segmentation methods. The results of the TLS method also reveal the lowest difference and deviation (20.6%, SD= ± 6.6%) when compared to the other methods. We found that

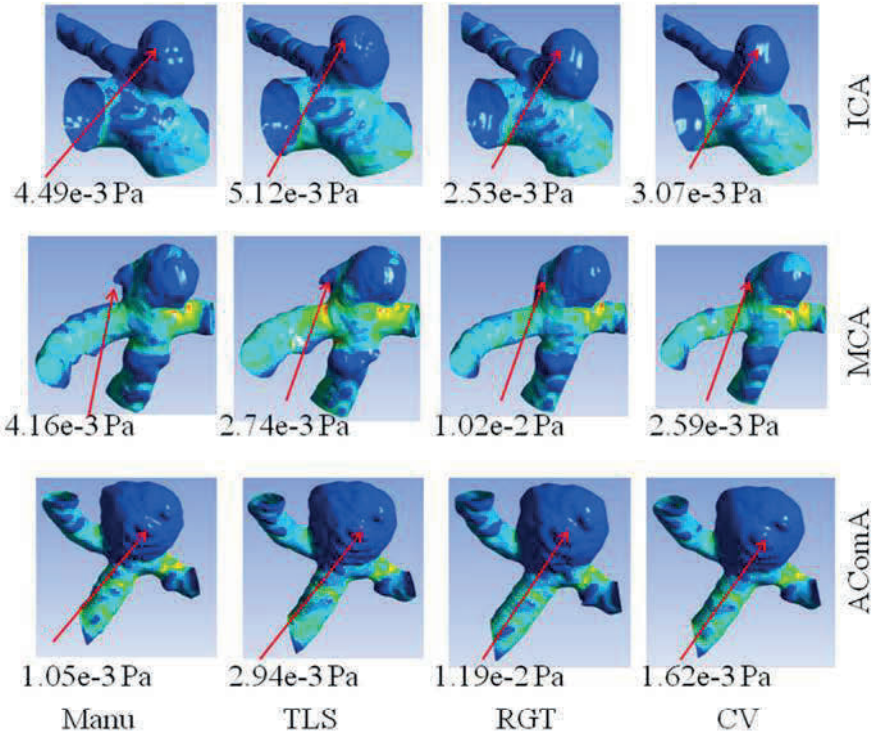

Fig. 8. WSS distributions. The lowest WSS appeared to be a significant difference between segmentation methods.

Table 1
Segmentation and haemodynamics simulation results.

IA location	ICA			MCA			AcomA		
Segmentation methods	TLS	RGT	CV	TLS	RGT	CV	TLS	RGT	CV
VD (%)	6.2	6.4	13.5	8.5	8.8	10.3	6.4	9.1	14.3
SD of VD (%)	± 2.9	± 3.5	± 4.1	± 4.7	± 3.5	± 7.6	± 4.8	± 3.6	± 6.2
JM (%)	93.0	92.5	90.2	92.0	90.2	89.5	92.3	92.1	88.0
SD of (JM %)	± 1.2	± 1.8	± 1.9	± 1.5	± 2.1	± 1.9	± 1.5	± 1.6	± 2.9
HD (Pixels)	0.74	0.77	1.04	0.70	0.75	1.61	0.72	1.06	1.04
ΔEL (%)	14.8	21.2	23.1	17.9	28.8	22.5	29.2	26.6	25.0
SD of ΔEL (%)	± 5.5	± 7.2	± 8.0	± 8.4	± 8.1	± 11.4	± 5.8	± 10.8	± 13.0
ΔWSS (highest) (%)	15.3	22.0	23.7	20.3	26.2	21.7	19.0	31.4	36.3
SD of ΔWSS (highest) (%)	± 4.8	± 7.3	± 4.8	± 8.6	± 13.6	± 8.5	± 5.8	± 13.6	± 9.5
ΔWSS (lowest) (%)	103.5	96.1	99.8	269.4	268.7	52.4	60.0	82.4	104.9
SD of ΔWSS (lowest) (%)	± 98.2	± 112.8	± 95.7	± 391.2	± 205.0	± 16.1	± 18.7	± 67.6	± 114.5

Please cite this article as: Sen, Y., et al., Image segmentation methods for intracranial aneurysm haemodynamic research. Journal of Biomechanics (2014), http://dx.doi.org/10.1016/j.jbiomech.2013.12.035

the results of WSS were notably technique dependent, particularly in terms of the quality of the lowest WSS. WSS is known to be calculated via local velocity vectors near the vessel surface (Eq. (6)), a major reason behind its sensitivity and influence by the local surface geometry. As mentioned in Eq. (4), EL is a scalar parameter which is typically only influenced by the flow parameter at both the inlet and outlet. Although the local geometry of the IA likewise influences the subsequent loss of flow power, the EL values obtained have been found to lie within a statistically reasonable range. Using the TLS method, VD and overlap difference can be restricted to a certain range (i.e.: under VD < 10% SD = ± 5%, JM > 90%, and HD < 1 Pixel). The values of EL were thus maintained at a given level throughout this study, with a deviation range below 23%. However, the results of WSS are uncontrollable and uncertain, with the maximum difference of WSS, particularly for lowest WSS, calculated to approach 1000% (10 times) that of the segmentation methods. These findings suggest that it may not be enough to introduce WSS parameters in estimating the risk of IA rupture until these segmentation methods are fully validated.

5. Conclusions

Three dichotomous segmentation methods were assessed for the analysis of 45 IA models in terms of geometric shape, volume, and haemodynamic results. Although based on the same medical imagery and data, different methods of image segmentation generated alterations in shape and volume, thereby resulting in significant variation in computed haemodynamic parameters. The results of EL were observed to be statistically stable as opposed to the relative uncertainty of the WSS, with the occurrence of uncertain results negatively affecting the accuracy of patient-specific haemodynamic applications. The TLS method was proposed to improve cerebrovascular IA segmentation applications, a technique with the ability to segment IAs automatically without the setting of a seed point or intensity threshold, and is likewise available for the segmentation of modifiable anatomical shapes.

Findings from this study suggest that a validation process to confirm the results of these segmentation techniques is important in limiting the error arising from manipulations of image data. With this, the results that are influenced by the segmentation process must be included in the haemodynamic study. Beside methods of segmentation, we also note that inflow condition is another important factor influencing the results of CFD simulation in IA haemodynamics (Karmonik et al., 2009). A series of in-vitro and in-vivo validation will be performed in our future research work to address this issue.

Conflict of interest statement

None of the authors have any financial interests to disclose in this study.

Acknowledgements

The authors would like to thank the members of Macquarie Medical Imaging, Macquarie University Hospital and Macquarie Medical Imaging for their kind support and contributions to these cases.

References

Castro, M.A., Putman, C.M., Cebral, J.R., 2005. Computational modeling of cerebral aneurysms in arterial networks reconstructed from multiple 3D rotational angiography images. Proc. SPIE, 233–244

Cebral, J.R., Castro, M.A., Burgess, J.E., Pergolizzi, R.S., Sheridan, M.J., Putman, C.M., 2005. Characterization of cerebral aneurysmas for assessing risk of rupture by using patient-specific computational hemodynamics models. AJNR. Am. J. Neuroradiol. 26 (10), 2550–2559.

Cebral, J.R., Sheridan, M., Putman, C.M., 2010. Hemodynamics and bleb formation in intracranial aneurysms. AJNR Am. J. Neuroradiol. 31, 304–310.

Chan, T.F., Vese, L.A., 2001. Active contours without edges. IEEE Trans. Image Process. 10 (2), 266–277.

de Rooij, N., Linn, F., van der Plas, J., Algra, A., Rinkel, G., 2007. Incidence of subarachnoid haemorrhage: a systematic review with emphasis on region, age, gender and time trends. J. Neurol. Neurosurg. Psychiatry 78 (12), 1365–1372.

Ford, M.D., Alperin, N., Lee, S.H., Holdsworth, D.W., Steinman, D.A., 2005. Characterization of volumetric flow rate waveformes in the normal internal carotid and vertebral arteries. Physiol. Meas. 26 (4), 477–488.

Hassan, T., Timofeev, E.V., Ezura, M., Saito, T., Takahashi, A., Takayama, K., Yoshimoto, T., 2003. Hemodynamic analysis of an adult vein of Galen aneurysm malformation by use of 3D image-based computational fluid dynamics. AJNR Am. J. Neuroradiol. 24 (6), 1075–1082.

Hu, Grossberg, Mageras, 2009. Survey of recent volumetric medical image segmentation techniques, Biomedical Engineering, Carlos Alexandre Barros de Mello (Ed.), ISBN: 978-953-307-013-1, InTech, http://dx.doi.org/10.5772/7865. Available from: http://www.intechopen.com/books/biomedical-engineering/survey-of-recent-volumetric-medical-image-segmentation-techniques.

Jonathan, L., Song, J.K., Newell, D.W., 2006. Cerebral aneurysms. N. Engl. J. Med. 355, 928–939.

Karmonik, C., Klucznik, R., Benndorf, G., 2008. Comparison of velocity patterns in an AComA aneurysm measured with 2D phase contrast MRI and simulated with CFD. Technol. Health Care 16, 119–128.

Karmonik, C., Yen, C., Grossman, R.G., Klucznik, R., Benndorf, G., 2009. Intraaneurysmal flow patterns and wall shear stresses calculated with computational flow dynamics in an anterior communicating artery aneurysm depend on knowledge of patient-specific inflow rates. Acta Neurochir. (Wien) 151, 479–485 (discussion 485).

Kassell, N.F., Torner, J.C., Haley, E.C., Jane, J.A., Adams, H.P., Kongable, G.L., 1990. The international cooperative study on the timing of aneurysm surgery. Part 1: overall management results. J. Neurosurg. 73 (1), 18–36.

Lesage, D., Angelini, E.D., Bloch, I., Funka-Lea, G., 2009. A review of 3D vessel lumen segmentation techniques: models, features and extraction schemes. Med. Image Anal. 13, 819–845.

Ma, B., Harbaugh, R.E., Raghavan, M.L., 2004. Three-dimensional geometrical characterization of cerebral aneurysms. Ann. Biomed. Eng. 32, 264–273.

Meng, H., Tutino, V.M., Xiang, J., Siddiqui, A., 2013. High WSS or low WSS? Complex interactions of hemodynamics with intracranial aneurysm initiation, growth, and rupture: toward a unifying hypothesis. AJNR Am. J. Neuroradiol., http://dxdoi.org/10.3174/ajnr.A3558

Mumford, D.B., Shah, J., 1989. Optimal approximations by piecewise smooth functions and associated variational problems. Commun. Pure Appl. Math. 42 (5), 577–685.

Phillips II, L.H., Whisnant, J.P., O'Fallon, W. Michael, Sundt , T.M., 1980. The unchanging pattern of subarachnoid hemorrhage in a community. Neurology 30, 1034–1040.

Qian, Y., Takao, H., Umezu, M., Murayama, Y., 2011. Risk analysis of unruptured aneurysms using computed fluid dynamics technology: preliminary results. AJNR Am. J. Neuroradiol. 32 (10), 1948–1955.

Raghavan, M.L., Ma, B., Harbaugh, R.E., 2005. Quantified aneurysm shape and rupture risk. J. Neurosurg. 102, 355–362.

Sen, Y., Qian, Y., Avolio, A., Morgan, M., 2013. Development of image segmentation methods for intracranial aneurysms. Comput. Math. Methods Med. 2013, 7.

Sen, Y., Qian, Y., Zhang, Y., Morgan, M., 2011. A comparison of medical image segmentation methods for cerebral aneurysm computational hemodynamics. In: Proceedings of the 2011 4th international conference on biomedical engineering and informatics (BMEI). pp. 901–904.

Shojima, M., Oshima, M., Takagi, K., Torii, R., Hayakawa, M., Katada, K., Morita, A., Kirino, T., 2004. Magnitude and role of wall shear stress on cerebral aneurysm: computational fluid dynamic study of 20 middle cerebral artery aneurysms. Stroke: J. Cereb. Circ. 35, 2500–2505.

Steinman, D.A., Milner, J.S., Norley, C.J., Lownie, S.P., Holdsworth, D.W., 2003. Image-based computational simulation of flow dynamics in a giant intracranial aneurysm. AJNR Am. J. Neuroradiol. 24 (4), 559–566.

Thomas, J.B., Milner, J.S., Rutt, B.K., Steinman, D.A., 2003. Reproducibility of image-based computational fluid dynamics models of the human carotid bifurcation. Ann. Biomed. Eng. 31, 132–141.

Vlak, M.H.M., Rinkel, G.J.E., Greebe, P., van der Bom, J.G., Algra, A., 2011. Trigger factors and their attributable risk for rupture of intracranial aneurysms: a case-crossover study. Stroke 42, 1878–1882.

Wermer, M.J.H., van der Schaaf, I.C., Algra, A., Rinkel, G.J.E., 2007. Risk of rupture of unruptured intracranial aneurysms in relation to patient and aneurysm characteristics: an updated meta-analysis. Stroke 38 (4), 1404–1410.

Zhang, H., Fritts, J.E., Goldman, S.A., 2008. Image segmentation evaluation: a survey of unsupervised methods. Comput. Vis. Image Underst. 110, 260–280.

Zuva, T., Olugbara, O.O., Ojo, S.O., Ngwira, S.M., 2011. Image segmentation, available techniques, developments and open issues. Can. J. Image Process. Comput. Vis. 2 (3), 20–29.

Please cite this article as: Sen, Y., et al., Image segmentation methods for intracranial aneurysm haemodynamic research. Journal of Biomechanics (2014), http://dx.doi.org/10.1016/j.jbiomech.2013.12.035

Investigation of Image Segmentation Methods for Intracranial Aneurysm Haemodynamic Research

Y. Sen, Y Zhang, Y. Qian, M. Morgan,
Australian School of Advanced Medicine
Macquarie University, Australia

Abstract

Patient-specific haemodynamic technology has been applied in clinical applications. Computational haemodynamic simulation is performed by utilization of geometric results obtained via medical image segmentation. However, the geometry and volume of intracranial aneurysm models are highly dependent upon different segmentation methods, even when employed upon the same medical imaging data. Moreover, methods of vascular segmentation have been insufficiently validated. In this study, we compared three segmentation methods; the Region Growing Threshold (RGT), Chan-Vese model (CV) and Threshold-Based Level Set (TLS), to segment the aneurysm geometry through the use of CTA image data. The results were evaluated via measurement of arterial volume differences (VD), local geometric shapes, and haemodynamic simulation results. We found that the maximum VD of three segmentation methods sat at around ±15%. Local artery anatomical shapes of aneurysms were likewise found to significantly influence segmentation results. The computational haemodynamic simulation was performed modelling three types of geometries, with typical haemodynamic characteristics; i.e. energy loss and shear stress. We found that there was a maximum of 58% difference between segmentation methods. The results indicated that it is essential to validate segmentation methods in order to confirm the quality of segmentation processes in the application of patient-specific cerebrovascular haemodynamic analysis.

Keywords: Medical image segmentation, Intracranial Aneurysm, level set, Region Growing Threshold, Haemodynamic

1 Introduction

Computed Tomography Angiography (CTA) is widely used in neurovascular imaging as a non-invasive diagnostic tool for detecting and evaluating intracranial aneurysms. This makes it possible to visualize three dimensional (3-D) cerebral aneurysms, allowing us to reconstruct patient specific vessels. Currently, the 3D geometry blood vessel has been applied to perform haemodynamic simulations. The results have been applied as an intelligent diagnosis tool to support aneurysmal treatment. Computational fluid dynamics (CFD) technology has been

applied to calculate blood pressure, velocity, wall shear stress (WSS), and energy loss (EL)[1].these parameters are difficult to obtain via direct measurements. These computational haemodynamic parameters have provided useful information in support of vascular surgeons in disease diagnoses and surgical preparation.

The accuracy of CFD simulation is highly dependent on vessel geometry [2]. The methods of segmentation of medical images directly influence the accuracy of aneurysm model construction, especially in the shapes and volumes of the vessel. Despite the many image segmentation methods, each with varying approaches and algorithms, there are currently no dominant segmentation methods, in terms of effectiveness, across all areas[3-5]. Our previous study has indicated that the volume of the aneurysm models exhibit variances across different segmentation methods, with the segmentation method likewise influencing the local geometric shapes of the aneurysms[6]. Validation will thus be an essential process, comparing segmentation methods and adjusting the parameters of these segmentation techniques in order to confirm the quality of patient-specific cerebral-vascular haemodynamic analysis. Although a number of commercial segmentation software packages have been released to the market, there is a conspicuous lack of methodological discussion and information regarding validation processes.

In this paper, six CTA image data, which include vascular and cerebral aneurysm images, are employed. Three segmentation methods; the Region Growing Threshold (RGT), Chan-Vese model (CV)[7], and Threshold-Based Level Set (TLS) are applied to segment these image data. We compared the difference, calculated from the above three segmentation methods, and performed CFD simulation in order to compare its influence upon haemodynamic research.

2 Materials and methods

All the experiments were performed on cropped data sets to reduce calculation time and memory usage. A region of interest (ROI), a good representation of the targeted aneurysm region for segmentation, is selected depending on the aneurysm size. All preparatory work is carried out prior to conduction of the experiments.

2.1 Region Growing Threshold Connecting (RGT)

The Region Growing Threshold method begins from a seed(s) which is selected within the area of the object to be segmented. This method requires two intensity values for the pixel of the object, with both a low threshold T_1 and high threshold T_2 value. Neighbouring pixels, whose intensity values fall inside this range are accepted and included in the region. When no more neighbouring pixels are found that satisfy the criterion, the segmentation is considered to have finished. The selection criterion is described by the following equation:

$$I(X) \in [X - T_1, X + T_2] \quad (1)$$

where T_1 and T_2 represent the low and high thresholds of the region intensities, *I(X)* represents the image and X the position of the particular neighbouring pixel being considered for inclusion in the region. Problems of RGT include threshold selection and sensitivity to seed position [8].

2.2 Chan-Vese model (CV)

The Chan-Vese model is based on the Mumford-Shah functional[9]. The associated evolution PDE in the level set framework is represented as:

$$\frac{\partial \varphi}{\partial t} = |\nabla \varphi| \left[\lambda_2 (I - \mu_{out})^2 - \lambda_1 (I - \mu_{in})^2 - \alpha + \beta div \left(\frac{\nabla \varphi}{|\nabla \varphi|} \right) \right] \quad (2)$$

where μ_{in} is the mean of the target object of intensity, μ_{out} represents the mean of the background of intensity and λ_1, λ_2 α, β are positive constants. In the Chan-Vese model, there is no utilization of a term related to the image gradient. Instead, it utilizes region intensity information for the target objects of segmentation. This model has exhibited a significantly effective performance in segmentation of images with unclear boundaries.

2.3 Threshold-Based Level Set (TLS)

The threshold-based level set combines the geodesic active contour[10] and the Chan-Vese model together within the level set framework.

Under the level set scheme, the contour deforms by the function; $\frac{\partial \Gamma(t)}{\partial t} + F|\nabla \varphi| = 0$, with an embedded surface $\Gamma(t)$ represented as the zero level set of φ by $\Gamma(t) = \{x, y \in R | \varphi(x, y, t) = 0\}$. F is a function for speed, which drives the $\Gamma(t)$ surface evolution in the normal direction. It is clear that F directly impacts upon the quality of medical image segmentation. The associated evolution PDE in the level set framework is as follows:

$$\frac{\partial \varphi}{\partial t} = |\nabla \varphi| \left(\alpha (I - T) + \beta div \left(g \frac{\nabla \varphi}{|\nabla \varphi|} \right) \right) \quad (4)$$

where I represents the image to be segmented, T represents the intensity threshold, g represents the image gradient, $\kappa = div \left(\frac{\nabla \varphi}{|\nabla \varphi|} \right)$ represents the curvature, α represents the image propagation constant and β represents the spatial modifier constant for the curvature κ. α and β weight the relative influence of each of these terms on the movement of the surface contour.

The threshold-based level set requires an appropriate estimate of the threshold from proper segmentation of the aneurysm, obtained via Chan-Vese model segmentation and the concepts of both confidence interval (CI) and confidence level (CL).

According to the theory of confidence interval, the lower bound threshold of the aneurysm can be defined by:

$$T_i = \mu_a - k_i \sigma_a \qquad i \geq 0 \quad (7)$$

The threshold T is the difference between the mean of the contour of the aneurysm (μ_a) and k times its standard deviation (σ_a). The intensities of the aneurysm and its background regions are different. The lowest intensity threshold of the aneurysm is the same as the highest intensity threshold of the background. Thus, $\mu_b + k_b \sigma_b = \mu_a - k_a \sigma_a$ would apply. The confidence level for both the aneurysm and background is considered to be the same; $k_b = k_a = k$. Therefore, k can be described as:

$$k = \frac{\mu_a - \mu_b}{\sigma_a - \sigma_b} \quad (8)$$

We utilized the Chan-Vese model method to perform an initial segmentation. From the segmentation results, the initial k_0 can be calculated by eqn.(8). The initial T_0 can subsequently be found using equation (7).

2.4 Data acquisition

Clinical studies were performed with the consent of the patient in relation to aneurysm image acquisition. These protocols were approved by the local institutional review board and the regional research ethics committee. Six data sets of patients with internal carotid artery aneurysms were acquired by 3D CTA scans (GE Healthcare).

Cross-sectional images were acquired by a CT angiography scanner with multidetector-row capability, a table speed of 9 mm/s and zero-degree table (and gantry tilt). Scanning started from the common carotid artery (CCA) and continued parallel to the orbito-meatal line to the level of the Circle of Willis, during which intravenous injection of contrast material was administered at a rate of 3.5mls/s. Aneurysm image was 512×512 pixel field, whilst continuous thickness slices were used to segment and reconstruct 3D vascular geometry. Pixels are expressed in Hounsfield Units (HU).

2.5 Haemodynamic analysis

CFD simulation includes three stages: 1) the segmentation of an aneurysm from medical imaging data recorded in DICOM format and generation of a STL format geometry data; 2) mesh generation; 3) CFD analysis. In the first stage, the segmentation methods mentioned above were introduced to reconstructive vessel and aneurysm geometry. In the second stage, ANSYS ICEM was used to form a mesh for CFD simulation. In the third stage, the geometric models are transferred to a haemodynamic system for CFD haemodynamic analysis.

2.5.1 Mesh generation

As the accuracy of CFD results depends upon grid resolution and boundary conditions, a series of analyses of verification and validation of mesh independent tests have been carried out at the beginning of this study. When the mesh number is found to be around at 400,000, the haemodynamic character; energy loss (EL), began to converge into a constant. Therefore, accurately reliable results could be obtained with a total of 563,000 finite elements and 240,000 nodes used in this study. In order to accurately calculate the WSS, five layers of prism mesh were inserted onto the artery's internal surface. The distance of the first prism mesh to the artery surface was set to 0.01 mm.

2.5.2 Calculation

The flow simulation is based on the Navier-Stokes (N-S) momentum equation and continuity equation as defined below:

$$\begin{cases} \dfrac{\partial}{\partial t}(\rho u_i)+\dfrac{\partial}{\partial x_j}(\rho u_i u_j)=-\dfrac{\partial p}{\partial x_i}+\dfrac{\partial}{\partial x_j}\left[\mu\left(\dfrac{\partial u_i}{\partial x_j}+\dfrac{\partial u_j}{\partial x_i}\right)\right] \\ \dfrac{\partial \rho}{\partial t}+\dfrac{\partial}{\partial x_j}(\rho u_j)=0 \end{cases} \tag{9}$$

Where i, j =1, 2, 3, x_1, x_2, x_3 represents coordinate axes, u_i, u_j and p are the velocity vectors and the pressure in the point of the fluid domain, ρ and μ are blood density and viscosity, t is time.

2.5.3 Energy loss

Energy loss is calculated as the power difference from inlet to outlet, and can be calculated as follows:

$$EL = \sum\left(P_i + \rho\frac{1}{2}v_i^2\right) - \sum\left(P_o + \rho\frac{1}{2}v_o^2\right) \tag{10}$$

where ρ is density, v is velocity, i indicates inlet, and o means outlet.

2.5.4 Wall Shear Stress (WSS)

The wall shear stress (WSS) is derived from predicted flow velocities. The parameter is known to be associated with initial thickening and thrombosis formation. The WSS is defined as:

$$WSS = -\mu\frac{\partial v_t}{\partial n}\Big|_{wall} \tag{11}$$

where μ is the dynamic viscosity, v is the velocity parallel to the wall and is the unit vector perpendicular to the wall.

3 Results

3.1 Geometric shapes

Fig. 1 d) is a picture which is taken during aneurysm treatment for Case 1. Two protrusions; A and B, are clearly observed in the aneurysm, with protrusion A located upon the larger protrusion B. Fig. 1 a) and c) indicate that the results of RGT and TLS methods segment both A and B protrusions. On the other hand, however, analysis of Fig. 1 b) reveals that the CV method leads to the display of only protrusion B, whilst protrusion A is not replicated in the segmented result.

3.2 Model volumes

All model volumes are listed in Fig. 2. The largest difference in terms of aneurysm volume, compared with TLS method, is around $\pm 15\%$, as was the case for Case 4. The difference across other cases was around ± 5 to $\pm 10\%$. The study indicates that the volume differences seen in aneurysm size may create an error of around 15%, through the use of various segmentation methods.

3.3 Haemodynamic Simulation Results

CFD simulation is performed by a process that includes segmented geometries. In order to compare various models under the same flow condition; inflow is assumed at 125 ml/min. The outflow condition is extended to a length distant enough to allow pressure recovery at the outlets. Fig. 3 illustrates the pressure distribution on the aneurysm surface (Case 1 and Case 4), with the pressure distributions being significantly different between the various segmentation methods. Fig. 4 shows the results of EL, which were calculated based upon the three types of segmentation methods. In particular, for Case 4, there is a 58% difference when compared to the results of TLS segmentation method. The results indicate that the extensive dependence of haemodynamic results on the accuracy of segmentation methods. Fig. 5 depicts the distribution of WSS between Case 1 and Case 4. The results indicate that local differences arose for WSS, particularly in bleb areas.

4 Conclusions

The study analysed six cerebral aneurysm models in geometric shape, volume and haemodynamic results. Although based on the same medical image data, different image segmentation methods generate alternations in shape, volume, thereby bringing significant haemodynamic results. The occurrence of uncertain results will negatively affect the accuracy of patient-specific haemodynamic applications.

The TLS method was proposed to improve cerebrovascular aneurysm segmentation applications, a technique with the ability to segment aneurysms automatically without the setting of a seed point or intensity threshold, which is likewise available for the segmentation of complex cerebrovascular anatomical shapes.

We believe a validation process to confirm segmentation will be an important study to limit the error arising from image segmentation. Results that are influenced by the segmentation process must be counted into the haemodynamic study. A series of in-vitro and in-vivo validation will thereby be performed in our projects.

5 Acknowledgement

The authors would like to thank members of Macquarie Medical Imaging, Macquarie University Hospital, for their kind support and contribution on these cases.

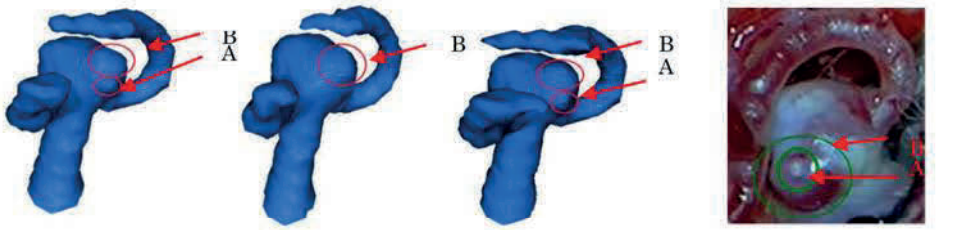

a) RGT b) CV c) TLS d) Surgical imagery

Figure 1: Geometric shape of aneurysm in Case 1

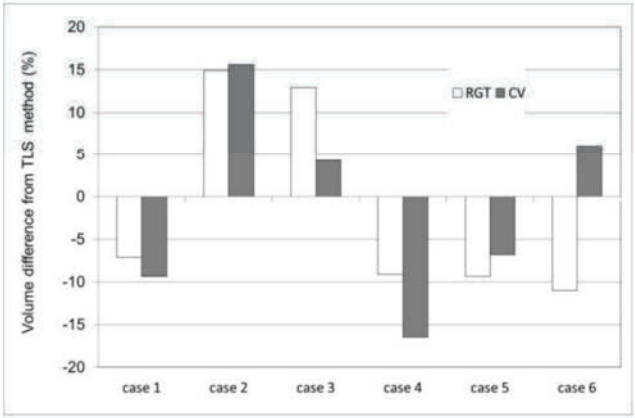

Figure 2: Aneurysm volume difference compared with TLS method

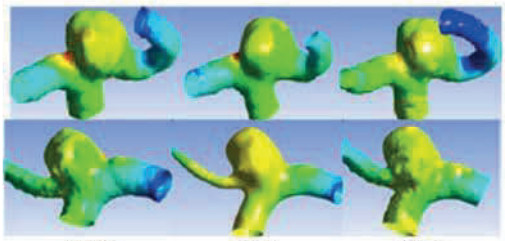

Figure 3: Pressure distribution: Top line; Case 1, Bottom line; Case 4

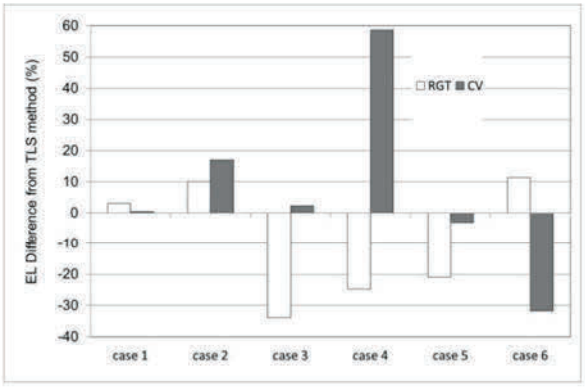

Figure 4: Haemodynamic results difference compared with TLS method

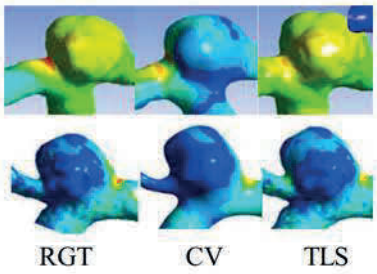

Figure 5: WSS distribution: Top line; Case 1, Bottom line; Case 4

References

[1] Y. Qian, et al., Risk Analysis of Unruptured Aneurysms Using Computed Fluid Dynamics Technology: Preliminary Results, AJNR Am J Neuroradiol. Nov-Dec 2011; 32(10):1948-55.

[2] Thomas, J.B., et al., Reproducibility of Image-Based Computational Fluid Dynamics Models of the Human Carotid Bifurcation. Annals of Biomedical Engineering, 2003. 31(2): p. 132-141.

[3] Zuva, T., et al., Image Segmentation, AvailableTechniques, Developments and Open Issues. Canadian Journal on Image Processing and Computer Vision, 2011. Vol. 2 No. 3: p. 20-29.

[4] Zhang, H., J.E. Fritts, and S.A. Goldman, Image segmentation evaluation: A survey of unsupervised methods. Computer Vision and Image Understanding, 2008. 110(2): p. 260-280.

[5] Lesage, D., et al., A review of 3D vessel lumen segmentation techniques: models, features and extraction schemes. Medical image analysis, 2009. 13(6): p. 819-45.

[6] Sen, Y., et al., A Comparison of Medical Image Segmentation Methods for Cerebral Aneurysm Computational Haemodynamics, in 2011 4th International Conference on Biomedical Engineering and Informatics (BMEI)2011. p. 901-904.

[7] Chan, T.F. and L.A. Vese, Active Contours Without Edges. IEEE TRANSACTIONS ON IMAGE PROCESSING 2001. vol. 10, no. 2: p. 266-277.

[8] Hu, G.a.M., Survey of Recent Volumetric Medical Image Segmentation Techniques, in Biomedical Engineering, C.A.B.d. Mello, Editor 2009, InTech.

[9] Mumford, D.B. and J. Shah, Optimal Approximations by Piecewise Smooth Functions and Associated Variational Problems. Communications on Pure and Applied Mathematics, 1989. 42(5): p. 577-685.

[10]Caselles, V., R. Kimmel, and G. Sapiro, Geodesic Active Contours. International Journal of Computer Vision, 1997. 22(1): p. 61-79.

Hindawi Publishing Corporation
Computational and Mathematical Methods in Medicine
Volume 2013, Article ID 715325, 7 pages
http://dx.doi.org/10.1155/2013/715325

Research Article

Development of Image Segmentation Methods for Intracranial Aneurysms

Yuka Sen, Yi Qian, Alberto Avolio, and Michael Morgan

The Australian School of Advanced Medicine, Macquarie University, Sydney, NSW 2109, Australia

Correspondence should be addressed to Yi Qian; yi.qian@mq.edu.au

Received 17 January 2013; Accepted 8 March 2013

Academic Editor: Peng Feng

Though providing vital means for the visualization, diagnosis, and quantification of decision-making processes for the treatment of vascular pathologies, vascular segmentation remains a process that continues to be marred by numerous challenges. In this study, we validate eight aneurysms via the use of two existing segmentation methods; the Region Growing Threshold and Chan-Vese model. These methods were evaluated by comparison of the results obtained with a manual segmentation performed. Based upon this validation study, we propose a new Threshold-Based Level Set (TLS) method in order to overcome the existing problems. With divergent methods of segmentation, we discovered that the volumes of the aneurysm models reached a maximum difference of 24%. The local artery anatomical shapes of the aneurysms were likewise found to significantly influence the results of these simulations. In contrast, however, the volume differences calculated via use of the TLS method remained at a relatively low figure, at only around 5%, thereby revealing the existence of inherent limitations in the application of cerebrovascular segmentation. The proposed TLS method holds the potential for utilisation in automatic aneurysm segmentation without the setting of a seed point or intensity threshold. This technique will further enable the segmentation of anatomically complex cerebrovascular shapes, thereby allowing for more accurate and efficient simulations of medical imagery.

1. Introduction

Specification of intracranial aneurysm morphology and hemodynamic analysis requires segmentation of vascular geometries from three-dimensional (3D) medical images, produced via CTA or MRA. Methods for such manipulations of medical images are directly linked to the accuracy of aneurysm model construction, particularly regarding the geometry of complex shapes and volumes. In most cases, this process involves extraction of the 2D image from CTA or MRA, followed by reconstruction of the 3D aneurysm surface model. As such, several approaches exist and are currently utilized in cerebrovascular segmentation. On one hand, the fuzzy-based approach has been adapted for detecting malformed and small vessels in MRA images [1], while region growing approaches are popular in medical image segmentation due to their simplicity and computational efficiency [2]. Major problems, however, include leakage when the boundary is blurred and sensitivity to seed position. Utilization of implicit active contour methods within the level set framework seems to be widespread in medical image segmentation [3–5] as the method does not suffer from parameterization surface problems [6] and has the capability to handle complex geometries and topological changes [7, 8]. More recently, active contour methods have also appeared in the modeling of intracranial aneurysms and cerebrovascular segmentation [9, 10]. Law and Chung proposed a method based upon multirange filters and local variances to perform the segmentation of intracranial aneurysms on Phase Contrast Magnetic Resonance Angiography data [11]. Hernandez and Frangi have developed a segmentation method for intracranial aneurysms based on Geometric Active Regions (GAR), using CTA and 3D Rotational Angiography data [12], whilst several Geodesic Active Contours (GAC) based methods have since been adapted for segmentation of brain aneurysms from CTA data [13, 14]. These methods either require sufficient training sets or they are reliant on boundary information obtained from medical imaging. Furthermore, boundary-based active contour level set methods may easily leak when the target boundary is not clearly defined. Though Firouzian et al. proposed a Geodesic Active Contours based level set method which employs region information and

intensity, it requires a user-defined seed point in order to calculate intensity threshold [15].

Despite the availabity of many image segmentation methods, with varying approaches and algorithms, there is no dominant method in terms of effectiveness, across all areas [16–18]. Our previous study indicated that the volume of the aneurysm models depends strongly on the different segmentation methods. The segmentation method likewise influences the local geometric shapes of the aneurysms [19]. Validation will thus become necessary, comparing segmentation methods and adjusting the parameters of these segmentation techniques in order to assure the quality of patient-specific cerebral-vascular hemodynamic analysis. Although a number of commercial software packages for segmentation are available in the market, there is a conspicuous lack of discussion of methodology and information regarding validation processes.

In this paper, the authors propose a new Threshold-Based Level Set method for cerebral aneurysms. This method is based on the Geodesic Active Contours model [20] and Chan-Vese model (CV) [21] integrating both region and boundary information to segment cerebral aneurysms through the use of a global threshold and gradient magnitude to form the speed function. The initial threshold is calculated from the Chan-Vese model and is then iteratively updated throughout the process of segmentation. Upon reaching the aneurysm boundary, the change in the threshold value will decrease because of the contrast between aneurysm and nonaneurysm intensities and the iteration will stop. The algorithm may then be implemented in an automatic or semiautomatic manner depending on the complexity of the aneurysm shape.

The results of 3D automatic aneurysm segmentations, from the Region Growing Threshold (RGT), the Chan-Vese model (CV), and the Threshold-Based Level Set (TLS), are compared to results obtained via manual segmentation, performed by an expert radiologist over eight data sets of CTA imagery. Evaluation was based on six validation metrics: volume difference (VD), Jaccard's measure (volume overlap metric, JM), false positive ratio (rfp), false negative ratio (rfn), Hausdorff distance (maximum surface distance, HD), and mean absolute surface distance (MASD). This study will also discuss the impact of parameter adjustments on segmentation results.

2. Methods

2.1. Region Growing Threshold Connecting (RGT). The Region Growing Threshold method starts with a seed(s), selected within the area of the object to be segmented. It requires two intensity values for the pixel of the object, a low threshold T_1, and high threshold T_2 values. Neighboring pixels whose intensity values fall within this range are accepted and included in the region. When no more neighbor pixels are found that satisfy the criterion, the segmentation is considered to have been completed. The selection criterion is described by the following equation:

$$I(X) \in [X - T_1, X + T_2], \tag{1}$$

where T_1 and T_2 represent the low and high thresholds of the region intensities, $I(X)$ represent the image, and X the position of the particular neighboring pixel being considered for inclusion in the region. Problems surrounding RGT include threshold selection and sensitivity to seed position [22].

2.2. Chan-Vese Model (CV) [21]. The Chan-Vese model is based upon the Mumford-Shah functional [23]. The associated evolution PDE in the level set framework is

$$\frac{\partial \varphi}{\partial t} = |\nabla \varphi| \left[\lambda_2 (I - \mu_{\text{out}})^2 - \lambda_1 (I - \mu_{\text{in}})^2 - \alpha + \beta \text{div}\left(\frac{\nabla \varphi}{|\nabla \varphi|} \right) \right], \tag{2}$$

where μ_{in} is the mean of the target object of intensity, μ_{out} represents the mean of the background of intensity, and λ_1, λ_2 α, and β are positive constants. The Chan-Vese model does not require a term related to the image gradient. Instead, region intensity information is utilized for the target objects of segmentation. This model has exhibited significant effectiveness in segmentation of images with blurred boundaries.

2.3. Threshold-Based Level Set (TLS). The Threshold-Based Level Set combines both the Geodesic Active Contour and the Chan-Vese model within the level set framework.

Under the level set scheme, the contour is seen to deform by the function; $\partial \Gamma(t)/\partial t + F|\nabla \varphi| = 0$, with an embedded surface $\Gamma(t)$ represented as the zero level set of φ by $\Gamma(t) = \{x, y \in R \mid \varphi(x, y, t) = 0\}$.

F represents a function for speed, which drives the $\Gamma(t)$ surface evolution in the normal direction. It is clear that F exerts a direct impact upon the quality of medical image segmentation. The associated evolution PDE in the level set framework is represented as follows:

$$\frac{\partial \varphi}{\partial t} = |\nabla \varphi| \left(\alpha (I - T) + \beta \text{div}\left(g \frac{\nabla \varphi}{|\nabla \varphi|} \right) \right), \tag{3}$$

where I represents the image to be segmented, T the intensity threshold, g is the image gradient, $\kappa = \text{div}(\nabla \varphi / |\nabla \varphi|)$ the curvature, α the image propagation constant, and β represents the spatial modifier constant for the curvature κ. α and β serve to weight the relative influence of each of these terms on the movement of the surface contour.

The first term of the RHS of the formula, $\alpha(I - T)$, defines the region where T is an automatically defined parameter indicating the lower boundary of the intensity level for the target object. In this work, the target aneurysm is always assumed to possess a relatively higher intensity level than its background. It can thus be seen that this first term forces the contours to enclose regions with intensity levels greater than T. When the contour lies within the aneurysm region, $(I - T) \geq 0$, it expands in the normal direction. When $(I - T) < 0$, the contour lies beyond the aneurysm region and thus shrinks with a negative speed. This process stops when the contours converge to the aneurysm boundary, with the

Table 1: Validation results of segmentation methods.

	Case 1	Case 2	Case 3	Case 4	Case 5	Case 6	Case 7	Case 8	Average
VD (%)									
GT	0	0	0	0	0	0	0	0	
TLS	1.55	4.69	4.48	0.46	2.92	0.12	3.55	2.27	2.51
RGT	7.65	4.47	8.86	1.37	5.52	6.09	3.21	10.90	6.01
CV	11.63	18.23	5.60	4.04	2.47	2.51	24.18	14.02	10.34
JM (%)									
GT	100	100	100	100	100	100	100	100	
TLS	91.87	89.66	88.57	93.25	91.64	92.35	91.55	93.79	91.59
RGT	90.12	88.24	87.02	93.00	91.39	90.90	94.27	89.58	90.57
CV	88.24	84.02	86.73	89.53	91.85	91.82	76.96	89.59	87.34
rfp (%)									
GT	0	0	0	0	0	0	0	0	
TLS	4.97	2.91	3.20	1.65	3.60	3.99	4.06	2.11	3.31
RGT	0.64	3.80	14.72	0.92	9.22	1.64	5.95	0.13	4.63
CV	11.84	18.02	13.26	5.38	4.60	5.54	28.75	11.62	12.38
rfn (%)									
GT	0	0	0	0	0	0	0	0	
TLS	3.57	3.25	1.51	5.21	1.40	3.97	4.73	4.23	3.48
RGT	9.26	8.40	0.17	6.15	0.18	7.61	0.12	10.30	5.27
CV	1.32	0.84	1.78	5.66	3.93	3.09	0.92	0.00	2.19
HD (pixel)									
GT	0	0	0	0	0	0	0	0	
TLS	0.51	0.65	0.68	1.17	0.79	1.89	0.65	0.79	0.89
RGT	0.77	0.64	0.89	1.41	0.55	1.86	0.49	0.76	0.92
CV	0.75	1.17	1.04	2.09	1.19	0.51	1.00	0.95	1.09
MASD (pixel)									
GT	0	0	0	0	0	0	0	0	
TLS	0.08	0.08	0.07	0.09	0.07	0.05	0.07	0.10	0.08
RGT	0.10	0.10	0.12	0.10	0.10	0.07	0.07	0.10	0.10
CV	0.06	0.06	0.07	0.11	0.08	0.05	0.07	0.10	0.08

image I reaching a threshold of T. If we isolate this first term of the RHS of (3), it becomes the selection criteria for the lower threshold in the Region Growing Threshold method. The second term in the formula would likewise become the Geodesic Active Contour term.

2.3.1. Method for Automatic Threshold Selection. The Threshold-Based Level Set requires an appropriate estimate of the threshold value from proper segmentation of the aneurysm, obtained using Chan-Vese model and the statistical data specifically, confidence interval (CI) and confidence level (CL).

2.3.2. Confidence Interval (CI) and Confidence Level (CL). The confidence level (CL) represents how often the true percentage of a population lies within the confidence interval (CI). Based on Chebyshev's inequality [24] a general relationship for symmetric distribution between CI and CL can be established. The inequality for symmetric distribution is given as

$$P\left(\left|X-\mu\right| \geq k\sigma\right) \leq \frac{1}{k^2} \quad k > 0, \tag{4}$$

where X is the random variable population, μ is the population mean, and confidence interval is represented by k times σ standard deviation. Equation (4) indicates that more than $(1 - (1/k^2) \times 100)$ percent of the population lies between k standard deviations from the population mean.

For nonsymmetric distribution, the one-tailed version of the inequality is used. This is given by

$$P\left(X-\mu \geq k\sigma\right) \leq \frac{1}{1+k^2} \quad k > 0. \tag{5}$$

For this inequality, it follows that when $k = 1$, more than 50% of the population is located one standard deviation away from the mean.

2.3.3. Initial Threshold Selection. According to the theory of confidence interval, the lower bound threshold of the aneurysm can be defined by

$$T_i = \mu_a - k_i\sigma_a \quad i \geq 0. \tag{6}$$

The threshold T represents the difference between the mean of the intensity of the aneurysm (μ_a) and k times its standard

deviation (σ_a). The intensities of the aneurysm and its background regions are different, with the lowest intensity threshold of the aneurysm being the same as the highest intensity threshold of the background. Thus, the relationship $\mu_b + k_b\sigma_b = \mu_a - k_a\sigma_a$ would apply. The confidence levels for both the aneurysm and its background are considered to be the same; $k_b = k_a = k$, thereby allowing k to be expressed as

$$k = \frac{\mu_a - \mu_b}{\sigma_a - \sigma_b}. \quad (7)$$

We have utilized the Chan-Vese model method to perform an initial segmentation. From the results obtained, the initial k_0 was seen to be calculated via (7). The initial T_0 can likewise be found using (6).

2.4. Data Acquisition. Clinical studies were performed with the consent of the patient in relation to acquisition of aneurysm images. These protocols were approved by the local institutional review board and the regional research ethics committee, with eight data sets of patients harboring internal carotid artery aneurysms acquired by 3D CTA scans (GE Healthcare).

Cross-sectional images were acquired by a CT angiography scanner with multidetector-row capability, a table speed of 9 mm/s, and zero-degree table (and gantry tilt). Scanning was initiated from the common carotid artery and continued parallel to the orbitomeatal line to the level of the Circle of Willis, during this intravenous injection of contrast material was administered at a rate of 3.5 mls/s. Aneurysm image was 512 × 512 pixel field, while slices of continuous thickness were used to segment and reconstruct 3D vascular geometry. Pixels are expressed in Hounsfield Units (HU).

2.5. Experiment Setting. For quantitative evaluation, manual segmentation of eight aneurysms using open source software, 3D Slicer, was conducted by an expert radiologist. The results were utilized as a ground truth (GT) for the comparison of other methods. A region of interest (ROI), a good representation of the targeted region for segmentation, was selected depending on the aneurysm size. All the experiments were performed on cropped data sets to reduce calculation time and memory usage, with preparatory work being completed prior to the conduction of the experiments.

2.5.1. Parameter Setting

The Threshold-Based Level Set. The initial zero level set is a rectangular prism surface, constructed by the subtraction of two pixels on either side of the ROI. Thus, three parameters needed to be set: α, β from (3) and c from (8). All eight experiments utilized a fixed setting of $\alpha = 10$, $\beta = 3$, and c in the range between 0.1 and 0.01. The role of this will be analyzed in Section 4.

The Chan-Vese Model. The initial zero level set is a cuboid surface, constructed in the same manner as the TLS, with the parameters in (2) fixed for all cases; $\lambda_1 = \lambda_2 = 0.001$, $\alpha = 0$, and $\beta = 0.3$.

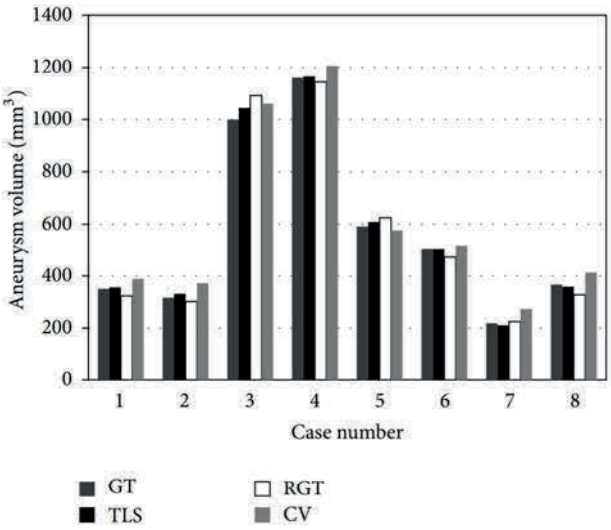

FIGURE 1: Aneurysm volume against segmentation methods.

The Region Growing Threshold. According to each case, an initial seed point is required to determine the starting loci within the specific aneurysm. For low and high intensity thresholds T_1 and T_2 in (1), T_1 was selected to utilize the threshold of the TLS result for each case, with T_2 representing the highest intensity of the aneurysm.

2.6. Evaluation

(i) Aneurysm volume was calculated through the use of the boundary geometry, segmented using various methods. The volume difference (VD) was calculated using the equation $\text{VD} = |(V_2 - V_1)/V_1| \times 100\%$, where V_1 represents the volume of GT and V_2 represents the volume of the TLS, RGT, or CV methods.

(ii) Jaccard's measure (JM) is a volume overlap metric, used to count the percentage of voxel intersections for the paired segmentations.

This can be seen as $\text{JM} = 2 * |S_1 \cap S_2|/S_1 \cup S_2$, where S_1 represents the voxels created by the GT and S_2 the voxels generated through the use of the TLS, RGT, or CV methods.

(iii) False positive ratio (rfp) represents the percentage of the extra voxels of S_2, located outside of S_1. When the rfp equates to zero, no voxels in S_2 will be located outside of S_1. Accordingly, $\text{rfp} = (|s_2| - |s_1 \cap s_2|)/|s_1|$, where S_1 represents the voxels created by the GT and S_2 represents the voxels generated by the TLS, RGT, or CV methods.

(iv) False negative ratio (rfn) represents the percentage of the lost voxels of S_2, which cover the internal surface of the S_1.

This may be seen as $\text{rfn} = (|s_1| - |s_1 \cap s_2|)/|s_1|$, where S_1 represents the voxels created by the GT and S_2

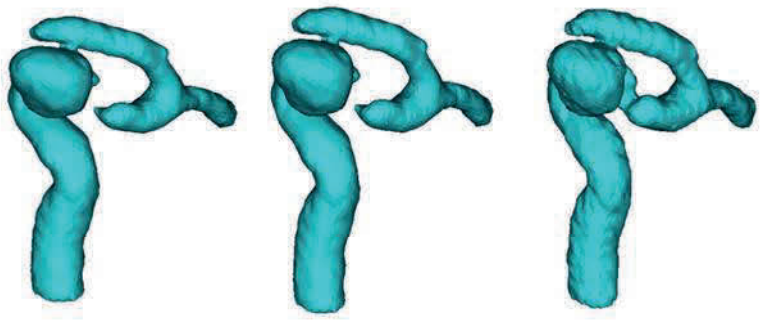

Figure 2: 3D geometries of segmentation results comparison, from left to right: CV, RGT, and TLS.

Figure 3: Segmentation results comparison (Case 1, aneurysm with bleb), from left to right: GT, CV, RGT, TLS, and photo from open head surgery.

represents the voxels generated by the TLS, RGT, or CV methods.

(v) Hausdorff distance (HD) measures the maximum surface distance. This measure is extremely sensitive to outliers and may not reflect the overall degree of correlation.

(vi) The mean absolute surface distance (MASD) indicates the average degree of difference between two surfaces and does not depend on aneurysm size [15].

3. Results

The calculated values of VD, JM, rfp, rfn, HD, and MASD for the eight cases considered are tabulated in Table 1. The average values are also shown. Figure 1 depicts the volume of the aneurysm. The minimum VD can be seen in the TLS method. The average value of VD is seen to be 2.51%. The maximum VD, however, is seen for Case 7 using the CV method. The values of JM indicate that the TLS method has the highest overlap rate in comparison to the other two methods, with an average of 91.59%. A study of rfp and rfn indicates a 3.31% overflow and 3.48% absence on average for the TLS method. The largest rfp and the smallest rfn were found to occur via the use of the CV method. These results likewise indicate that the largest volume was generated by the CV method, when compared to all other methods.

Results obtained for the surface distance metrics (HD and MASD) indicate the reliability of all segmentation methods, with the HD values for the TLS method being between 0.51 to 1.89 pixels and the maximum MASD being 0.08.

Figure 2 shows the 3D geometry of Case 4, restructured via three segmentation methods. Only TLS was effective in fully reconstructing the parent artery and aneurysm, while the other two methods were not able to construct a portion of the artery. One reason for this is that the aneurysm size in Case 4 is larger in comparison to other cases. Another point is that the distal parent artery itself is curved to lie proximally to the aneurysm. These results likewise indicate that the TLS method may be utilized in the segmentation of aneurysms with blurred boundaries.

Figure 3 represents the segmented aneurysm surfaces of Case 1, where only TLS is able to restructure the bleb located at the top of the aneurysm. The resulting image is similar to the picture taken during open-skull surgery.

4. Discussion

4.1. TLS Boundary Detect Function. In this study, the TLS method utilizes a boundary feature map:

$$g\left(|\nabla I|\right) = \frac{1}{1 + c|\nabla I|^2}, \tag{8}$$

where g is for the detection of vascular boundaries, $|\nabla I|$ represents a gradient magnitude, and c is a constant that controls the slope of the boundary detect function, $g(|\nabla I|)$. At the region of the artery and aneurysm, the boundary intensity gradient was seen to increase significantly. Thus, a relatively low c value was sufficient for the adjustment of the decreasing speed of g, in order to ensure that the search for the boundary surface was stopped at the arterial boundary. Figure 4 shows the process of selection for the value of c in Case 1; the results indicating that both VD and JM converged to a constant and MASD ceased all fluctuation when c was taken to equate to 0.5.

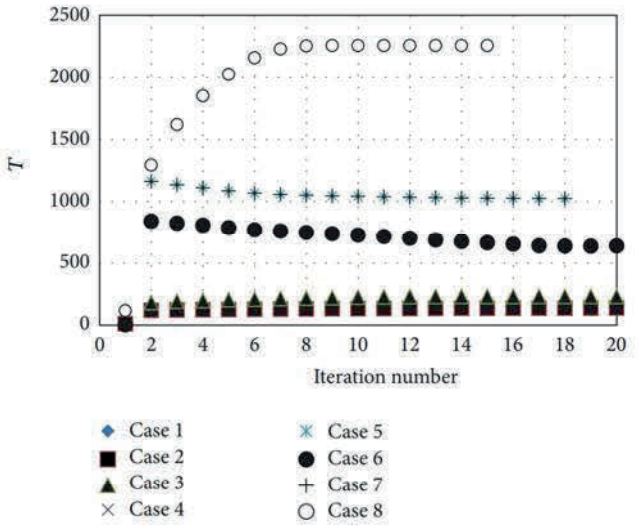

FIGURE 4: The convergence history of threshold T.

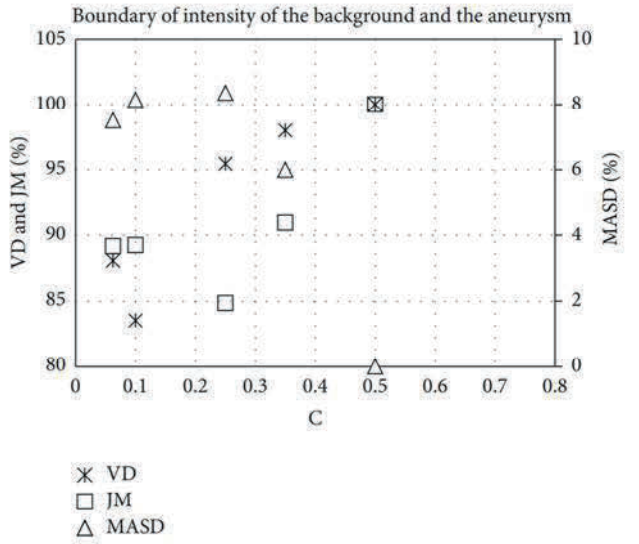

FIGURE 5: Validation of TLS boundary detect function C (Case 1).

4.2. TLS Threshold. The convergence history of threshold T is shown in Figure 5, with the T volumes exhibiting a tendency to converge after 15 iterations. The stability of the T volume against a range of value of c was likewise tested. The volume was found to be very stable for the range of c between 0.5 and 0.7. We thus suggest that the value of c is set at a volume between 0.5 and 0.7 for accurate boundary detection. As it is only TLS that does not require selection of any seeds during segmentation, it is suitable for the performance of automatic segmentations.

5. Conclusion

Various methods of segmentation generate a range of geometric models with changes in shape and volume, with the occurrence of uncertain results having the reductive potential to negatively affect clinical treatment decisions. Through analysis of eight cerebral aneurysm models, this study indicated that limitations continue to surround current segmentation methods. The validation of the methods and analysis of errors seem vital. In this study, the TLS method was proposed to improve cerebrovascular aneurysm segmentation application. It is a technique with the ability to segment aneurysms anatomically without the setting of a seed point or intensity threshold. The method is also suitable for the segmentation of complex cerebrovascular anatomical shapes.

Acknowledgments

The authors would like to thank members of Macquarie Medical Imaging, Macquarie University Hospital, for their kind support and contributions to these cases.

References

[1] N. D. Forkert, A. Schmidt-Richberg, J. Fiehler et al., "Fuzzy-based vascular structure enhancement in Time-of-Flight MRA images for improved segmentation," *Methods of Information in Medicine*, vol. 50, no. 1, pp. 74–83, 2011.

[2] B. E. Chapman, J. O. Stapelton, and D. L. Parker, "Intracranial vessel segmentation from time-of-flight MRA using preprocessing of the MIP Z-buffer: accuracy of the ZBS algorithm," *Medical Image Analysis*, vol. 8, no. 2, pp. 113–126, 2004.

[3] M. Droskey, B. Meyerz, M. Rumpfy, and K. Schaller, "An adaptive level set method for medical image segmentation," in *Proceedings of the Annual Symposium on Information Processing in Medical Imaging*, London, UK, 2001.

[4] M. E. Leventon, W. E. L. Grimson, and O. Faugeras, "Statistical shape influence in geodesic active contours," in *Proceedings of IEEE Conference on Computer Vision and Pattern Recognition (CVPR '00)*, pp. 316–323, June 2000.

[5] P. A. Yushkevich, J. Piven, H. C. Hazlett et al., "User-guided 3D active contour segmentation of anatomical structures: significantly improved efficiency and reliability," *NeuroImage*, vol. 31, no. 3, pp. 1116–1128, 2006.

[6] J. A. Sethian, *Level Set Methods and Fast Marching Methods: Evolving Interfaces in Geometry, Fluid Mechanics, Computer Vision, and Materials Science*, Cambridge University, 2nd edition, 1999.

[7] M. Kass, A. Witkin, and D. Terzopoulos, "Snakes: active contour models," *International Journal of Computer Vision*, vol. 1, no. 4, pp. 321–331, 1988.

[8] S. Osher and J. A. Sethian, "Fronts propagating with curvature-dependent speed: algorithms based on Hamilton-Jacobi formulations," *Journal of Computational Physics*, vol. 79, no. 1, pp. 12–49, 1988.

[9] S. Demirci, G. Lejeune, and N. Navab, "Hybrid deformable model for aneurysm segmentation," in *Proceedings of IEEE International Symposium on Biomedical Imaging: From Nano to Macro (ISBI '09)*, pp. 33–36, July 2009.

[10] N. Wilson, K. Wang, R. W. Dutton, and C. Taylor :, "A software framework for creating patient specific geometric models from medical imaging data for simulation based medical planning of vascular surgery," in *Proceedings of the 4th International Conference on Medical Image Computing and Computer-Assisted Intervention (MICCAI '01)*, pp. 449–456, 2001.

[11] M. W. K. Law and A. C. S. Chung, "Vessel and intracranial aneurysm segmentation using multi-range filters and local variances," in *Proceedings of the International Conference on Medical Image Computing and Computer-Assisted Intervention (MICCAI '07)*, vol. 10, part 1, pp. 866–874, 2007.

[12] M. Hernandez and A. F. Frangi, "Non-parametric geodesic active regions: method and evaluation for cerebral aneurysms segmentation in 3DRA and CTA," *Medical Image Analysis*, vol. 11, no. 3, pp. 224–241, 2007.

[13] T. Deschamps, P. Schwartz, D. Trebotich, P. Colella, D. Saloner, and R. Malladi, "Vessel segmentation and blood flow simulation using level-sets and embedded boundary methods," *International Congress Series*, vol. 1268, pp. 75–80, 2004.

[14] R. Manniesing, B. K. Velthuis, M. S. van Leeuwen, I. C. van der Schaaf, P. J. van Laar, and W. J. Niessen, "Level set based cerebral vasculature segmentation and diameter quantification in CT angiography," *Medical Image Analysis*, vol. 10, no. 2, pp. 200–214, 2006.

[15] A. Firouzian, R. Manniesing, Z. H. Flach et al., "Intracranial aneurysm segmentation in 3D CT angiography: method and quantitative validation with and without prior noise filtering," *European Journal of Radiology*, vol. 79, no. 2, pp. 299–304, 2011.

[16] T. Zuva, O. O. Olugbara, S. O. Ojo, and S. M. Ngwira, "Image segmentation, available techniques, developments and open issues," *Canadian Journal on Image Processing and Computer Vision*, vol. 2, no. 3, pp. 20–29, 2011.

[17] H. Zhang, J. E. Fritts, and S. A. Goldman, "Image segmentation evaluation: a survey of unsupervised methods," *Computer Vision and Image Understanding*, vol. 110, no. 2, pp. 260–280, 2008.

[18] D. Lesage, E. D. Angelini, I. Bloch, and G. Funka-Lea, "A review of 3D vessel lumen segmentation techniques: models, features and extraction schemes," *Medical Image Analysis*, vol. 13, no. 6, pp. 819–845, 2009.

[19] Y. Sen, Y. Qian, Y. Zhang, and M. Morgan :, "A comparison of medical image segmentation methods for cerebral aneurysm computational hemodynamics," in *Proceedings of the 4th International Conference on Biomedical Engineering and Informatics (BMEI '11)*, vol. 2, pp. 901–904, 2011.

[20] V. Caselles, R. Kimmel, and G. Sapiro, "Geodesic active contours," *International Journal of Computer Vision*, vol. 22, no. 1, pp. 61–79, 1997.

[21] T. F. Chan and L. A. Vese, "Active contours without edges," *IEEE Transactions on Image Processing*, vol. 10, no. 2, pp. 266–277, 2001.

[22] Hu, Grossberg, and Mageras, "Survey of recent volumetric medical image segmentation techniques," in *Biomedical Engineering*, C. A. B. de Mello, Ed., InTech, 2009.

[23] D. B. Mumford and J. Shah, "Optimal approximations by piecewise smooth functions and associated variational problems," *Communications on Pure and Applied Mathematics*, vol. 42, no. 5, pp. 577–685, 1989.

[24] J. Russell and R. Cohn, *Chebyshev's Inequality*, Book on Demand, 2012.

A Comparison of Medical Image Segmentation Methods for Cerebral Aneurysm Computational Hemodynamics

Y Sen
Australian School of Advanced Medicine
Macquarie University
Sydney, Australia

Y Qian
Australian School of Advanced Medicine
Macquarie University
Sydney, Australia

Y Zhang
Australian School of Advanced Medicine
Macquarie University
Sydney, Australia

M Morgan
Australian School of Advanced Medicine
Macquarie University
Sydney, Australia

***Abstract*— Patient-specific hemodynamic technology has been applied in clinical applications. However, the process of vessel segmentation was insufficiently validated. In order to confirm the accuracy of medical image segmentation methods, 13 image segmentation methods are introduced in this study to compare the results of cerebral-vascular aneurysms and its parent arteries from three-dimensional computed tomography (3D CT) images. This study indicates that the volume of the aneurysm models can reach difference of 11% with different segmentation methods under the same intensity threshold. The same segmentation methods under different intensity ranges can cause a volume change of up to 18%. The segmentation method also influences the local geometric shapes of the aneurysms. Some segmentation methods change subtle aspects of the anatomical shapes, which significantly influences the hemodynamic analysis and clinical decision. Computational hemodynamic simulation is performed by using the geometric results from segmentation. The hemodynamic characters; i.e. energy loss, are found to have a maximum of 34.8% in difference from segmentation. The results indicate that validation will be an essential process in the confirmation of the segmentation quality of patient-specific cerebral-vascular hemodynamic analysis.**

Keywords- medical imaging; image segmentation; region growing; threshold; computational hemodynamics; computed tomography

I. INTRODUCTION

Within the last ten years, there have been significant advances in computed tomography (CT) technology and improvements in medical image processing. This makes it possible to visualize patient-specific cerebral aneurysms in three-dimensions, allowing us to simulate the blood flow and provide an intelligent diagnosis for aneurismal treatment. Computational fluid dynamics (CFD) of hemodynamics is used for blood flow simulation by calculating pressure and velocity fields in geometric models of aneurysms constructed from medical images. Computed results potentially provide a set of hemodynamic parameters, such as wall shear stress (WSS) and energy loss (EL), which are not easily acquired by direct measurements. These results describe the blood flow by quantization and assist neurosurgery specialists with diagnoses and treatment of the aneurysm.

Accuracy of CFD simulation results depends on geometric models [1]. The methods of segmentation of medical images are directly linked to the accuracy of aneurysm model construction, especially in geometric shapes and volumes. This research analysed the difference between a set of models in regard to shapes, volumes and CFD simulation results and validated the shape of the models with real surgical imagery. The study employed 13 geometric aneurysm models in which 12 models are generated by use of a region growing segmentation method that consists of three noise removing algorithms and four intensity fields. Another is generated by commercial software (Mimics). All of the models were based on patient-specific CT DICOM (Digital Imaging and Communications in Medicine) data.

II. MATERIALS AND METHODS

The study includes three stages: 1) the segmentation of an aneurysm from medical imaging data recorded in DICOM format; 2) generation of a STL format geometric model; 3) CFD analysis. In the first stage, three edge preserving smoothing methods, gradient anisotropic diffusion, curvature anisotropic diffusion, and curvature flow [2], are introduced to eliminate the noise from the DICOM image data. A region growing threshold connecting method is adopted for segmentation vascular tissues. The segmentation method of threshold connection is significantly more effective in CT image data [3]. The Insight Toolkit (ITK) is implemented as a programming tool in this study. In the second stage, the open source software 3DSlicer, is used to generate geometric models. Parameters for model making will be explained in the following section. In the third stage, the geometric models are transferred to a hemodynamic system to generate meshing for CFD hemodynamic analysis.

A. *Medical image data segmentation*

Clinical studies were done with the consent of the patient in relation to aneurysm image acquisition. These protocols were approved by the local institutional review board and the regional research ethics committee.

Cross-sectional images were acquired by a CT angiography scanner (GE Medical Systems), with multidetector-row capability, a table speed of 9 mm/s and zero-degree table (and gantry tilt). Scanning started from the common carotid artery (CCA) and continued parallel to the orbito-meatal line, until the level of Circle of Willis during which the intravenous injection of contrast material was injected at the rate of 3.5mls/s. Fig.1 shows one such image of the aneurysm. 512×512 pixel field, continuous 0.625 mm thick 210 slices were used to segment and reconstruct 3D vascular geometry. Pixels are expressed in Hounsfield Units (HU).

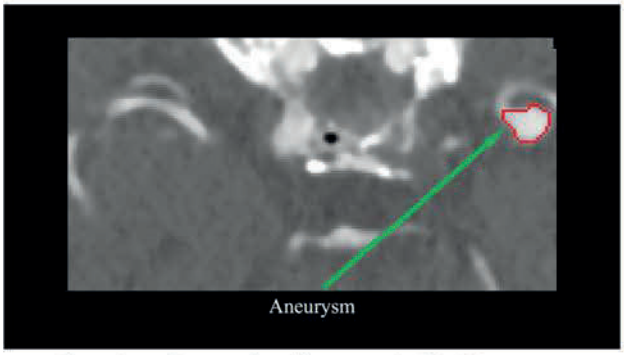

Figure 1. Cross-sectional image acquired by CT scan

Three methods of edge preserving smoothing are applied to reduce noise on images

1) *Gradient Anisotropic Diffusion (GAD)*

Anisotropic diffusion is a non-linear smoothing method. It produces a Gaussian smoothed image, which is the solution to the heat equation, with a variable conductance term to limit smoothing on edges. For the GAD method, the conductance term is a function of the gradient magnitude of the image at each point. The method uses 3 parameters: number of iterations=5, time step=0.0625 and conductance=3.

2) *Curvature Anisotropic Diffusion (CAD)*

The CAD method performs anisotropic diffusion on an image using a modified curvature diffusion equation (MCDE). MCDE does not exhibit the edge enhancing properties of classic anisotropic diffusion. The CAD method is less sensitive to contrast than other anisotropic diffusion methods and preserves finer detail structures in images. The CAD method uses 3 parameters: the number of iterations=5, the time step=0.0625 and the conductance=3.

3) *Curvature Flow(CF)*

The CF method performs a process of edge-preserving smoothing similar to classical anisotropic diffusion. The method uses a level set formation, where the iso-intensity contours in an image viewed as level sets and pixels of a particular intensity, form one level set. The level set function is then evolved under the control of a diffusion equation. The CF method will cause removal of image information, as each contour shrinks to a point and disappears. The CF method uses 2 parameters: the number of iterations=10 and time step=0.0625.

The method of region growing threshold connection is applied for the segmentation of vascular tissues. The pixel value in a CT image is reported in Hounsfield units, which are calibrated to correspond to the attenuation of x-rays, measured within the particular sample of tissue. Two low intensity thresholds (120, 150) HU and two high intensity thresholds (420, 500) HU are employed in this study. A seed point within the aneurysm is provided and a region growing algorithm is initiated from this point. The pixel value of the seed neighbouring is evaluated. If the pixel value belongs to a threshold range, then it is considered as part of the vascular tissues. 3D segmentation label map is exported as result.

TABLE I. MODEL VOLUMES

Model Volumes (mm^3)	Intensity Threshold (HU)				
	120-420	120-500	150-420	150-500	Other
GAD	422.70	422.54	345.90	345.90	
CAD	397.99	398.57	329.27	329.84	
CF	376.47	376.07	305.71	305.45	
Mimics					248.87

B. *Generating a geometric modelating*

The free open source software 3D Slicer version 3.6 was used to reconstruct the model. The software was running under a 64 bit Linux operating system. In the model maker module, the input volume uses a 3D segmentation label map, generated at the segmentation stage. The smooth type is Sinc, and the level is 3. 12 models are generated by the 3D Slicer and another is produced by commercial software Mimics from the CT medical image data through image segmentation.

C. *CFD analysis*

1) *Mesh generation*

As the accuracy of CFD results depends upon the grid resolution and boundary conditions, a series of analyses of verification and validation of mesh independent tests were carried out at the beginning of this study. When the mesh number was around 400,000, the hemodynamic character; energy loss (EL), started to converge into a constant. Therefore, accurately reliable results could be obtained with a total of 563,000 finite elements and 240,000 nodes used in this study. Fig.2 shows the meshes for CFD simulation. In order to accurately calculate the WSS, five layers of prism mesh were inserted onto the artery's internal surface. The distance of the first prism mesh to the artery surface was set to 0.01 mm.

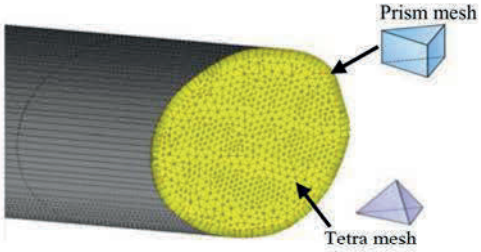

Figure 2. CFD simulation mesh.

2) Calculation

The flow simulation is based on the Navier-Stokes (N-S) momentum equation and continuity equation as defined below:

$$\begin{cases} \frac{\partial}{\partial t}(\rho u_i)+\frac{\partial}{\partial x_j}(\rho u_i u_j)=-\frac{\partial p}{\partial x_i}+\frac{\partial}{\partial x_j}\left[\mu\left(\frac{\partial u_i}{\partial x_j}+\frac{\partial u_j}{\partial x_i}\right)\right]+f_i \\ \frac{\partial \rho}{\partial t}+\frac{\partial}{\partial x_j}(\rho u_j)=0 \end{cases} \quad (1)$$

Where $i, j = 1, 2, 3$, x_1, x_2, x_3 represents coordinate axes, u_i, u_j and p are the velocity vectors and the pressure in the point of the fluid domain, ρ and μ are blood density and viscosity, t is time. The term f_i expresses the action of body forces.

3) Energy loss

Energy loss is calculated as the power difference from inlet to outlet, and can be calculated as follows:

$$EL = \underbrace{\sum\left(P_i+\rho\frac{1}{2}v_i^2\right)}_{E_{inlet}}-\underbrace{\sum\left(P_o+\rho\frac{1}{2}v_o^2\right)}_{E_{outlet}} \quad (2)$$

III. RESULTS

To contrast vascular models, the study utilizes 162725 mm as a region of intersecting (ROI). All models belong to the ROI.

A. Geometric shape

Fig. 3 shows the picture of aneurysm. It clearly shows a bleb A, located on a large protrusion B. There are two protrusions, A and B, clearly observed in the aneurysm. In Fig. 5, the results of GAD and CAD model segment both A and B protrusions. However, the CF and Mimics model only display large protrusion B, bleb A protrusion has not been replicated at segmented results.

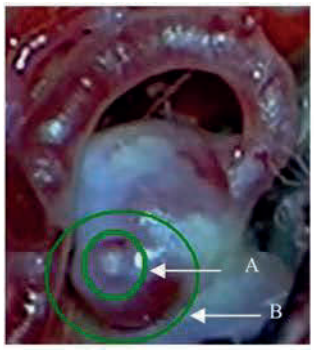

Figure 3. Cerebral Aneurysm

B. Model volumes

All model volumes are listed in Table 1. Fig. 4 clearly shows that under the same intensity threshold range, the GAD method produces the largest volume, when compared to the other models, followed by the CAD method and the CF method. The model with the smallest volume is generated by Mimics. The average volume difference between the GAD method and the CAD method is around 5% and the volume of the CF method is smaller than the volume of the CAD method, which is approximately 6%. The study indicates that the volumes can reach an 11% difference when used with different segmentation methods in the same intensity range. The relationship with the intensity threshold within the GAD, CAD and CF methods is such that, when the low threshold is fixed, the high threshold increases from 420 HU to 500 HU and the volumes change by less than 0.5%. When the high threshold is fixed, the low threshold decreases from 150 HU to 120 HU and the volume change is approximately 18 %.

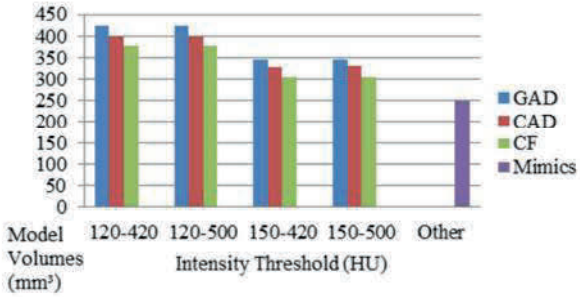

Figure 4. Aneurysm volume vs. Segmentation models

C. CFD Resluts

CFD simulation is performed based upon the segmented

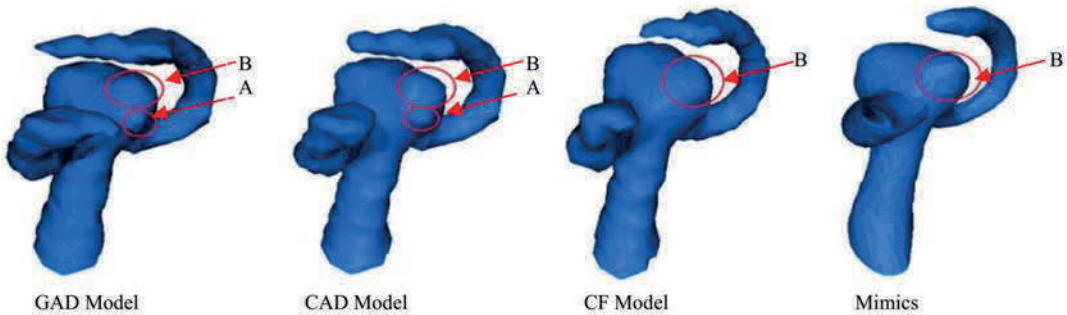

Figure 5. Models segmented by different methods

geometrics. In order to compare various models under the same conditions, the constant inflow condition is selected in this study. The inflow is 125 ml/min. The outflow condition is assumed at its extended length, to be of enough distance to allow pressure recovery. Fig. 6 shows the geometry of the of the velocity vectors on the sections and plane 1 and plane 2 which are shown in Fig. 6. Strong vortex flows are observed in CAD, CF and Mimics, however the velocity of the GAD model has not formed a vortex on the section of plane 1. On plane 2, the velocity vectors are also different from 4 other models. High speed jet flows are observed from the CF model and the Mimics model. Fig. 8 is blood pressure results on section plane 2. Low pressure zones are found from the CAD and the CF models which indicate that it flows in a circular method around the aneurysm. The energy loss (EL) is calculated to be 0.15, 0.173, 0.113, and 0.23(mW) respectively with the CAD, CF, GAD, and MIMICS models. The maximum difference of EL is 34.8%.

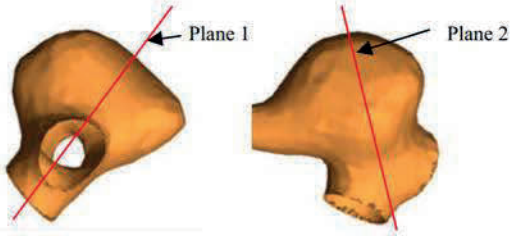

Figure 6. Segmented aneurysm

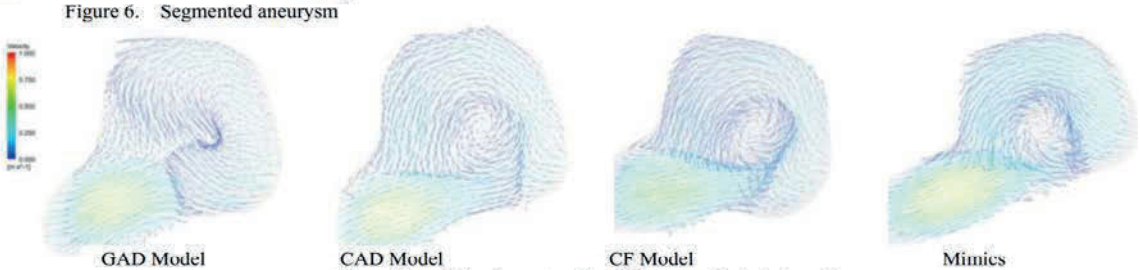

Figure 7a. Velocity vectors by different methods (plane 1)

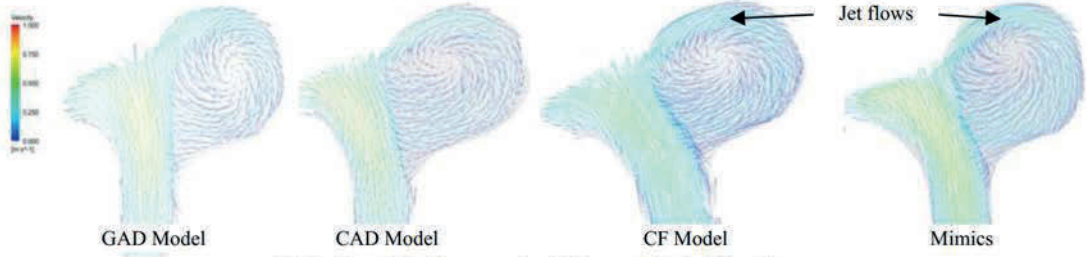

Figure 7b. Velocity vectors by different methods (plane 2)

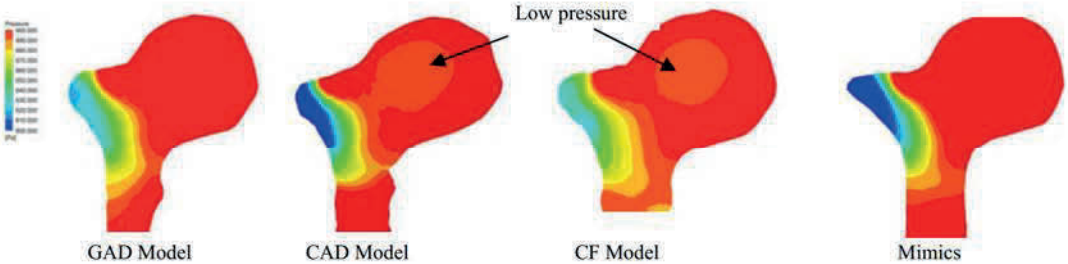

Figure 8. Models segmented by different methods (plane 2)

IV. Conclusion

The study analysed 13 cerebral aneurysm models in geometric shape, volume and hemodynamic results. Although based on the same medical image data, different image segmentation methods generate different models with change in shape, volume and hemodynamic results. The occurrence of uncertain results will negatively affect the accuracy of CFD application in medical surgery. Therefore, a validation process to confirm segmentation will be an important study to limit the error created from image segmentation. Results that are influenced by the segmentation process must be counted into the CFD study. A series of in-vitro and in-vivo validation will be performed in our projects.

References

[1] JB. Tomas, JS. Milner, BK. Rutt, DA. Steinman, "Reproducibility of computational fluid dynamics models reconstructed from serial black blood MRI of the human carotid bifurcation," Ann. Biomed. Eng., vol. 31(2), pp.132-141, 2003.

[2] P.Perona and J.Malik, "Scale-space and edge detection using anisotropic diffusion," IEEE transactions on Pattern Analysis Machine Intelligence," vol.12 pp. 629-639, 1990.

[3] T. Yoo, editor. Insight Into Images: priciples and practice for segmentation, registration, and imge analysis. AK Peters, Wellesley, Massachusetts, 2004.

MACQUARIE UNIVERSITY

Research Office
Research Hub, Building C5C East
MACQUARIE UNIVERSITY NSW 2109 AUSTRALIA

Phone +61 (0)2 9850 8612
Fax +61 (0)2 9850 4465

Ethics
Phone +61 (0)2 9850 6848

Email ethics.secretariat@ro.mq.edu.au
Web www.research.mq.edu.au/researchers/ethics/human_ethics

01/06/2010

Professor Michael Morgan
The Australian School of Advanced Medicine
2, Technology Place, Macquarie University
NSW, 2109

Reference: 5201000234

Dear Professor Morgan

FINAL APPROVAL

Title of project: ***Computational Haemodynamic Evaluation of Patients with Intracranial Aneurysms and Cerebrovascular Bypass Surgery***

Thank you for your recent correspondence. Your response has addressed the issues raised by the Human Research Ethics Committee and you may now commence your research. The following personnel are authorised to conduct this research:

Professor Michael Morgan - Chief Investigator/Supervisor
Dr 'Joe ' Sheau Fung, Professor Alberto Avolio, Professor Itsu Sen, Mrs Azadeh Farnoush and Dr Leon Lai - Co-Investigators

Please note the following standard requirements of approval:

1. The approval of this project is **conditional** upon your continuing compliance with the *National Statement on Ethical Conduct in Human Research (2007).*

2. Approval will be for a period of five (5 years) subject to the provision of annual reports. **Your first progress report is due on 01 June 2011.**

   If you complete the work earlier than you had planned you must submit a Final Report as soon as the work is completed. If the project has been discontinued or not commenced for any reason, you are also required to submit a Final Report on the project.

   Progress Reports and Final Reports are available at the following website:
   http://www.research.mq.edu.au/for/researchers/how_to_obtain_ethics_approval/human_research_ethics/forms

3. If the project has run for more than five (5) years you cannot renew approval for the project. You will need to complete and submit a Final Report and submit a new application for the project. (The five year limit on renewal of approvals allows the Committee to fully re-review research in an environment where legislation, guidelines and requirements are continually changing, for example, new child protection and privacy laws).

4. Please notify the Committee of any amendment to the project.

5. Please notify the Committee immediately in the event of any adverse effects on participants or of any unforeseen events that might affect continued ethical acceptability of the project.

6. At all times you are responsible for the ethical conduct of your research in accordance with the guidelines established by the University. This information is available at: http://www.research.mq.edu.au/about/research_@_macquarie/policies,_procedures_and_conduct

If you will be applying for or have applied for internal or external funding for the above project it is your responsibility to provide Macquarie University's Research Grants Officer with a copy of this letter as soon as possible. The Research Grants Officer will not inform external funding agencies that you have final approval for your project and funds will not be released until the Research Grants Officer has received a copy of this final approval letter.

Yours sincerely

Dr Karolyn White
Director of Research Ethics
Chair, Human Research Ethics Committee

Cc: **Dr 'Joe' Sheau Fung SIA, The Australian School of Advanced Medicine, 2, Technology Place Macquarie University**

Mrs Azadeh Farnoush, The Australian School of Advanced Medicine, 2, Technology Place Macquarie University,

Dr Leon Lai, The Australian School of Advanced Medicine, 2, Technology Place Macquarie University.